Chair of Nonferrous Metallurgy

Doctoral Thesis

# Aluminium alloys in extreme environments for space applications

Dipl.-Ing. Patrick Daniel Willenshofer, BSc

October 2024

## AFFIDAVIT

I declare on oath that I wrote this thesis independently, did not use any sources and aids other than those specified, have fully and truthfully reported the use of generative methods and models of artificial intelligence, and did not otherwise use any other unauthorized aids.

I declare that I have read, understood and complied with the "Preamble on Integrity in Academic Study, Teaching, and Research Operations" of the Montanuniversität Leoben.

Furthermore, I declare that the electronic and printed versions of the submitted thesis are identical in form and content.

Date 08.Oct.2024

Patrick Willenshofer

(The original signature is kept at the university)

# Abstract

The development of a novel crossover aluminum alloy has led to an improved combination of strength and ductility compared to conventionally available Al alloys. Precipitation hardening using a complex intermetallic hardening phase – the T-phase ($Mg_{32}(Zn,Al)_{49}$) – enhances strength in this new class of alloys. A high radiation resistance of crossover alloys has been observed in further experiments, primarily attributed to the precipitation of the T-phase. This may allow for potential use in environments with elevated particle radiation, as required for space applications.

It has been shown that the T-phase remains stable up to 1.0 displacement-per-atom (dpa), while conventional hardening phases – such as the $Mg_2Si$-phase in Al-Mg-Si-alloys – dissolve at 0.2 dpa. The stability of the microstructure and hardening phases is crucial for the material. For example, upon dissolution of the hardening phase, the material loses its strength, compromising the properties for which it was initially designed. Furthermore, point defects are introduced by irradiation, which can aggregate into voids or dislocations, contributing to embrittlement. Previous research has also observed this adverse phenomenon in crossover alloys, where dislocation loops form in the Al-matrix, ultimately leading to premature failure.

To mitigate radiation-induced defects, increasing the number of interfaces, such as grain and phase boundaries, has been proposed in the literature. While the crossover alloy contains 10 vol.-% of the radiation-resistant T-phase, these interfaces alone have proven insufficient to significantly reduce defect formation. Therefore, grain size reduction was necessary.

Through the severe plastic deformation method High-Pressure Torsion (HPT), the grain size of the crossover alloy, was successfully refined, producing a stable

ultrafine-grained microstructure. In-situ irradiation experiments revealed that the alloy remained free of radiation-induced defects, even at an extreme dose level of 24 dpa. This reduction in grain size, while effective in defect mitigation, also influenced the precipitation sequence. Consequently, the precipitation behavior in both coarse- and ultrafine-grained regimes was examined and compared. Given the potential influence of the electron microscope environment (low vacuum and thin film conditions) on these experiments, the precipitation behavior was also assessed using various microstructural characterisation techniques.

The novel ultrafine-grained crossover alloy demonstrated significant resistance to radiation-induced defects at high dose levels. The T-phase's stability was enhanced by increased chemical complexity, and the microstructure remained intact. Additionally, the reduction in grain size accelerated the kinetics of T-phase precipitation, shortening the time required to reach quasi-equilibrium conditions. However, it was also observed that the precipitation behaviour is also influenced by the type of experimental technique used for examination.

# Zusammenfassung

Die Entwicklung einer neuartigen Aluminium-Crossover-Legierung hat zu einer verbesserten Kombination von Festigkeit und Duktilität im Vergleich zu herkömmlich verfügbaren Aluminiumlegierungen geführt. Eine Aushärtung durch Ausscheidung unter Verwendung einer komplexen intermetallischen Härtungsphase – der T-Phase ($Mg_{32}(Zn,Al)_{49}$) – steigert die Festigkeit in dieser Klasse von neuartigen Legierungen. Eine hohe Strahlenbeständigkeit der Crossover-Legierung wurde in weiteren Experimenten beobachtet und wird hauptsächlich der Ausscheidung der T-Phase zugeschrieben. Dies ermöglicht einen potenziellen Einsatz in Umgebungen mit erhöhter Teilchenstrahlung, wie dies für Anwendungen im Weltraum erforderlich ist.

Es wurde gezeigt, dass die T-Phase bis zu einem Strahlungsschaden von 1.0 Displacements-per-Atom (dpa) stabil bleibt, während sich konventionelle Härtungsphasen, wie die $Mg_2Si$-Phase in Al-Mg-Si-Legierungen, bei 0.2 dpa auflösen. Die Stabilität der Mikrostruktur und der Härtungsphasen ist entscheidend für das Material. Bei einer Auflösung der Härtephase verliert das Material beispielsweise seine Festigkeit, wodurch die für das Material vorgesehenen Eigenschaften beeinträchtigt wird. Zudem entstehen Punktdefekte, die sich zu Hohlräumen oder Versetzungen in der Al-Matrix aggregieren können, was zur Versprödung beiträgt. Frühere Untersuchungen haben dieses unerwünschte Phänomen auch in Crossover-Legierungen beobachtet, bei denen sich Versetzungsschlaufen bilden, was letztendlich zu einem vorzeitigen Versagen führen kann.

Zur Minderung von strahlungsbedingten Defekten wurde in der Literatur vorgeschlagen, die Anzahl von Grenzflächen, wie Korngrenzen und Phasengrenzen, zu erhöhen.

Obwohl die Crossover-Legierung 10 vol.-% der strahlenbeständigen T-Phase enthält, haben sich diese Grenzflächen allein als unzureichend erwiesen, um die Defektbildung signifikant zu verringern. Daher war eine Kornfeinung erforderlich.

Mithilfe der Methoden der Hoch-Verformung wie Hochdruck-Torsion, konnte die Korngröße der Crossover-Legierung erfolgreich verfeinert und eine stabile ultrafeinkörnige Mikrostruktur erzeugt werden. In-situ-Bestrahlungsexperimente zeigten, dass die Legierung auch bei extrem hohen Strahlungsdosen bis zu 24 dpa frei von strahlungsinduzierten Defekten blieb. Diese Reduktion der Korngröße, die sich als wirksam zur Defektminderung erwies, beeinflusste auch die Ausscheidungssequenz. Folglich wurde das Ausscheidungsverhalten sowohl im grob- als auch im ultrafeinkörnigen Regime untersucht und verglichen. Angesichts des potenziellen Einflusses der Elektronenmikroskop-Umgebung (Niedervakuum, Dünnschichtbedingungen) auf diese Experimente wurde das Ausscheidungsverhalten auch unter Verwendung verschiedener mikrostruktureller Charakterisierungstechniken bewertet.

Abschließend zeigte die neuartige ultrafeinkörnige Crossover-Legierung eine signifikante Beständigkeit gegenüber strahlungsinduzierten Defekten bei hohen Strahlungsdosen. Die Stabilität der T-Phase wurde durch eine erhöhte chemische Komplexität verstärkt, und die Mikrostruktur blieb intakt. Darüber hinaus beschleunigte die Reduktion der Korngröße die Kinetik der T-Phasen-Ausscheidung, wodurch die Zeit bis zum Erreichen eines quasi-Gleichgewichtszustands verkürzt wurde. Es wurde jedoch auch festgestellt, dass das Ausscheidungsverhalten auch von der Art der für die Untersuchung verwendeten Versuchstechnik beeinflusst wird.

# Danksagung

My greatest and sincerest thanks go to Univ.-Prof. Dipl.-Ing. Dr. mont. Stefan Pogatscher for the invaluable opportunity to carry out my doctoral thesis under his supervision. During this period, I have gained invaluable knowledge and life lessons.

I would also like to express my gratitude to Univ.-Prof. Dipl.-Ing. Dr.mont. Helmut Antrekowitsch, Univ.-Prof. Dipl.-Ing. Dr.mont. Peter Uggowitzer, and all of my colleagues from the Chair of Nonferrous Metallurgy. Each of you has played a significant role in my PhD journey. Some provided me with stimulating scientific discussions, while others shared memorable moments over valuable times. I deeply appreciated both experiences.

A very special thank you goes to my esteemed friend and colleague, Ass.-Prof. PhD Matheus Tunes. His dedication and passion for everything he undertakes are truly inspiring and contagious. He guided me through every step of this process, offering invaluable assistance at every turn. I consider myself incredibly fortunate to have had you by my side throughout this thesis journey.

Lastly, my immeasurable gratitude goes to my girlfriend, Stephanie, and my entire family. Your unwavering support from the beginning of my university journey to the completion of this thesis has been incredible. I am profoundly grateful for your love, kindness, and assistance.

# Contents

# Chapter 1

# Introduction

The demand for aluminium (Al) and its alloys is continuously rising [1], which underscores the significance of Al in our daily lives. The use of Al alloys is pervasive, with applications ranging from safe packaging of food [2] in households to numerous components in the automotive sector [3] and even in aerospace applications [4]. The majority of applications for Al alloys exhibit a distinctive combination of low density ($\rho \cong 2.7 g \cdot cm^{-3}$) and high strength (yield strength up to $R_{P0.2} \cong 500 MPa$) and ease of fabrication and recycling. Consequently, these alloys represent an intriguing subject for further investigation. [5, 6]

In 2020, a new potential application and field for Al alloys was opened. In their research, Tunes *et al.* [7] discovered, that the hardening phase – T-phase ($Mg_{32}(Zn, Al)_{49}$) [8] – withstands heavy ion irradiation. Amongst all known hardening phases in the Al series alloys, the T-phase is superior in this regard. In general, Al alloys with their interesting properties represent an attractive candidate for various applications, where these requirements are needed [9]. The recent discovery of their radiation-resistant properties positions Al crossover alloys as promising materials for use in the harsh conditions of outer space.

In general, crossover alloys represent a novel category of Al alloys, distinguished from existing classifications by their synthesis of two or more distinct Al alloy series. Each series possesses unique characteristics, with the 5xxx series alloys, for instance, exhibiting excellent formability while lacking high strength. Conversly, the 7xxx series alloys are age-hardenable, resulting in high strength, although their formability is limited. The concept of crossover alloying is based on the idea of combining the advantages of two dinstinct Al series alloys. For instance, in the 5xxx/7xxx crossover system, the alloy exhibits high strength due to the age-hardening of the T-phase, while simultaneously displaying good formability [10]. It should be noted, however, that the concept of crossover alloying is not exclusivly applicable to the 5xxx/7xxx system; it can also be applied to other alloy classes as well. However, it is worth mentioning, that the concept of crossover alloying is not strictly applied to the 5xxx/7xxx system, but can applied to different alloy classes as well. [11]

## 1.1 Approach

The objective of this thesis is to build upon the findings of Tunes *et al.* [7], which revealed the simultaneous occurrence of dislocation loop generation and accumulation under particle irradiation. These findings suggest that such occurences may be detrimental under in-service conditions. Additionally, thermodynamically stable dispersoids, such as (Fe,Cr,Mn)-containing particles, were observed to dissolve rapidly, leaving voids in the microstructure. These phenomena, namely the nucleation of dislocation loop networks and void generation, significantly affect the material properties that material scientists have tailored to enhance strength, formability, and heat resistance. Given that this microstructure is incapable of withstanding irradiation, there is a need to engineer a new microstructure to mitigate the impact of heavy ion particles. Accordingly, as proposed in the literature, a reduction in grain size should be the initial step, as an increased volume fraction of interfaces (*e.g. grain boundaries*) is able to act as sinks for radiation-induced point defects and, thus, enhance the material's performance [12]. Concurrently, the radiation-survivability level of the T-phase will be enhanced through an increase in its chemical complexity [13].

Another intriguing aspect emerges when the grain size is reduced: it modifies the precipitation sequence [14]. Given that the radiation-resistant T-phase forms as a secondary-type precipitate after solution heat-treatment and ageing, it is essential to investigate the differences in precipitation behaviour between the coarse- and ultrafine-grained microstructures. While coarse-grained microstructures typically exhibit minimal to no tendency for recrystallization following an ageing treatment due to the stabilisation of grains [15], the behaviour of ultrafine-grained microstructures upon heating should also be studied in order to gain insight into the influence of heat on grain and precipitate size [16].

The examination of ultrafine-grained materials necessitates the use of advanced imaging techniques, as their highly deformed microstructure cannot be easily analysed using conventional methods. Therefore, TEM is often employed. However, when observing electron-transparent samples, they may exhibit different behaviours due to size effects compared to their bulk counterparts. In a third aspect, this size effect should be analysed in relation to the precipitation kinetics of the T-phase using different heating methodologies.

## 1.2 Document Structure

In order to gain a full understanding of the properties of the radiation tolerant crossover alloy, some basic principles need to be addressed. Chapter 1 and chapter 2 therefore provide an introduction to the subject, the definition of extreme environments and where they can be found. The focus is on space applications and the harsh conditions found in space. This is followed by a brief summary of Al and its alloys, including the effects of the alloying elements and the processing route that leads to the exploitation of grain size reduction. Finally, a brief overview of the methods to produce such ultrafine-grained microstructures is discussed. Then, in chapter 3, the alloy synthesis and methodology will be shown. Chapter 4 presents the results of the investigation of the ultrafine-grained microstructure upon irradiation, while chapter 5 gives an insight into the precipitation behaviour of the irradiation-resistant hardening phase (T-phase) in two different grain size regimes. Chapter 6 highlights the microstructural analysis of T-phase precipitates when different heating strategies are used. Finally, chapter 7 provides a brief summary of the results and an outlook.

## 1.3 Reference

[1] Gudrun Saevarsdottir, Halvor Kvande, and Barry J Welch. Aluminum production in the times of climate change: The global challenge to reduce the carbon footprint and prevent carbon leakage. *Jom*, 72:296–308, 2020.

[2] Manuela Lamberti and Felix Escher. Aluminium foil as a food packaging material in comparison with other materials. *Food Reviews International*, 23 (4):407–433, 2007.

[3] Jürgen Hirsch. Recent development in aluminium for automotive applications. *Transactions of Nonferrous Metals Society of China*, 24(7):1995–2002, 2014.

[4] Tolga Dursun and Costas Soutis. Recent developments in advanced aircraft aluminium alloys. *Materials & Design (1980-2015)*, 56:862–871, 2014.

[5] Afaf M Abd El-Hameed and YA Abdel-Aziz. Aluminium Alloys in Space Applications: A Short Report. *Journal of Advanced Research in Applied Sciences and Engineering Technology*, 22(1):1–7, 2021.

[6] Lukas Stemper, Matheus A Tunes, Ramona Tosone, Peter J Uggowitzer, and Stefan Pogatscher. On the potential of aluminum crossover alloys. *Progress in Materials Science*, 124:100873, 2022.

[7] Matheus A Tunes, Lukas Stemper, Graeme Greaves, Peter J Uggowitzer, and Stefan Pogatscher. Prototypic Lightweight Alloy Design for Stellar-Radiation Environments. *Advanced Science*, 7(22):2002397, 2020.

[8] Gunnar Bergman, John L.T. Waugh, and Linus Pauling. The Crystal Structure of the Metallic Phase $Mg_{32}(Al, Zn)_{49}$. *Acta Crystallographica*, 10(4):254–259, 1957.

[9] Jin-Feng Li, Zhuo-wei Peng, Chao-Xing Li, Zhi-Qiang Jia, Wen-jing Chen, and Zi-Qiao Zheng. Mechanical properties, corrosion behaviors and microstructures of 7075 aluminium alloy with various aging treatments. *Transactions of Nonferrous Metals Society of China*, 18(4):755–762, 2008.

[10] Sebastian Samberger, Irmgard Weißensteiner, Lukas Stemper, Christina Kainz, Peter J Uggowitzer, and Stefan Pogatscher. Fine-grained aluminium crossover alloy for high-temperature sheet forming. *Acta Materialia*, 253:118952, 2023.

[11] Bernhard Trink, Irmgard Weißensteiner, Peter J Uggowitzer, Katharina Strobel, and Stefan Pogatscher. High Fe content in Al-Mg-Si wrought alloys facilitates excellent mechanical properties. *Scripta Materialia*, 215:114701, 2022.

[12] H Gleiter. Grain boundaries as point defect sources or sinks—diffusional creep. *Acta Metallurgica*, 27(2):187–192, 1979.

[13] Lingyun Qian, Honggang Bao, Rui Li, and Qing Peng. Atomistic insights of a chemical complexity effect on the irradiation resistance of high entropy alloys. *Materials Advances*, 3(3):1680–1686, 2022.

[14] Yonghao Zhao, Jizi Liu, Troy D Topping, and Enrique J Lavernia. Precipitation and aging phenomena in an ultrafine grained Al-Zn alloy by severe plastic deformation. *Journal of Alloys and Compounds*, 851:156931, 2021.

[15] WC Liu and B Radhakrishnan. Recrystallization behavior of a supersaturated Al–Mn alloy. *Materials Letters*, 64(16):1829–1832, 2010.

[16] FX Zhao, XC Xu, HQ Liu, and YL Wang. Effect of annealing treatment on the microstructure and mechanical properties of ultrafine-grained aluminum. *Materials & Design*, 53:262–268, 2014.

# Chapter 2

# State of the art

The next chapter provides a comprehensive review of extreme environments, with a particular focus on space. It highlights the challenges faced by materials in such conditions. It then provides a detailed overview of Al and its alloys, discussing the influence of primary and secondary alloying elements and the various ways their properties can be modified.

## 2.1 Extreme Environments

Extreme environments push the boundaries of materials science to its limit. Examples include operating temperatures above 1000°C, extreme shock and strain rates, corrosion, pressure, and radiation exposure. [1, 2, 3] Investigating the behaviour of materials under extreme conditions is critical to addressing many challenges. However, certain issues remain particularly complex due to our limited understanding of multiscale phenomena, in particular, how the formation of atomic defects translates into nanoscale and ultimately macroscale effects. To design and develop more resilient materials, it is essential to characterise them at the level of fundamental interactions. This includes, for example, *in situ* observations of atomic and defect dynamics in materials exposed to harsh environments. [4]

It is only through constant advances in technology and materials that mankind's dream of exploring the deep universe can be realised. The first step in this never-ending story was the Apollo mission [5]. Led by the National Aeronautics and Space

Administration (NASA), this marked a monumental first step by successfully landing the first men on the Moon. During these missions, Al alloys played a crucial role, serving as both thermal control and structural materials. In addition to the use of Ti-6Al-4V titanium alloys, a wide range of Al series alloys were used, including the 2xxx, 5xxx, 6xxx, and 7xxx series. [6].

Subsequently, humanity aims to delve deeper into our galaxy through the colonization of Mars [7]. While the requirements for both missions have been relatively modest, the exploration of the deep universe presents a distinct and elevated level of challenges [8]. The material exposed in space environment will suffer temperature fluctuations from $\approx$ -100°C to $\approx$ +100°C, high-energy radiation and immense ballistic impacts from micro-meteoroids and space debris. [9, 10, 11, 12, 13]

During deep-space missions, there is a critical need for materials with enhanced radiation resistance [14]. The development of high-performance materials for use in space is partly driven by the challenges posed by space weather, which will be covered in the next section.

### 2.1.1 Space Weather

In simple terms, similar to weather phenomena on Earth, there are weather-like occurrences in space, and these are always linked to the Sun. In an expanded definition, space weather also encompasses space debris, asteroids, meteoroids, radiation and particles, cosmic rays, nearby supernova explosions, and even the broader galactic environment [15, 16]. The list below shows different types of space weather: [17, 18, 19, 20]

- Solar flares
- Solar energetic particles (SEPs)
- Solar wind
- Coronal mass ejections (CMEs)
- Geomagnetic induced storms

- Galactic Cosmic Rays

Figure 2.1 displays two major events of the Sun: a Solar flare and a Coronal Mass Ejection. Even though these events primarily occur in space, their impact on Earth is significant [21]. Power grids, the global positioning system (GPS), air travel, and spaceflight can be affected while satellites may start to behave abnormal and even pipes laid in the ground will corrode more strongly. This is due to rapid fluctuation of geomagnetic fields, inducing currents in pipelines, which enhances the rate of corrosion significantly in those pipes [16, 22]. However, it is not possible to prevent the affects of space weather here on Earth but only to minimize them. A good prediction model is nonetheless important [23, 24]. Spontaneous occurrences of these events have been observed in the past, yet a clear signature indicating an event and its likely timing, location, magnitude, and significance for Earth is still missing. When such an event is happening and reaches the boundaries of Earth, a series of processes will be triggered caused by the Earth's magnetic field (*i.e.* the ionosphere and atmosphere) [21]. For example, the *Aurora Borealis* (also known as "the Northern Lights") are the widest known manifestation of the interaction between SEPs and our atmosphere, depicted in Figure 2.2. [25]

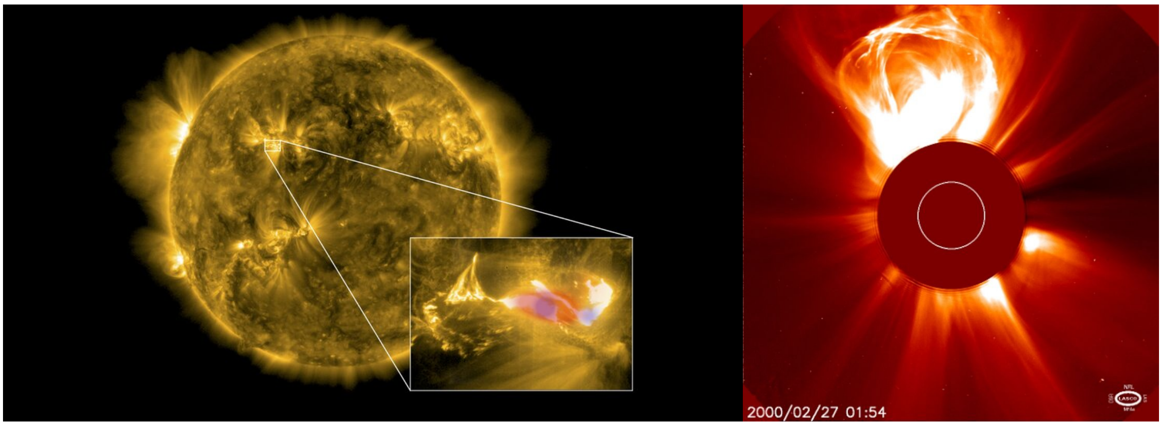

(a) Solar Flare

(b) Coronal Mass Ejection

Figure 2.1: **(a)** A solar flare captured by the European Space Agency (ESA). Red and blue colours highlighting areas with different types of X-rays. **(b)** An image of a Coronal Mass Ejection. The disk blocks the bright light of the Sun, while the white circle inside shows the Sun's surface. [26, 27]

Consequently, the Sun and the solar wind, as primary drivers of space weather, have received significant attention in the past. Typically, the Earth's magnetosphere,

Figure 2.2: The interaction between highly energetic particles emitted by the Sun and the Earth's atmosphere is the cause for an astonishing spectacle on Earth: the Aurora Borealis. The mesmerizing and mystifying colour is a simple reaction between the SEPs and molecules of the atmosphere (mostly oxygen and nitrogen). [25]

maintained by its intrinsic magnetic field, redirects the solar wind flow away from Earth. However, during abnormal events, such as when the northward pointing Earth field encounters a solar wind with a southward pointing field, SEPs may penetrate the magnetosphere, leading to various geomagnetic disturbances. [21, 28]

The radiation dose from these significant incidents has emerged as a crucial concern in manned space exploration. Solar flares, for instance, release flashes within seconds and lasting to minutes, spanning a vast wavelength range across 17 orders of magnitude, from kilometric radio waves to gamma rays. This huge variation is also measured for the total energy released during such events: between $10^{12}$ J for small events up to $10^{25}$ J for major events. In comparison, the total generated electricty on Earth in 2017 was equivalent to $10^{19} J$, therefore, a major Sun event could provide Earth's energy need for about 16.000 years. [21, 29, 30]

Here on Earth, mankind is protected by the invisible layer the magnetosphere provides around Earth. This is not the case for space exploration. For example, Mars' outer layer is not as protective as Earth's: the average radiation dose on Mars is about 140 times higher than on Earth [31]. Finally, this is the reason for the major concern of long-term space missions. Both astronauts and materials are exposed to these types of radiation and doses, with varying intensities and occurrences, emitted by the Sun. Therefore, it is crucial to guarantee the safety of them during long-term deep-space missions, where lack of protection is found. At this point, materials science is taking the leading role to design the next-generation material used in the extreme environments of space. The design of an irradiation-resistant alloy must be addressed at the atomic scale to meet the needs of safety, durability and reliability. While the Al crossover alloy, hardened by irradiation-resistant T-phase, was found to be a potential candidate, the reasons of its behavior still remains unclear.

Beside the invisible danger space weather is constantly providing to space missions, there is a growing concern about space debris, which is threatening not only space missions but also humanity on Earth.

Space debris are objects that have been discarded in Earth's orbit and are continuously accumulating over time. In 1978, there were approximately 6,000 trackable objects in orbit. By 2005, this population had more than doubled to 14,000. Only large objects with sizes greater than 1 m are easily tracked and catalogued, but small-size space debris objects causes concern. They cannot be tracked, their number is several orders of magnitude higher than that of large objects and is continuously rising and their impact on operating space crafts can lead to significant damage or even to catastrophic failure. The distribution of small-size space debris is displayed in Table 2.1. The size of these objects are typically small, measuring between 1 and 10 cm and their relative velocity can reach values up to 15 km/s. A collision of a space craft with small-size space debris can neither be predicted nor avoided. Figure 2.3 shows the detrimental impact of an Al sphere, travelling at the speed of approximately 6.8 km/s, hitting an 18 cm thick Al block. In comparison, Figure 2.4 shows the damage of a solar cell and the windshield of a space shuttle after it was hit by space debris. Therefore, a high-strength structural material is therefore necessary to minimise the damage coming from space debris. [11, 32, 33, 34]

As explained earlier, the number of small pieces of space debris is exponentially increasing due to a phenomenon called *Kessler Syndrome*. This term was created back

Table 2.1: Estimation of orbital debris by size between 2010 and 2023 by size. [34, 36]

| Debris Size | <10 cm | >10 cm |
|---|---|---|
| 2010 | 400.000 | 16.000 |
| 2023 | 670.000 | 29.000 |

in the late 1970s and predicted an increase in space debris in low Earth orbit in the early 2000s. Since then, the prediction has come true, as a result of collisions between large catalogued objects, which scatter into smaller particles. This led to a cascade of collision events. As of today, the number of untrackable small-size space debris has reached values over 670.000, as shown in Table 2.1. However, these numbers are still increasing, even with a net zero input of additional space debris is maintained, due to the collision cascade effects. [35, 36]

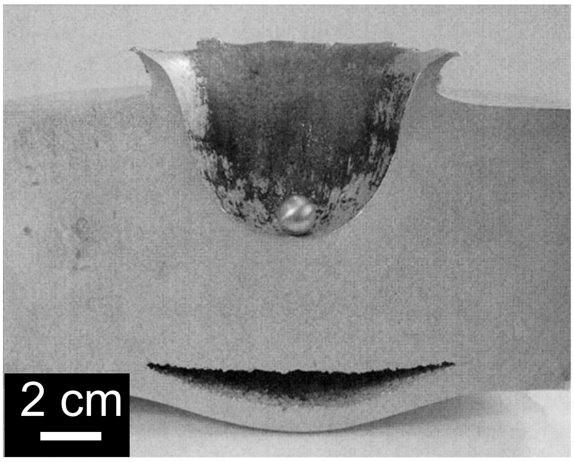

Figure 2.3: Simulation of the impact of an Al sphere with 1.2 cm in diameter and a weight of 1.8 g. The sphere hit the 18 cm thick Al block at a speed of 6.8 km/s. [34]

### 2.1.2 The nature of radiation damage

This section is intended to provide a brief introduction to the nature of radiation damage, particularly where metals are concerned. The origin of radiation ranges from natural cosmic phenomena to man-made applications, however, they only differ in terms of intensity. When metals are intentionally irradiated for study or accidentally irradiated during space missions, the damage caused by irradiation can best be described as the formation of voids and interstitials. The formation of these defects

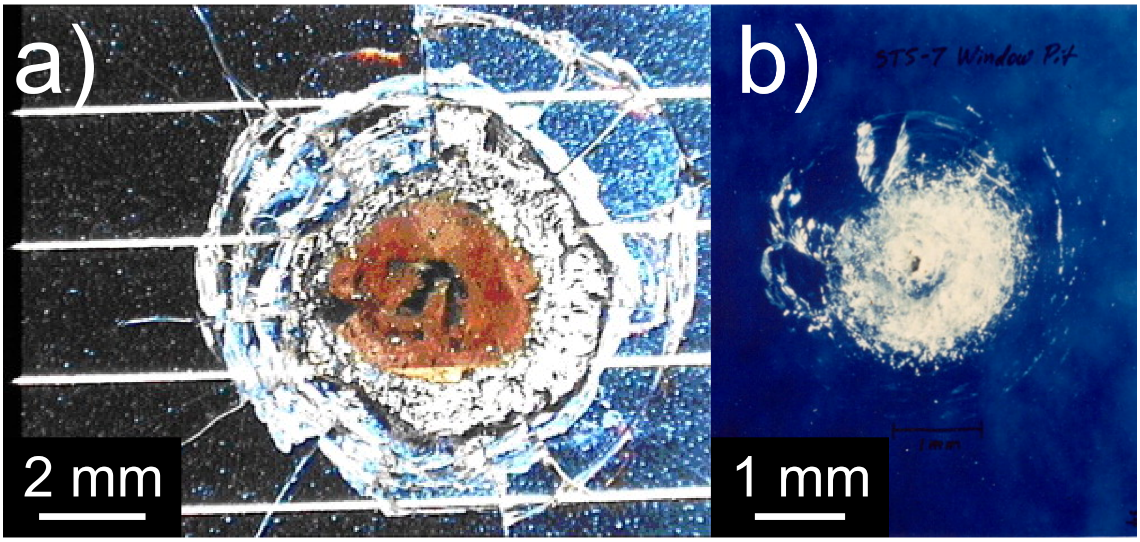

Figure 2.4: Impact of space debris. a) is displaying a crater on a solar cell. The crater has an diameter of 4 mm. b) Impact crater on a window of a Space Shuttle. Impacts with this sizes need to be replaced. [11]

is not uniformly distributed throughout the material, but is concentrated in a small volume. These defects are only observed in a low temperature regime and when the microstructure is in a stable condition, otherwise, the nucleation of a more stable phase is possible. For example, when heavy ions are used as bombarding elements, the temperature in a small volume rises sharply and is promptly quenched. [37]

During radiation, a primary knock-on atom (PKA) is generated by a nuclear reaction, radioactive decay or from an accelerated ion beam. This event occurs over a timescale of fraction of a second ($10^{-15}$s). The energy of the PKA is transferred either via the excitation of electrons in the medium or those of the PKA itself. This excitation process may then lead to ionisation of some of the particles. During collision, the total kinetic energy is nearly conserved and are considered to be quasi-elastic. However, on occasion, when the PKA collides with atoms, they may receive sufficient kinetic energy to displace them from their lattice sites, thus enabling them to make similar collisions of their own. This results in a branching tree-like structure of successive collisions, accompanied by electron excitation, which produces heat in metals. While most defects are unstable and rearrange them rapidly into more stable configurations, some of them recombine or agglomerate into defect-clusters. Besides, not only microstructural damage can appear, but also sputtering, chemical disorder, unusual chemical reactions or phase changes. [38]

In order to displace an atom, it is necessary to overcome the threshold energy $E_d$. If a lattice atom receives an energy that is higher than the threshold ($E \geq E_d$), then the lattice atom is permanently displaced. Only when the energy received is less than the threshold energy ($E < E_d$), no displacement occurs. The transferred energy must be greater than the sum of both the formation energies of a vacancy ($E_V^F \approx$ 1 eV) and an interstitial atom ($E_I^F \approx 4$ eV). However, $E$ needs to be significantly larger, as it is necessary to move the displaced atom out of its own recombination zone. Therefore, the displacement energy should be 4-5 times the sublimation energy. As suggested by Seitz *et al.*, $E \approx 25$ eV, which holds true for most metals [39, 40]

### 2.1.3 Parameters in radiation experiments

As with any experiment, it is essential to carefully define the parameters that influence the setup. This chapter will provide a concise overview and explanation of the key parameters involved in irradiation experiments on metals.

**Type and Energy of Radiation** Radiation damage can originate from various energetic particles, such as neutrons, ions, electrons, gamma rays, and protons. The energy level of these particles dictates the degree of displacement damage within the crystal lattice. Both the type and energy of the radiation influence the penetration depth and extent of the damage. In this context, energy specifically refers to the kinetic energy of the incident particles, commonly measured in electron volts (eV). [42]

**Dose Accumulation** The term dose quantifies the amount of radiation energy deposited in a material over a defined volume, providing a measure of radiation exposure and the resulting damage within the crystal lattice. This damage manifests as defects, including dislocations, voids, and vacancies. Two primary types of dose are typically considered: the absorbed dose, which refers to the energy absorbed by the material, and fluence, representing the number of incident radiation particles. Dose is a cumulative parameter that considers both the number of particles striking the material and the energy they deposit. While fluence only accounts for the number of incident particles (expressed in $particles/m^2$), the dose considers both particle count and the energy deposited. The dose is commonly expressed in Grays (Gy), where 1 Gy = 1 J/kg. Additionally, to quantify structural damage, the absorbed dose is often expressed in "displacements per atom" (dpa). It quantifies the number of times an atom in a solid material has been displaced from its lattice position due to interactions with energetic particles, such as neutrons, ions, or electrons. In simple terms, if a material has experienced 1 dpa, it means that, on average, each atom in the material has been displaced once from its original position by the impact of radiation. [42, 41]

**Temperature and Time** Temperature plays a critical role in irradiation experiments, as it affects the mobility of radiation-induced defects and their potential for self healing. At low temperatures, defects may become trapped, while higher temperatures can promote their recombination. [43]

As previously discussed, dose quantifies the accumulation of radiation damage within the material, making irradiation time another significant factor in determining material stability. As time progresses, damage accumulates, and the dose continues to rise, influencing the material's structural integrity.

## 2.2 Aluminium and its alloys

The following chapter provides an insight into Al and its alloys in terms of alloying and processing. Processing then leads to the grain refinement into the ultrafine-grained (UFG) and nanocrystalline (nc) regime.

### 2.2.1 Impact of the alloying constituents

Typically, the alloying elements establishes the potential properties of the material. Subsequently, final processing refines this potential and determines the ultimate properties of the alloy in practical applications [44]. Given the different characteristics of each element in the periodic table, this section will look at the primary alloying elements of the examined crossover alloy under consideration to analyse their remarkable behavior. Finally, some other interesting elements are discussed.

**Magnesium (Mg):** Mg tends to occupy substitutional sites in the crystal, and thus acting as an obstacle to gliding dislocations. This yields in an enhanced strength with increasing Mg content [45, 46, 47]. Simultaneously, Mg is reported to decrease the stacking fault energy of Al [48], which makes cross-slip more difficult and decreases strain localization [45, 49]. The age-hardening response in Al-Mg base alloys is rather low [50], because Mg is trapping vacancies after solution heat treatment and quenching due to a strong binding energy of Mg solute-complexes [51]. Subsequently, they are released upon ageing at elevated temperatures. Precipitation of T-phase type particles can be stimulated via the introduction of Zn and the released trapped-in vacancies [52].

**Zinc (Zn):** Zn addition results in a change of the microstructure: in Al-Mg base alloys, *i.e.* 5xxx series alloys, the $\beta$-phase ($Al_3Mg_2$) precipitates along the grain boundaries, making it prone to intergranular corrosion and stress corrosion cracking [53]. However, Zn additions can fully suppress the formation of $\beta$-phase [54], thus enhancing the corrosion resistance of the alloy while improving the age-hardening response and facilitating even higher strength values [55, 56]. The addition of Zn to Al-Mg based alloys promotes the formation and transformation of the T-phase during solidification and ageing, significantly improving the alloy's precipitation kinetics and strength [57]. Additionally, it is reported that increasing the Zn content decreases the formation energy of the T-phase [**?**].

**Copper (Cu):** When Cu is added to the Al-Mg-Zn crossover alloy, the thermal stability of the T-phase is improved. Moreover, Cu reduces the width of the precipitation free zone (PFZ) between the grain boundary and the matrix precipitates, which results in a higher intergranular corrosion resistance [59]. Additionally, an increase in thermal stability of the T-phase in Al-Mg-Zn-Cu alloy is reported [60], because Cu modifies the morphology of the T-phase into spherical-like. While a decrease in hardness is often caused by coarsening of precipitates, Cu will inhibit this coarsening mechanisms due to its low diffusion coefficient [61]. Furthermore, Cu is stabilizing and promoting the nucleation of T-phase precursors over the whole precipitation sequence. This leads to an enhanced strength of the alloy [62].

**Silver (Ag):** Even trace additions of Silver, up to 0.2 wt.-%, are beneficial regarding a finer and more dense distribution of T-phase precipitates, while such additions are also enhancing the strength of the alloy. It must be noted that higher Ag additions may promote void nucleation as well as their growth and crack propagation. The report from Liu *et al.* [63] emphasizes the importance of the amount added to the alloy. Moreover, the atomic radius for Al and Ag is 0.143 nm and 0.144 nm, respectively. Both solutes will easily form solute pairs and clusters. This can enhance the density of GP zones during aging treatments. [64]

Both Cu and Ag share the ability to lower the formation energy of T-phase [**?**], making it easier to nucleate the T-phase during age-hardening. However, there is a wide range of reports on different alloying elements, how they affect the behavior of the crossover alloy.

### 2.2.2 Effect of processing

While the previous chapter elucidated the influence of various alloying elements on the performance and properties of the AlMgZn crossover alloys, an impact is also achievable through different processing techniques. This chapter will discuss the most prominent methods.

Due to the high activation energy of the hardening phase (T-phase) [65], the nucleation and growth of these hardening particles, takes long times [52, 51]. Aging at low temperatures yields in a slow aging response, which takes hours to reach peak hardness. In fact, Cao *et al.* [51] reported that the peak-aged condition of an Al-5.2Mg-0.45Cu alloys at 180°C is reached only after 168h, while the Al-5.2Mg-2.0Zn alloy only needs 24h to reach peak hardness. Since both cases are not applicable for industry, new ways have to be found to shorten the peak-aging time drastically.

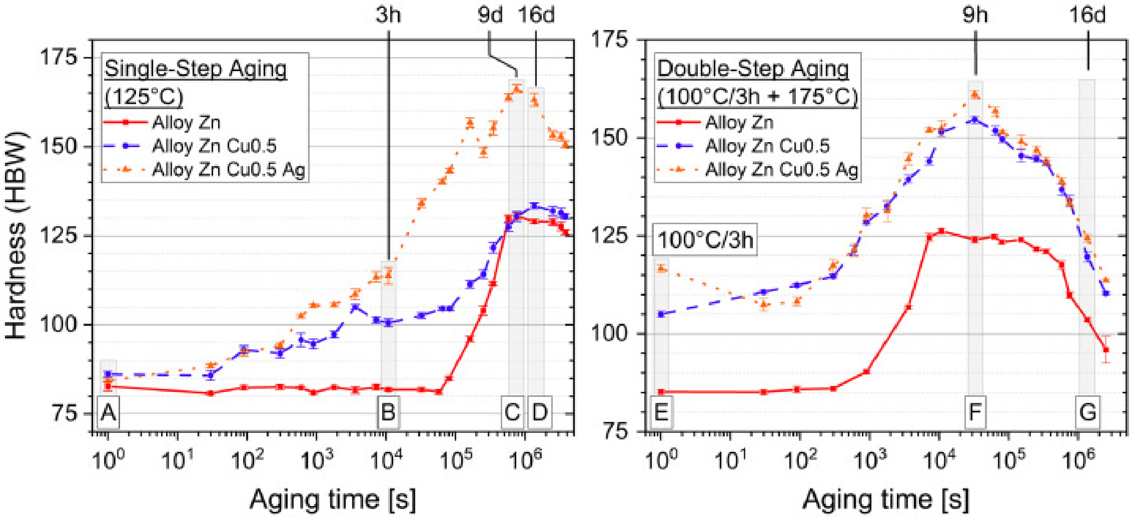

Figure 2.5: Age-hardening response of a Al-Mg-Zn crossover alloy with additions of Cu and Ag. Left image displays the hardening response of single-step aged alloy at 125 °C, while the image on the right shows its behavior upon double-step aging at 100°C/3h + 175°C/x. [55]

Cao *et al.* [66] pursued this issue further and observed a significant reduction in peak aging time when pre-aging is applied. His results suggested that pre-aging can reduce the amount of time to only 20% compared to a peak-aging heat-treatment without pre-aging. Similar results were also observed by Stemper *et al.*, which are depicted in Figure 2.5.

The introduction of the T-phase as main hardening phase in Al crossover alloys facilitates several advantages, as mentioned earlier. Among all hardening phases, the T-phase is unique in its properties. It is reported that this hardening phase has a high hydrogen trapping capacity [67], resistance upon heavy ion-irradiation [68], allows for age-hardening in 5xxx/7xxx crossover alloy systems [69], and is able to inhibit grain growth or to generate particle stimulated nucleation [70]. The potential of the T-phase is significant and thus offering researches a wide range of opportunities.

### 2.2.3 Aluminium alloys in radiation-rich environments

As outlined at the beginning of this chapter, extreme environments can occur at elevated temperatures, in corrosive conditions, or in radiation-rich settings. While Al alloys have been extensively studied under varying temperature regimes and corrosive environments, research in radiation-rich conditions remains limited, resulting in a scarcity of literature in this area. Nevertheless, this section aims to present the available knowledge on the subject.

**Irradiation experiments** There is little available literature upon irradiation experiments on Al alloys. For example, Lohmann *et al.* [71] and Singh *et al.* [72] investigated irradiation effects on commercially available AlMg and AlMgSi alloys. Neither the cold-worked microstructure nor the $Mg_2Si$ hardening phase survived upon irradiation of 0.2 dpa, resulting in a significant drop in hardness [71]. High-purity Al was irradiated with 600 MeV protons, resulted in the formation of large dislocation networks and bubbles [73]. Liu *et al.* [74] studied microstructural changes of age-hardenabale Al alloys upon neutron irradiation. He observed a break-up of small GP zones and precipitates, resulting in smaller size of the particles and a wider volume fraction after irradiation [74]. On the contrary to the previously reported results, Flament *et al.* reports the stability of the $\beta''$-phase under high dose ion irradiation [75], while simultaneously, reports can be found which state the opposite [71, 76]. However, this controversial findings suggest for a more detailed study on the stability under heavy ion irradiation of the $\beta''$-phase. The above mentioned literature is mainly focused on the 6061 Al series alloy, as it is one of the most important alloys industrially produced. In 2020, Tunes *et al.* has discovered the stability of the T-phase upon heavy ion-irradiation up to 1.0 dpa. He ascribes this feature to the high volume fraction of the T-phase in the crossover system and the chemical complexity of the T-phase [68].

Investigations on a supersaturated Al-Cu system was carried out under neutron irradiation, with the main findings that the formation of $Al_2Cu$-phase ($\theta'$-phase) is accelerated. This phenomena is linked to the formation of damage centers in the matrix [77]. The effects of neutron irradiation on the mechanical properties of pure Al was carried out by Farrell *et al.* [78]. After irradiation, they observed an increase in the ultimate tensile strength, which they linked to fine precipitation of transmutation-produced silicon, while the work hardening exponent and elongation was significantly reduced. Similar to this previous findings, proton irradiation on 5083 Al series alloy lead to an increase of microstrain and microhardness values [79].

Similar observations were made on self-ion irradiated 6061-Al series alloy, where nanointendation showed an increase in hardness after irradiation [80]. Meanwhile, a drop in hardness of the 6061-Al series alloy was observed due to neutron irradiation, which can likely attributed to the dissolution of the age-hardening precipitates present before irradiation [81], while neutron irradiation on a similar alloy can lead to radiation-induced precipitation and thus hardening of the alloy. This behaviour may be attributed to the difference in neutron fluences in both experiments [82]. Ar ion irradiation on a cold-worked 1441-Al series alloy resulted in the dissolution of $Al_3Zr$ and $Al_8Fe_2Si$ particles, while the nucleation and formation of new plate-like $Al_2LiMg$ phases were observed due to the irradiation [83].

Jahnke *et al.* [84] studied the formation of voids in an Al-Mg-Si alloy and in pure Al under different precipitation conditions using 100 keV Al ions. Voids in the pure Al were observed over the whole experimental range, while the formation of voids in the Al-Mg-Si alloy strongly depends on the thermal treatment. In aging treatments with coherent precipitates present in the matrix, the void formation was fully suppressed, while aging treatments which lead to incoherent or partially coherent precipitates resulted in void formation [84]. However, Singh *et al.* did not observe void formation within the grains in pure Al, AlMg3 or 6061 Al alloy, but observed gas bubbles in the pure Al and AlMg3 but not in the 6061 alloy [85]. In this regard, Engman *et al.* [86] has successfully removed radiation-induced voids through annealing while monitoring them *in situ*. Void formation suppression was also observed by 100 and 400 keV self-ion irradiation in a Al-3%Mg (wt.-%), attributing this resistance to vacancy trapping on small second-phase particles [87]. On the other hand, void formation was observed by neutron and ion irradiation in a 6061 T6 series alloy, but more importantly in this case, the corrosion rate increased [88].

The increase of the corrosion rate was also observed in a 6xxx series Al alloy after in-service conditions in pool water of a low-power research reactor [89]. The material was exposed to neutron and gamma rays, and thus, their interaction played a different role. Neutrons are likely to collide with the atomic nuclei, which causes displacements and thus microstructural changes (*i.e.* formation of defects or new phases). Gamma rays induced chemical reaction in the pool water, forming corrosive species (*i.e.* free radicals, reactive oxygen). Both types of irradiation will negatively affect the corrosion resistance of the alloy. [89, 90]

## 2.3 Exploiting the benefits of ultrafine-grained microstructures

The grain size in aluminium alloys is crucial that profoundly affects their mechanical properties and performance characteristics. The microstructure of these alloys is characterized by the size, distribution, and orientation of individual grains, which are formed during solidification or recrystallisation processes. Finer grain sizes generally result in enhanced strength, hardness, and fatigue resistance due to the increased grain boundary area, which impedes dislocation movement and improves strengthening mechanisms. Heat treatments and processing techniques can be employed to control the grain size and optimize the material properties for specific applications. As indicated by Hall and Petch [94, 95] in the well-known Hall-Petch Equation, see Equation 2.1, the yield strength $\sigma_y$ is directly proportional with inverse grain size. Therefore, a reduction in grain size leads to increased yield stresses.

$$\sigma_y = \sigma_i + k_y \cdot d_g^{-1/2} \tag{2.1}$$

For decades, this equation has been describing the relationship between yield strength and grain sizes of various metals and alloys. The term $\sigma_i$ describes the lattice function (i.e., impediment of the movement of dislocations through the crystal), $k_y$ is the so-called Hall-Petch constant and $d_g$ is the average grain size diameter. [96]

As shown in Figure 2.6, a decrease in grain size can enhance the yield strength significantly. But this is not only true for the yield strength, as many other important properties of the material will be positively affected by a smaller grain size. For example, wear resistance [97] and fatigue will increase upon decreasing grain size [98]. However, a reduction in grain size via conventional methods is not easily achieved.

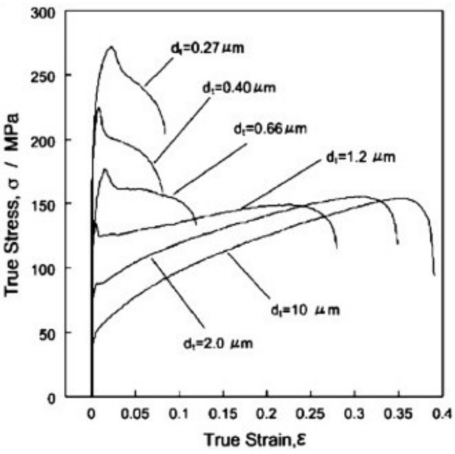

Figure 2.6: Experimental stress strain curves of pure Al with different grain sizes. [?]

This occurs because the numerous grain boundaries store a significant amount of excess energy, rendering the microstructure highly unstable, even during storage at room temperature [99, 100]. Murdoch *et al.* has proposed a list of requirements to achieve a stable nanocrystalline material, where the most important ones are: [101]

- A specific nanostructure is required: segregation-stabilized, dual-phase nanostructures or amorphous-type structure.
- The energy of the grain boundary needs to be zero.
- Enthalpy of segregation should be higher than enthalpy of mixing.

If one or more of the above mentioned requirements is fulfilled, then a stable nanocrystalline (grain sizes < 100 nm) or a (meta)-stable ultrafine-grained microstructure (100 nm < grain sizes 1000 nm) is achieved. Until now, only the physical aspects were discussed. The next section elucidates the processing techniques to create sophisticated nanocrystalline microstructures.

## 2.4 Severe Plastic Deformation

Severe plastic deformation (SPD) methods are widely acknowledged for their possibility to reduce the grain size of materials from the coarse-grained regime (>> 1 µm) down to the UFG regime, and even to the nanoscale regime. In most cases, the properties of the SPD-processed materials are superior to their coarse-grained counterparts [102]. Classics methods to produce UFG materials are High-pressure Torsion (HPT), Equal-channel angular pressing (ECAP) and Accumulative roll-bonding (ARB). However, this thesis will only cover the basics of HPT, as it was used extensively to produce UFG crossover alloys.

### 2.4.1 High-pressure Torsion

The principle of HPT is as follows: a disc is placed between two anvils, with one fixed and the other capable of rotation. A sketch of the setup is shown in Figure 2.7. The anvils subject the material to intense strain and torsional force. But with this setup, two limitations are encountered: first, material will flow out and thus restricts the applied pressure and second, the applied pressure is restricted by the compressive yield strength of the anvils. Furthermore, the process is discontinuous, and thus restricting the sample size [103]. With this limitations, HPT is not applicable for industrial scale operations, but according to Ref. [102], there is a trend to scale up the sample size and to develop new (semi-)continuous processes for industrial applications. [104]

It is also important to note the sample preparation. For HPT, a round disk is required, which fits between the anvils. Due to this geometric requirements, the applied shear strain is a function of the radius of the disk, as described in Equation 2.2:

$$\gamma = 2\pi r N/h \tag{2.2}$$

where r is the distance from the disk center, N is the amount of rotations and h is the thickness of the disc. Therefore, when investigations are carried out on the deformed disk, the properties strongly depend on the position ($r$) on the disk.

#### Grain boundaries

One of the most fundamental quantities when it comes to nanostructured materials is the number of grain sizes – and simultaneously – the fraction of grain boundaries. As the grain size decreases, the amount of interfaces (i.e., grain boundaries) increases. While most of the materials' properties will be positively affected from smaller grain

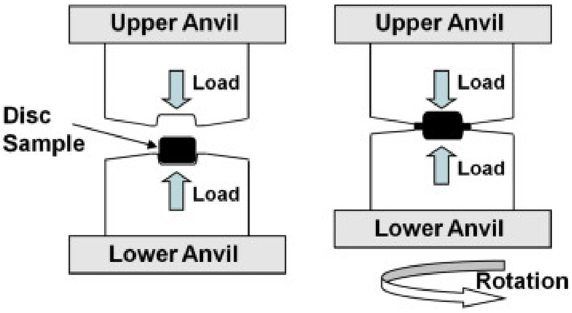

Figure 2.7: Schematic illustration of an HPT tool after loading and after deformation. In most cases, the thickness of the sample is then reduced. [105]

sizes, they become more prone to grain growth upon minimal heating. The migration of grain boundaries is primarily driven by the excess energy stored in the grain or interphase boundaries. [106] Grain growth can be estimated using the following equation for ideal grain growth in Equation 2.3:

$$D^2 - {D_0}^2 = k \cdot t \tag{2.3}$$

where $D_0$ and $D$ are the grain sizes at the beginning and a given time t, respectively. The term k presents a temperature-depended factor. However, it was shown in the past that it is possible to inhibit grain growth to a certain extent, when the sample is short-time annealed at low temperatures. This was the result of atomic rearrangements in the boundaries, as the excess energy stored was reduced by 40 %, as displayed in Figure 2.8 [107]

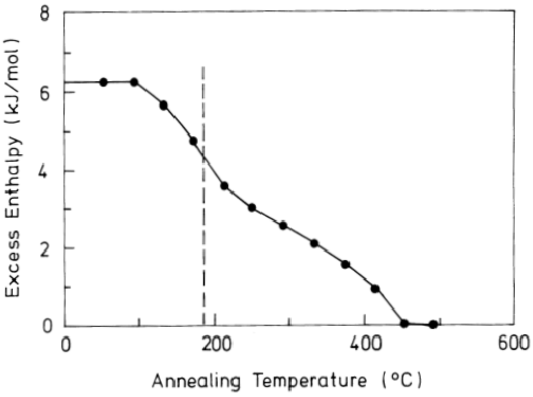

Figure 2.8: Plot of the excess enthalpy upon annealing temperature of nanostructured Pd (10 nm average grain size). Up to the dashed line, no measurable grain growth was observed but the stored energy reduced significantly. [107]

There are several other attempts to stabilise or restrict grain growth. In some cases, the growth kinetics are reduced by decreasing the excess enthalpy (as shown in Figure 2.8) or the GB mobility. Another approach is to reach a truly metastable condition of the material, where a small increase in the GB area increases the excess enthalpy. In this situation, a large energy barrier has to be overcome to start grain growth, which then would be achieved via thermal activation. [106] Second-phase particles can also be used to decrease the total free energy at the GBs and to pin the GB movement. This is explained by the well-known Smith-Zener limit in Equation 2.4: [108]

$$R = 4r/3f \tag{2.4}$$

where $r$ is the radius of the pinning particle and $f$ their volume fraction. While grain growth strongly depends on the grain boundaries curvature, their growth could be inhibited with second-phase particles. During annealing, the grain size would stay at a rather constant level until the dispersion of these second-phase particles will dissolve within the matrix. Zener pinning was successfully demonstrated in a cryomilled 5083 Al alloy. [106, 109] The uniform dispersion of second-phase particles is crucial for the Zener limit to work: there are some reports, where rapid grain growth occurs in certain grains. Noteworthy, grains which do not have pinning particles on their GBs, resulting in a bimodal grain structure. [110, 111]

This phenomenon becomes particularly significant in extreme environments, such as heavy-ion particle irradiation, where a smaller grain size is preferred. This was first observed by Singh *et al.* in 1973. He discovered that the interaction between defects and an interface (*i.e.* grain boundary) increases with decreasing distance between those two. [112, 113]. Therefore, when the distance for interaction is small enough, they will interact. A review article highlighted two main effects of absorption types: [114]

- A dislocation loop near a high-angle grain boundary reduced its diameter over the spawn of 49s, and then abruptly migrated 10nm towards the grain boundary within 0.1 seconds, where the dislocation loop vanished - indicated in Figure 2.9

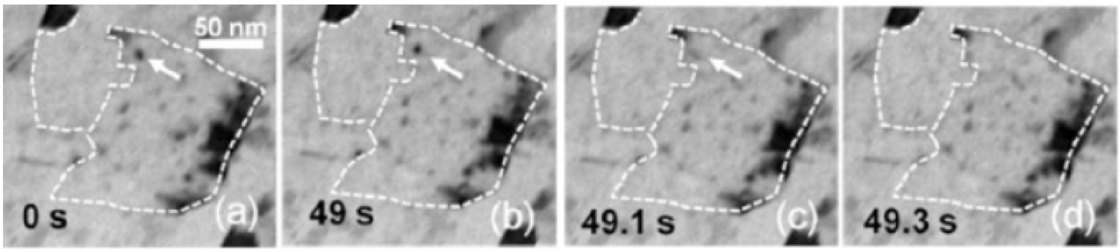

Figure 2.9: Evidence of the absorption of an dislocation loop by a nanostructured grain boundary. Within a time frame of 49s, the dislocation loop (indicated with white arrows) migrated towards the grain boundary and was fully absorbed. [114]

- A segment of a dislocation was gradually annihilated by a grain boundary.

It has been showed that GBs play an important role to mitigate radiation damage. Thus, it can be assumed that the characteristics of the GB determines the *sink strength* of radiation damage, as elucidated by Tschopp *et al.*: [115]

- Generally, GB sites exhibit a significant lower vacancy formation energies compared to those in bulk, suggesting that these sites will capture and thus annihilate radiation-induced point defects.
- Both low-angle and high-angle GBs are effective in terms of annihilating point defects, but high-angle GBs are more efficient in that.
- With increasing misorientation angle or GB energy, the point defect formation energy is decreasing.
- Simulations have shown that GBs are biased defect sinks: interstitials have a greater tendency to segregate to the GBs rather then vacancies. Long-term radiation will also affect the atomic configuration of the GBs and thus change the selective absorption of interstitials.

However, there is another important factor regarding the stability of the microstructure under irradiation, which is the motion of grain boundary movement. Molecular dynamics simulations have shown that grain boundaries can undergo movement under irradiation conditions if the volume affected by the thermal spike exceeds the volume of the grain [116].

The importance of the microstructural stability and size is also supported by ion irradiation on Au foams, as such foams exhibit a high surface to volume ratio and suggesting a superior radiation-resistant material. However, it was concluded that not all nanoporous materials are radiation tolerant, and only a small parameter window exist where these foams show radiation resistance. When the size of the ligaments is too big, the material will behave similar to bulk material and radiation-induced point defects will accumulate and not annihilate. If the ligament is too small in size, planar defects, breaking and even melting is observed [117, 118].

To summarize, the microstructure plays a pivotal role on the radiation-resistance of a given material. A synergistic interaction between the number of grain boundaries (*i.e. grain size*) and their characteristics determines the radiation-resistance of any given material. Therefore, it is crucial to maintain a grain size, which is small enough to annihilate radiation-induced point defects, but big enough to mitigate the thermal spike resulting from radiation.

## 2.5 Reference

[1] Suhas Eswarappa Prameela, Tresa M Pollock, Dierk Raabe, Marc André Meyers, Assel Aitkaliyeva, Kerri-Lee Chintersingh, Zachary C Cordero, and Lori Graham-Brady. Materials for extreme environments. *Nature Reviews Materials*, 8(2):81–88, 2023.

[2] Muntazir Abbas and Mahmood Shafiee. An overview of maintenance management strategies for corroded steel structures in extreme marine environments. *Marine Structures*, 71:102718, 2020.

[3] William G Fahrenholtz and Greg E Hilmas. Ultra-high temperature ceramics: Materials for extreme environments. *Scripta Materialia*, 129:94–99, 2017.

[4] Russell J Hemley, George W Crabtree, and Michelle V Buchanan. Materials in extreme environments. *Physics Today*, 62(11):32–37, 2009.

[5] William David Compton. *Where no man has gone before: A history of Apollo lunar exploration missions*, volume 4214. US Government Printing Office, 1989.

[6] John B Rittenhouse and John B Singletary. Space materials handbook. Technical report, National Aeronautics and Space Administration, 1969.

[7] Omid Karimzade Soureshjani, Ali Massumi, and Gholamreza Nouri. Sustainable colonization of Mars using shape optimized structures and in situ concrete. *Scientific Reports*, 13(1):15747, 2023.

[8] William Dobney, Louise Mols, Dhruti Mistry, Kevin Tabury, Bjorn Baselet, and Sarah Baatout. Evaluation of deep space exploration risks and mitigations against radiation and microgravity. *Frontiers in Nuclear Medicine*, 3, 2023.

[9] Yifan Lu, Qi Shao, Honghao Yue, and Fei Yang. A review of the space environment effects on spacecraft in different orbits. *IEEE access*, 7:93473–93488, 2019.

[10] Daniel K Schreiber, Ruth Schwaiger, Martin Heilmaier, and Scott J McCormack. Materials properties characterization in the most extreme environments. *MRS Bulletin*, 47(11):1128–1142, 2022.

[11] Gerhard Drolshagen. Impact effects from small size meteoroids and space debris. *Advances in Space Research*, 41(7):1123–1131, 2008.

[12] William J Tedeschi, Cdr John C Connell, Darren S McKnight, Firooz Allahdadi, Al Reinhardt, Ronald D Hunt, and David M Hogg. Determining the effects of space debris impacts on spacecraft structures. *Acta Astronautica*, 26(7): 501–512, 1992.

[13] T Asavei, M Tomut, M Bobeica, S Aogaki, MO Cernaianu, M Ganciu, S Kar, G Manda, N Mocanu, L Neagu, et al. Materials in extreme environments for energy, accelerators and space applications at ELI-NP. *Rom. Rep. Phys*, 68: S275–S347, 2016.

[14] Marco Durante. Space radiation protection: destination Mars. *Life Sciences in Space Research*, 1:2–9, 2014.

[15] Arnold Hanslmeier. The sun and space weather. In *Heliophysical Processes*, pages 233–249. Springer, 2010.

[16] Ezequiel Echer, WD Gonzalez, Fernando Luiz Guarnieri, A Dal Lago, and LEA Vieira. Introduction to space weather. *Advances in Space Research*, 35 (5):855–865, 2005.

[17] Mark Moldwin. *An Introduction to Space Weather*. Cambridge University Press, 2022.

[18] DN Baker. What is space weather? *Advances in Space Research*, 22(1):7–16, 1998.

[19] JP Eastwood, E Biffis, MA Hapgood, L Green, MM Bisi, RD Bentley, Robert Wicks, L-A McKinnell, M Gibbs, and C Burnett. The economic impact of space weather: Where do we stand? *Risk Analysis*, 37(2):206–218, 2017.

[20] Jonathan P Eastwood. The science of space weather. *Philosophical Transactions of the Royal Society A: Mathematical, Physical and Engineering Sciences*, 366 (1884):4489–4500, 2008.

[21] Rainer Schwenn. Space weather: The solar perspective. *Living Reviews in Solar Physics*, 3(1):1–72, 2006.

[22] Roberta Piccinelli and Elisabeth Krausmann. North Europe power transmission system vulnerability during extreme space weather. *Journal of Space Weather and Space Climate*, 8:A03, 2018.

[23] Steven K Morley. Challenges and opportunities in magnetospheric space weather prediction. *Space Weather*, 18(3):e2018SW002108, 2020.

[24] Joan Feynman and SB Gabriel. On space weather consequences and predictions. *Journal of Geophysical Research: Space Physics*, 105(A5):10543–10564, 2000.

[25] Space.com. Aurora Borealis. Available at: https://www.space.com/15139-northern-lights-auroras-earth-facts-sdcmp.html. Accessed: 14.03.2024.

[26] ESA.int. Solar Flare. Available at: https://www.esa.int/Science_Exploration/Space_Science/What_are_solar_flares. Accessed: 14.03.2024.

[27] Earthsky.org. Coronal Mass Ejection. Auvailable at: https://earthsky.org/space/what-are-coronal-mass-ejections/. Accessed: 14.03.2024.

[28] Steven R Cranmer, Sarah E Gibson, and Pete Riley. Origins of the ambient solar wind: implications for space weather. *Space Science Reviews*, 212:1345–1384, 2017.

[29] Manuela Temmer. Space weather: The solar perspective: An update to Schwenn (2006). *Living Reviews in Solar Physics*, 18(1):4, 2021.

[30] Tanveer Ahmad and Dongdong Zhang. A critical review of comparative global historical energy consumption and future demand: The story told so far. *Energy Reports*, 6:1973–1991, 2020.

[31] Lawrence W Townsend. Space weather on the Moon. *Physics Today*, 73(3): 66–67, 2020.

[32] Heiner Klinkrad. *Space debris: models and risk analysis.* Springer Science & Business Media, 2006.

[33] VV Adushkin, O Yu Aksenov, SS Veniaminov, SI Kozlov, and VV Tyurenkova. The small orbital debris population and its impact on space activities and ecological safety. *Acta Astronautica*, 176:591–597, 2020.

[34] Shenyan Chen. The space debris problem. *Asian Perspective*, 35(4):537–558, 2011.

[35] Donald J Kessler, Nicholas L Johnson, JC Liou, and Mark Matney. The kessler syndrome: implications to future space operations. *Advances in the Astronautical Sciences*, 137(8):2010, 2010.

[36] Amrith Mariappan and John L Crassidis. Kessler's syndrome: a challenge to humanity. *Frontiers in Space Technologies*, 4:1309940, 2023.

[37] John Wallington Glen. A survey of irradiation effects in metals. *Advances in Physics*, 4(16):381–477, 1955.

[38] Mark T Robinson. Basic physics of radiation damage production. *Journal of Nuclear Materials*, 216:1–28, 1994.

[39] E Friedland. Radiation damage in metals. *Critical Reviews in Solid State and Material Sciences*, 26(2):87–143, 2001.

[40] Frederick Seitz. On the disordering of solids by action of fast massive particles. *Discussions of the Faraday Society*, 5:271–282, 1949.

[41] Kai Nordlund, Andrea E Sand, Fredric Granberg, Steven J Zinkle, Roger Stoller, Robert S Averback, Tomoaki Suzudo, Lorenzo Malerba, Florian Banhart, William J Weber, et al. Primary radiation damage in materials. *Review of Current Understanding and Proposed New Standard Displacement Damage Model to Incorporate in Cascade Defect Production Efficiency and Mixing Effects*, 2015.

[42] GS Was. *Fundamentals of Radiation Materials Science: Metals and Alloys*. Springer, 2007.

[43] A Ballesteros, Ralf Ahlstrand, Christiane Bruynooghe, A Chernobaeva, Y Kevorkyan, D Erak, and D Zurko. Irradiation temperature, flux and spectrum effects. *Progress in Nuclear Energy*, 53(6):756–759, 2011.

[44] Jingjing Yu and Xiaomei Li. Modelling of the precipitated phases and properties of Al-Zn-Mg-Cu alloys. *Journal of Phase Equilibria and Diffusion*, 32:350–360, 2011.

[45] Byeong-Hyeon Lee, Sung-Hoon Kim, Jun-Hyoung Park, Hyung-Wook Kim, and Jae-Chul Lee. Role of Mg in simultaneously improving the strength and

ductility of Al–Mg alloys. *Materials Science and Engineering: A*, 657:115–122, 2016.

[46] EL Huskins, B Cao, and KT Ramesh. Strengthening mechanisms in an Al–Mg alloy. *Materials Science and Engineering: A*, 527(6):1292–1298, 2010.

[47] Wei Wen, Yumin Zhao, and JG Morris. The effect of Mg precipitation on the mechanical properties of 5xxx aluminum alloys. *Materials Science and Engineering: A*, 392(1-2):136–144, 2005.

[48] TC Schulthess, PEA Turchi, A Gonis, and T-G Nieh. Systematic study of stacking fault energies of random Al-based alloys. *Acta Materialia*, 46(6): 2215–2221, 1998.

[49] Eric M Taleff, Donald R Lesuer, and Jeffrey Wadsworth. Enhanced ductility in coarse-grained Al-Mg alloys. *Metallurgical and Materials Transactions A*, 27:343–352, 1996.

[50] ECW Perryman and GB Brook. Mechanism of Precipitation in Aluminium-Magnesium Alloys. *J. Inst. Metals*, 79:19–34, 1951.

[51] Cheng Cao, Di Zhang, Zhanbing He, Linzhong Zhuang, and Jishan Zhang. Enhanced and accelerated age hardening response of Al-5.2 Mg-0.45 Cu (wt%) alloy with Zn addition. *Materials Science and Engineering: A*, 666:34–42, 2016.

[52] XB Yang, JH Chen, JZ Liu, F Qin, J Xie, and CL Wu. A high-strength AlZnMg alloy hardened by the T-phase precipitates. *Journal of Alloys and Compounds*, 610:69–73, 2014.

[53] R Zhang, MA Steiner, SR Agnew, SK Kairy, CHJ Davies, and N Birbilis. Experiment-based modelling of grain boundary $\beta$-phase ($Mg_2Al_3$) evolution during sensitisation of aluminium alloy aa5083. *Scientific Reports*, 7(1):2961, 2017.

[54] Chunyan Meng, Di Zhang, Hua Cui, Linzhong Zhuang, and Jishan Zhang. Mechanical properties, intergranular corrosion behavior and microstructure of

Zn modified Al–Mg alloys. *Journal of Alloys and Compounds*, 617:925–932, 2014.

[55] Lukas Stemper, Matheus A Tunes, Paul Oberhauser, Peter J Uggowitzer, and Stefan Pogatscher. Age-hardening response of AlMgZn alloys with Cu and Ag additions. *Acta Materialia*, 195:541–554, 2020.

[56] MC Carroll, PI Gouma, MJ Mills, GS Daehn, and BR Dunbar. Effects of Zn additions on the grain boundary precipitation and corrosion of Al-5083. *Scripta Materialia*, 42(4):335–340, 2000.

[57] Cheng Guo, Haitao Zhang, and Jiehua Li. Influence of Zn and/or Ag additions on microstructure and properties of Al-Mg based alloys. *Journal of Alloys and Compounds*, 904:163998, 2022.

[58] Boyu Xue, Wei Xiao, Xiwu Li, Guanjun Gao, Xiaowu Li, Yongan Zhang, Ligen Wang, and Baiqing Xiong. Comprehensive investigation on the structural, electronic and mechanical properties of T-$Mg_{32}(Al,Zn)_{49}$ phases in Al-Mg-Zn alloys. *Journal of Materials Science & Technology*, 173:237–246, 2024.

[59] Cheng Cao, Di Zhang, Xu Wang, Qibiao Ma, Linzhong Zhuang, and Jishan Zhang. Effects of Cu addition on the precipitation hardening response and intergranular corrosion of Al-5.2 Mg-2.0 Zn (wt.%) alloy. *Materials Characterization*, 122:177–182, 2016.

[60] Hiroki Ishii, Rikito Takagi, Naoki Takata, Asuka Suzuki, and Makoto Kobashi. Influence of Added Fourth Elements on Precipitation in Heat-Resistant Al–Mg–Zn Ternary Alloys. *Materials Transactions*, 63(4):513–521, 2022.

[61] Jianwen Mao, Shengping Wen, Shangshang Liang, Xiaolan Wu, Wu Wei, Hui Huang, Kunyuan Gao, and Zuoren Nie. Precipitation behaviors and thermal stability of Al-3.5 Mg-1.0 Cu alloy with co-addition of Zn and Si. *Journal of Alloys and Compounds*, 946:169401, 2023.

[62] Yingxin Geng, Qi Song, Zhaorui Zhang, Yanlin Pan, Hongxiang Li, Yuan Wu, Huihui Zhu, Di Zhang, Jishan Zhang, and Linzhong Zhuang. Quantifying early-stage precipitation strengthening of Al–Mg–Zn (-Cu) alloy by using particle size distribution. *Materials Science and Engineering: A*, 839:142851, 2022.

[63] Haoran Liu, Zhen Zhang, Di Zhang, and Jishan Zhang. The effect of Ag on the tensile strength and fracture toughness of novel Al-Mg-Zn alloys. *Journal of Alloys and Compounds*, 908:164640, 2022.

[64] Yukuan Huang, Yu Liu, Zhengbing Xiao, and Yuanchun Huang. A trade-off between mechanical strength and electrical conductivity of Al–Zn–Mg–Cu alloy via Ag alloying and retrogression re-aging heat treatment. *Materials Science and Engineering: A*, 880:145230, 2023.

[65] Nasser Afify, Abdel-Fattah Gaber, Ghada Abbady, et al. Fine scale precipitates in Al-Mg-Zn alloys after various aging temperatures. *Materials Sciences and Applications*, 2(05):427, 2011.

[66] Cheng Cao, Di Zhang, Linzhong Zhuang, and Jishan Zhang. Improved age-hardening response and altered precipitation behavior of Al-5.2 Mg-0.45 Cu-2.0 Zn (wt%) alloy with pre-aging treatment. *Journal of Alloys and Compounds*, 691:40–43, 2017.

[67] Yafei Wang, Bhupendra Sharma, Yuantao Xu, Kazuyuki Shimizu, Hiro Fujihara, Kyosuke Hirayama, Akihisa Takeuchi, Masayuki Uesugi, Guangxu Cheng, and Hiroyuki Toda. Switching nanoprecipitates to resist hydrogen embrittlement in high-strength aluminum alloys. *Nature Communications*, 13(1):6860, 2022.

[68] Matheus A Tunes, Lukas Stemper, Graeme Greaves, Peter J Uggowitzer, and Stefan Pogatscher. Prototypic Lightweight Alloy Design for Stellar-Radiation Environments. *Advanced Science*, 7(22):2002397, 2020.

[69] Lukas Stemper, Matheus A Tunes, Ramona Tosone, Peter J Uggowitzer, and Stefan Pogatscher. On the potential of aluminum crossover alloys. *Progress in Materials Science*, 124:100873, 2022.

[70] Sebastian Samberger, Irmgard Weißensteiner, Lukas Stemper, Christina Kainz, Peter J Uggowitzer, and Stefan Pogatscher. Fine-grained aluminium crossover alloy for high-temperature sheet forming. *Acta Materialia*, 253:118952, 2023.

[71] W Lohmann, A Ribbens, WF Sommer, and BN Singh. Microstructure and mechanical properties of medium energy (600-800 MeV) proton irradiated commercial aluminium alloys. *Radiation Effects*, 101(1-4):283–299, 1987.

[72] Bachu Narain Singh, Torben Leffers, M Victoria, WV Green, and D Gavillet. Effects of 600 mev proton irradiation on nucleation and growth of precipitates and helium bubbles in a high-purity Al-Mg-Si alloy. *Journal of Nuclear Materials*, 141:743–747, 1986.

[73] Bachu Narain Singh, Torben Leffers, WV Green, and M Victoria. Nucleation of helium bubbles on dislocations, dislocation networks and dislocations in grain boundaries during 600 MeV proton irradiation of aluminium. *Journal of Nuclear Materials*, 125(3):287–297, 1984.

[74] KS Liu, O Kawano, Y Murakami, and H Yoshida. Structural changes in age-hardenable aluminium alloys induced by low temperature neutron irradiation. *Radiation Effects*, 15(1-2):37–49, 1972.

[75] Camille Flament, Joel Ribis, Jérôme Garnier, Y Serruys, F Leprêtre, A Gentils, C Baumier, M Descoins, D Mangelinck, A Lopez, et al. Stability of $\beta$ nano-phases in Al-Mg-Si (-Cu) alloy under high dose ion irradiation. *Acta Materialia*, 128:64–76, 2017.

[76] Tom Petit, Claire Ritter, Jacques Besson, and Thilo F Morgeneyer. Effects of neutron irradiation and post-irradiation annealing on pop-in crack propagation instabilities in 6061 aluminium alloy. *Journal of Nuclear Materials*, 569:153909, 2022.

[77] LE Katz, H Herman, and AC Damask. Precipitation in neutron-irradiated Al-base Cu. *Acta Metallurgica*, 16(7):939–945, 1968.

[78] K Farrell and RT King. Radiation-induced strengthening and embrittlement in aluminum. *Metallurgical Transactions*, 4:1223–1231, 1973.

[79] P Bhattacharyya, N Gayathri, M Bhattacharya, A Dutta Gupta, Apu Sarkar, S Dhar, MK Mitra, and P Mukherjee. Proton irradiation studies on Al and Al5083 alloy. *Radiation Physics and Chemistry*, 139:132–140, 2017.

[80] Yan Zhanfeng, Zheng Jian, Zhou Wei, and Wang Hao. The self-ion irradiation effects in 6061-Al alloy. , 34(5):056008–1, 2022.

[81] ZH Ismail. Effect of low dose neutron irradiation on the mechanical properties of an AlMgSi alloy. *Radiation Effects and Defects in Solids*, 112(4):105–110, 1990.

[82] ZH Ismail and B Birt. Post-irradiation mechanical properties of an AlMgSi alloy. *Journal of Nuclear Materials*, 218(3):289–292, 1995.

[83] VV Ovchinnikov, NV Gushchina, FF Makhin'ko, LS Chemerinskaya, AR Shkol'nikov, SM Mozharovskii, AV Filippov, and LI Kaigorodova. Structural features of aluminium alloy 1441 irradiated by Ar+ ions. *Russian Physics Journal*, 50:177–186, 2007.

[84] B Jahnke and K Ehrlich. Void formation in an Al-Mg-Si alloy under different precipitation conditions after irradiation with 100 keV Al ions. *Journal of Materials Science*, 15:831–838, 1980.

[85] Bachu Narain Singh, Andy Horsewell, WF Sommer, and W Lohmann. Gas accumulation at grain boundaries during 800 MeV proton irradiation of aluminium and aluminium-alloys. *Journal of Nuclear Materials*, 141:718–722, 1986.

[86] U Engman and B Holmqvist. Electron microscopy studies of void swelling and annealing of voids in aluminium irradiated with aluminium ions. *Radiation Effects*, 47(1-4):189–193, 1980.

[87] DJ Mazey, R Bullough, and AD Brailsford. Observation and analysis of damage structure in Al and Al/Mg (N4) alloy after irradiation with 100 and 400 keV aluminium ions. *Journal of Nuclear Materials*, 62(1):73–88, 1976.

[88] Sarah L'haridon Quaireau, Kimberly Colas, Bénédicte Kapusta, Bénédicte Verhaeghe, Marie Loyer-Prost, Gaëlle Gutierrez, Dominique Gosset, and Sylvie Delpech. Impact of ion and neutron irradiation on the corrosion of the 6061-T6 aluminium alloy. *Journal of Nuclear Materials*, 553:153051, 2021.

[89] Mojtaba Bagherzadeh, Meysam Karimi, Mohammad Hosein Choopan Dastjerdi, Mohsen Asadi Asadabad, Javad Mokhtari, and Afshin Babanejhad. Long-time irradiation effect on corrosion behavior of aluminum alloy in pool water of low-power research reactor. *Scientific Reports*, 13(1):17007, 2023.

[90] Kotchaphan Kanjana and Jatechan Channuie. Corrosion of neutron/gamma-irradiated aluminium alloy 6061. *Songklanakarin Journal of Science & Technology*, 41(2), 2019.

[91] Elisa Canepa, Roberto Stifanese, Lorenzo Merotto, and Pierluigi Traverso. Corrosion behaviour of aluminium alloys in deep-sea environment: A review and the KM3NeT test results. *Marine Structures*, 59:271–284, 2018.

[92] JFG Conde and DJ Godfrey. Materials for extreme environments. *Journal of the Royal Naval Scientific Service*, page 111, 2009.

[93] Renjish Vijay, VN Aju Kumar, A Sadiq, and Lijin Thomas. Influence of cryogenic treatment on bulk and surface properties of aluminium alloys: a review. *Advances in Materials and Processing Technologies*, 8(4):4335–4346, 2022.

[94] EO Hall. The deformation and ageing of mild steel: III discussion of results. *Proceedings of the Physical Society. Section B*, 64(9):747, 1951.

[95] Norman J Petch. The cleavage strength of polycrystals. *J. Iron Steel Inst.*, 174:25–28, 1953.

[96] Vladimir Bata and Elena V Pereloma. An alternative physical explanation of the hall–petch relation. *Acta Materialia*, 52(3):657–665, 2004.

[97] ZN Farhat, Y Ding, DO Northwood, and AT Alpas. Effect of grain size on friction and wear of nanocrystalline aluminum. *Materials Science and Engineering: A*, 206(2):302–313, 1996.

[98] Anthony Wayne Thompson and WA Backofen. The effect of grain size on fatigue. *Acta Metallurgica*, 19(7):597–606, 1971.

[99] Arvind R Kalidindi, Tongjai Chookajorn, and Christopher A Schuh. Nanocrystalline materials at equilibrium: a thermodynamic review. *Jom*, 67:2834–2843, 2015.

[100] Markus Ames, Jürgen Markmann, Rudolf Karos, Andreas Michels, Andreas Tschöpe, and Rainer Birringer. Unraveling the nature of room temperature grain growth in nanocrystalline materials. *Acta Materialia*, 56(16):4255–4266, 2008.

[101] Heather A Murdoch and Christopher A Schuh. Stability of binary nanocrystalline alloys against grain growth and phase separation. *Acta Materialia*, 61 (6):2121–2132, 2013.

[102] Kaveh Edalati, Andrea Bachmaier, Victor A Beloshenko, Yan Beygelzimer, Vladimir D Blank, Walter J Botta, Krzysztof Bryła, Jakub Čížek, Sergiy Divinski, Nariman A Enikeev, et al. Nanomaterials by severe plastic deformation: review of historical developments and recent advances. *Materials Research Letters*, 10(4):163–256, 2022.

[103] Kaveh Edalati and Zenji Horita. A review on high-pressure torsion (HPT) from 1935 to 1988. *Materials Science and Engineering: A*, 652:325–352, 2016.

[104] Ghader Faraji and Hesam Torabzadeh. An overview on the continuous severe plastic deformation methods. *Materials Transactions*, 60(7):1316–1330, 2019.

[105] Kaveh Edalati, Junko Matsuda, Akira Yanagida, Etsuo Akiba, and Zenji Horita. Activation of TiFe for hydrogen storage by plastic deformation using groove rolling and high-pressure torsion: Similarities and differences. *International Journal of Hydrogen Energy*, 39(28):15589–15594, 2014.

[106] Herbert Gleiter. Nanostructured materials: basic concepts and microstructure. *Acta Materialia*, 48(1):1–29, 2000.

[107] H Gleiter. Nanostructured materials. In *Mechanical Properties and Deformation Behavior of Materials Having Ultra-Fine Microstructures*, pages 3–35. Springer, 1993.

[108] Manohar PA, M Ferry, and T Chandra. Five decades of the Zener equation. *ISIJ International*, 38(9):913–924, 1998.

[109] VL Tellkamp, EJ Lavernia, and A Melmed. Mechanical behavior and microstructure of a thermally stable bulk nanostructured Al alloy. *Metallurgical and Materials Transactions A*, 32:2335–2343, 2001.

[110] H Asgharzadeh and HJ McQueen. Grain growth and stabilisation of nanostructured aluminium at high temperatures. *Materials Science and Technology*, 31(9):1016–1034, 2015.

[111] BO Han, EJ Lavernia, Z Lee, S Nutt, and D Witkin. Deformation behavior of bimodal nanostructured 5083 Al alloys. *Metallurgical and Materials Transactions A*, 36:957–965, 2005.

[112] BN Singh. On the influence of grain boundaries on void growth. *Philosophical Magazine*, 28(6):1409–1413, 1973.

[113] M Rose, AG Balogh, and HJNI Hahn. Instability of irradiation induced defects in nanostructured materials. *Nuclear Instruments and Methods in Physics Research Section B: Beam Interactions with Materials and Atoms*, 127:119–122, 1997.

[114] Xinghang Zhang, Khalid Hattar, Youxing Chen, Lin Shao, Jin Li, Cheng Sun, Kaiyuan Yu, Nan Li, Mitra L Taheri, Haiyan Wang, et al. Radiation damage in nanostructured materials. *Progress in Materials Science*, 96:217–321, 2018.

[115] Mark A Tschopp, KN Solanki, Fei Gao, Xin Sun, Mohammad A Khaleel, and MF Horstemeyer. Probing grain boundary sink strength at the nanoscale: Energetics and length scales of vacancy and interstitial absorption by grain boundaries in $\alpha$-Fe. *Physical Review B*, 85(6):064108, 2012.

[116] Wolfgang Voegeli, Karsten Albe, and Horst Hahn. Simulation of grain growth in nanocrystalline nickel induced by ion irradiation. *Nuclear Instruments and Methods in Physics Research Section B: Beam Interactions with Materials and Atoms*, 202:230–235, 2003.

[117] Eduardo Marcial Bringa, JD Monk, A Caro, A Misra, L Zepeda-Ruiz, M Duchaineau, F Abraham, Michael Nastasi, ST Picraux, YQ Wang, et al. Are nanoporous materials radiation resistant? *Nano Letters*, 12(7):3351–3355, 2012.

[118] LS Novikov, EN Voronina, and NP Chirskaya. Features of radiation impact on nanostructured materials. *Inorganic Materials: Applied Research*, 5:107–115, 2014.

# Chapter 3

# Materials, methodology and approach

This section gives a brief overview on the materials synthesis' and some applications, which were used during the experiments.

## 3.1 Alloy synthesis

Based on previous research activities on the new emerging Al crossover series, a compositional merge between a 5xxx and 7xxx series alloy was used. The nominal chemical composition is listed below in Table 3.1. Significantly, maintaining a Zn/Mg ratio below 1 is recognized as crucial for the precipitation of T-phase precipitates [1]. The alloys under investigation consistently adhere to this parameter.

Table 3.1: Nominal chemical composition of the investigated alloys in this thesis. Chemical composition was determined using optical emission spectroscopy.

| | VL1 | VL2 | VL3 | VL4 |
|---|---|---|---|---|
| Mg | 4.8 | 4.8 | 4.8 | 4.8 |
| Zn | 3.7 | 3.7 | 3.7 | 3.7 |
| Cu | - | - | 0.6 | 0.6 |
| Ag | - | 0.17 | - | 0.17 |
| Al | bal. | bal. | bal. | bal. |

## 3.2 Differential scanning calorimetry

The usage of differential scanning calorimetry (DSC) is widespread. These kind of experiments offers the user quantitative calorimetric information of a given sample. Within this technique, a linear heating ramp is applied into both a reference and a sample, which is chosen by the use [2]. While these two samples are subjected to a controlled temperature program, the heat flow rate difference of them is measured. The final thermal analysis is able to reveal various characteristic temperatures, such as: [2]

- heat capacity,
- melting temperature,
- recrystallization temperature and
- heat of fusion, etc.

One of the biggest advantages of the DSC is the small amount of samples needed for measurements. For quantitative and statistical analysis, less then 1 g of sample is needed, which makes it very useful when only limited or small samples are available. However, with evolving technology, the DSC has also gained from technological advancements. The so-called *Flash DSC* allows to reduce the sample size and thus the sample mass even further to the nanogram regime [7], which also makes its handling more complicated. Therefore, the DSC is a good compromise between easy usage and small amounts of samples needed. It is important to comprehend that temperature is the most important quantity in DSC measurements: temperature is the only measured value. From there, all other values are calculated, which makes the precise measurement of the temperature invaluable. In fact, temperature is a thermodynamic parameter of a system, which describes the average kinetic energy of the atoms within this system. However, it is only possible to describe temperature for equilibrium systems only [2]. The zeroth law of thermodynamics describes the term temperature: When two systems are each in thermal equilibrium with a third system, then they are in thermal equilibrium with each other [8]. While the zeroth law of thermodynamics only provides an understanding of the terminology temperature, the second law of thermodynamics helps to mathematically express the temperature.

### 3.2.1 Principles of the differential scanning calorimetry

To comprehend the principles of the measurements within the DSC, the easiest reaction will be considered: determination of a phase transformation. During the heating process, a common heat flow flows from the oven into both the sample and the reference. If no reaction takes place, both have the same thermal properties and the system is symmetrical, which means that the sample and the reference heat up the same time. Therefore, the heat flow is identical and the measured temperature difference at the sensor is zero. In case a reaction appears within the sample, the temperature at the sample side is different to the temperature at the reference and thus, the heat flow is not zero anymore. However, in reality, the temperature difference between reference and sample is never zero, even when no reaction is happening. This is due to the different heat capacity of the materials. However, this makes it possible to analyze thermal properties. The raw data acquired from the DSC measurements is the temporal change in the thermoelectric voltages. Through a sensitivity calibration, the real heat flow in mW/mg can be displayed. The area under any peak responds to the change of enthalpy of the system. [9] Its principles are displayed in Figure 3.1.

### 3.2.2 Parameters of the measurements

Even though only temperature is measured, several important parameters are calculated from this, which the most important ones will be discussed in this section.

**Heat flow** Since heat is a form of energy, and energy transfers from a higher-temperature system to a lower-temperature system, it can be considered as a heat flow. Thermal equilibrium is then reached when the temperature of both systems become equal. [2]. Simplified, when no work is taken into account, and the process occurs at constant volume, the internal energy U is equal to the amount of heat

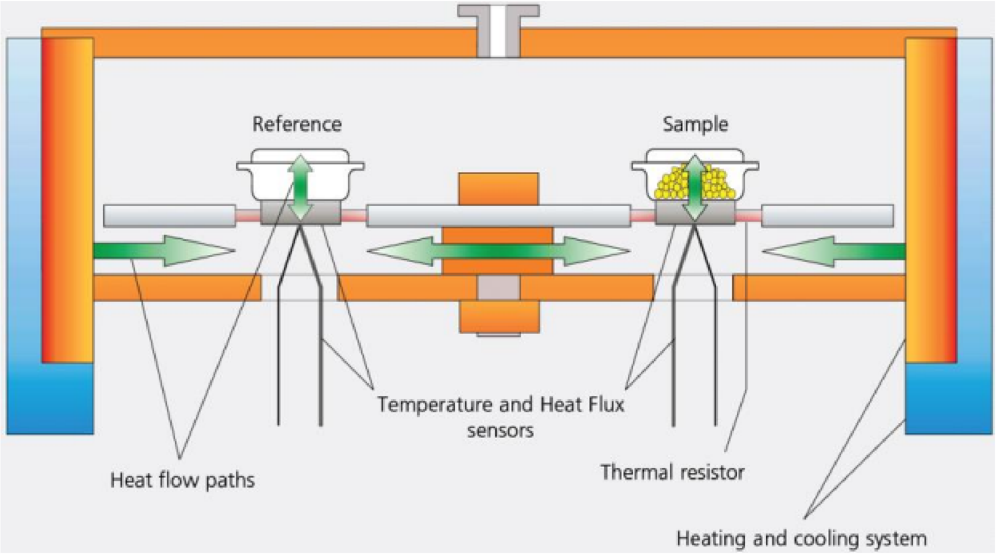

Figure 3.1: Principles of the heat flow signal obtained from a DSC. [10]

added to the system or extracted from it, and thus, the heat Q becomes a function of state. There are three major forms of heat flow: [2, 3]

- *Conduction*: heat travels from the hotter system to the colder system. This is possible within one system or via the physical contact of two individual systems.
- *Convection*: heat can be transferred via the surface to its surroundings or vice versa.
- *Thermal radiation*: electromagnetic energy is radiated from the surface of the system to its surrounding. The frequency and intensity is depending on the surface temperature.

**Latent heat** The Latin word *latent* means ”existing but concealed” and is related to the energy which is released or absorbed during phase transitions, for example, melting. During this process, the temperature of the material does not change. Another common wording for latent heat is *heat of transition*. [4]

**Enthalpy** The enthalpy increase of systems in equilibrium processes is identical to the heat added to the system. However, it must be noted that normally only enthalpy changes are measured. Within the DSC, this change is calculated from the difference between the sample and the reference. [5]

**Heat capacity** The heat capacity can be calculated at constant pressure ($C_p$) or constant volume ($C_V$), but this can only be calculated in the absence of chemical reactions or phase transitions. Then, the amplitude of the heat flow signal is directly correlated with the heat capacity at constant pressure. This is described in Equation 3.1. [6]

$$C_P \equiv (\frac{\partial Q}{\partial T})_P \equiv (\frac{\partial H}{\partial T})_P \tag{3.1}$$

**Phase Transitions** They can be classified in two types: first-order and second-order transitions. First-order transitions are those, where the partial derivative of the free energy (e.g., volume, entropy, enthalpy) with a thermodynamic variable (e.g., temperature, pressure) signals discontinuity. Thus, melting, evaporation, sublimation, crystallization, condensation or deposition can be named. In contrast, second-order transitions are found when the aforementioned first derivatives are continuous but a second partial derivative of the free energy exhibits discontinuity. So, a jump in the heat flow signal of the DSC is equal to a second-order transition. [11]

## 3.3 Transmission electron microscopy

A (scanning) transmission electron microscope (S/TEM) is an advanced instrument to observe and characterise the microstructure of a given material in detail. This paragraph covers the fundamentals of the imaging techniques and covers the basics of different working techniques.

### 3.3.1 Working principle of the transmission electron microscopy

A series of magnetic lenses is used to focus an electron beam, which is accelerated by a high potential. This is illustrated in Figure 3.2. A X-FEG filament is placed behind a Wehnelt cap with a hole and is electrically heated. Electrons emitted by the

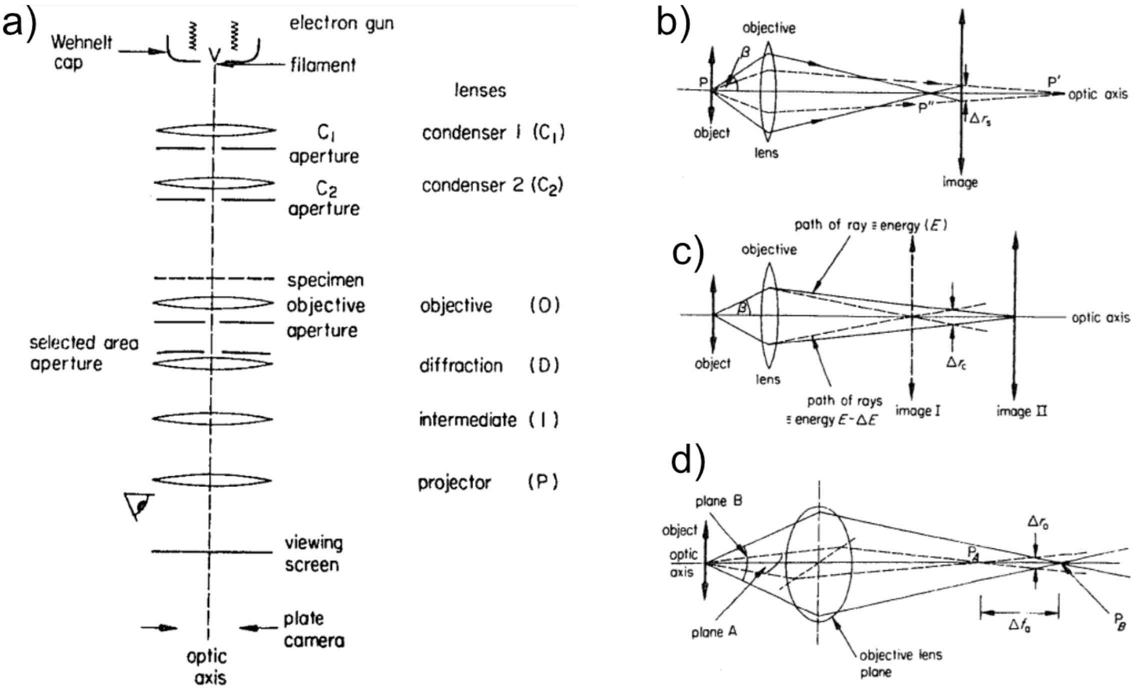

Figure 3.2: Schematic illustration of the Transmission Electron Microscope. a) displays the working principle with the most important parts of the TEM. The lens defects are illustrated from b) to d), with b) showing the spherical, c) chromatic and d) astigmatism aberrations. [12]

filament are accelerated to earth potential. A double condenser lens system is used to focus the electrons under vacuum. The image or diffraction pattern is obtained from the interaction between the electrons and the specimen is then formed on a fluorescent screen. An objective lens can be used to enhance the contrast of the sample, while the use of a selected area aperture allows the selection of the area of diffraction on the sample. The objective lens is used to focus the image, while the magnification is controlled by excitation of the intermediate lens. [12] However, the lenses used in the TEM are not perfect and therefore, the performance of the lenses is limited as they all have lens defects. When working with a TEM, it is important to calibrate and align the beam accordingly, to reduce the influence of these limitations and to enhance the results from the experiments.

Given the critical nature of lens defects and their corrections, the following section is looking into the origins of these issues and strategies to mitigate their impact. From the operator's point-of-view, the most important ones are spherical, chromatic aberration and astigmatism, as they can significantly enhance or decrease the resolution of the microscope.

**Spherical aberration** A graphical explanation is given in Figure 3.2 b). Electrons departing from point P along the optic axis of the specimen are redirected and refocused at point P" rather than P'. Consequently, the imaged point in the image plane appears as a disc. The radius of this disc can be calculated using the following equation Equation 3.2: [12]

$$\Delta r_s = C_s \cdot \beta^3 \tag{3.2}$$

$C_s$ is the spherical aberration constant (typically 1 or 2 mm for objective lens), while $\beta$ expresses the aperture size. Given from Equation 3.2, the radius of the disc increases to the power of 3 upon increasing the size of the aperture. A small aperture is able to allow for better imaging conditions. Unfortunately, there is no convenient methodology to correct it. Therefore, the spherical aberration is the most limiting parameter within electron microscopes [12, 13]. With the advent of the so-called spherical aberration corrected TEM ($C_s$-corrected TEM), a point resolution of less than 0.10 nm is achievable and allows for high-resolution imaging and analysis. [14]

**Chromatic aberration** This arises due to different factors, such as wavelength (and thus the energy), instabilities of the accelerating voltage or lens current. The energy spread of approximately 0.8 eV of emitted electrons of the filament is rather small compared to the energy loss of up to 50 eV, when the electrons pass through the specimen. Therefore, the focal length of lens varies with the electron energy, as displayed in Figure 3.2 c). [12]

**Astigmatism** This phenomenon arises when the lens demonstrates varying focal lengths based on the path of the rays through it. This is shown in Figure 3.2 d): the rays travelling in plane A are converged at point $P_A$ while the rays travelling in plane B are focused at point $P_B$. Thus, a point on the specimen is then imaged as a disc. However, this can easily be corrected when electromagnetic astigmators are used, which produce a small variable magnetic field. While condenser astigmatism diminishes beam coherence, resulting in an elliptical spot, objective astigmatism can significantly reduce resolution, causing streaking in one direction of fine details in the image. The condenser astigmatism is adjusted to make the spot as circular as possible, while the objective astigmatism is aligned using Fresnel fringes near edges of a hole. [12]

When the above-mentioned aberrations are accordingly aligned and reduced, this can significantly enhance the image resolution. However, there are another two important types of resolution: first, the instrument resolution, and second, the specimen resolution.

**Instrument resolution** The resolution of the instrument can be considered as a function of aberrations of the objective lens. Employing a small aperture can enhance resolution; however, if the aperture size is diminished excessively, diffraction effects at the aperture can become a limiting factor. Diffraction of the lens aperture causes a point source to be imagined as a disc – known as Airy's disc – surrounded by a number of fainter rings. The Rayleigh criterion describes the distance between two distinguishable points and depends on the wave-length (and thus the energy) and also by the inverse size of the aperture. The Rayleigh criterion is given in Equation 3.3, with $\lambda$ expressing the wavelength. Therefore, the increase in aperture size also increases the resolution but decreases due to the influence of spherical aberration, given in Equation 3.2. However, when both criteria are combined and mathematically solved, an optimum objective aperture diameter can be calculated, and the maximum resolution is written in Equation 3.4. [12, 15]

$$\Delta r_{min} \approx \lambda^{3/4} \cdot C_s^{1/4} \tag{3.3}$$

$$\Delta r_d = \frac{0.61 \cdot \lambda}{\beta} \tag{3.4}$$

**Specimen resolution** Generally, the specimen is going to reduce the resolution of the image via chromatic aberration, since many electrons lose energy when they pass through the specimen. Only when very thin regions are examined, the energy loss of the electrons is minimized. [12]

### 3.3.2 Working principle of the scanning transmission electron microscopy

To understand the principle of a STEM, it is best to elucidate the different illumination mode from TEM. In TEM mode, the objective is to achieve a perfectly circular and parallel beam hitting the sample surface. Conversely, in STEM mode, the aim is to produce a focused, convergent beam. This is illustrated in Figure 3.3. [18]

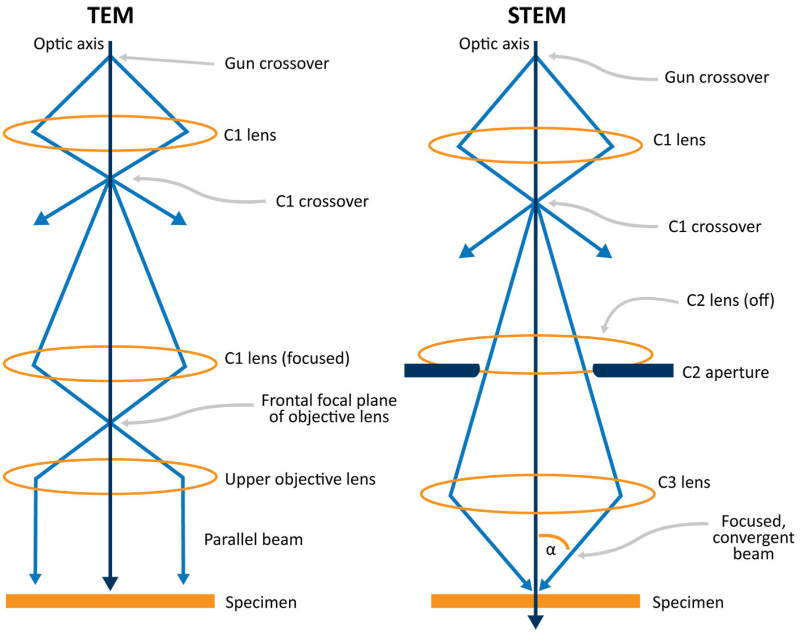

Figure 3.3: Different illumination techniques of a TEM compared with a STEM. [18]

The imaging technique of the STEM is able to visualize differences in the microstructures up to the nanometer scale while simultaneously collecting spectroscopic data of each point. The material under analysis must be electron-transparent, enabling electrons to pass through the sample with minimal scattering. Then the data is often collected via high-angle annular dark field (HAADF), bright field (BF) or dark field (DF) detectors.

### 3.3.3 *In situ* transmission electron microscopy

*In situ* experiments can be helpful to study the influence of heat, strain or accelerated particles upon the microstructure. When heat is applied, this will cause phase transformation and finally recrystallization of the microstructure. Via the use of *in situ* experiments, it can be understood at which temperature (or strain) changes in the microstructure will evolve and thus removing doubts from *ex situ* experiments. However, assumptions and conclusions drawn from such an experimental setup needs to be carefully done, since one requirement for the use of TEM experiments is a electron-transparent region. Therefore, the sample will be a thin foil, and, surface diffusion is much more rapid compared with bulk diffusion. Furthermore, it needs to be kept in mind that such experiments are performed under different conditions that are likely not the same in-service conditions. [16]

During *in situ* experiments, it is sensible to recall a well-known quote by Werner Heisenberg: [17]

> *"Wir können nicht beobachten, ohne das zu beobachtende Phänomen zu stören, und die Quanteneffekte, die sich am Beobachtungsmittel auswirken, führen von selbst zu einer Unbestimmtheit in dem zu beobachtenden Phänomen."*

The meaning of this quote is to comprehend that the observations made through any device are likely to differ from reality, where the act of observation itself has a strong influence on the phenomena. While this quote was originally written for quantum mechanics, it is also true for investigations made through any device, for example, an electron microscope. It is reported that the electron beam may rise the temperature of the sample, whilst the electrons emitted from the source to create this beam are bombarding the sample surface, leading to irradiation damage. With the increasing complexity of the experiments, the more careful they have to be carried out. Even though experiments within the TEM take place under vacuum, presence of gas molecules can never be neglected, as they may deposit on the surface of the specimen (such as carbon contamination). Then, these molecules will interact with the specimen and the electron beam might act as an catalyst for reaction, which normally do not happen. For example, carbon results in the contamination on the sample surface, whilst hydrocarbon are polymerised by the electron beam and even gas atoms can be injected into the specimen when environmental chambers are used. [19]

## 3.4 Reference

[1] Gloria Graf, Petra Spoerk-Erdely, Peter Staron, Andreas Stark, Francisca Mendez Martin, Helmut Clemens, and Thomas Klein. Quench rate sensitivity of age-hardenable Al-Zn-Mg-Cu alloys with respect to the Zn/Mg ratio: An in situ SAXS and HEXRD study. *Acta Materialia*, 227:117727, 2022.

[2] Joseph D Menczel, Lawrence Judovits, R Bruce Prime, Harvey E Bair, Mike Reading, and Steven Swier. Differential scanning calorimetry (DSC). *Thermal Analysis of Polymers: Fundamentals and Applications*, pages 7–239, 2009.

[3] David W Hahn and M Necati Özisik. *Heat Conduction*. John Wiley & Sons, 2012.

[4] S Jegadheeswaran and Sanjay D Pohekar. Performance enhancement in latent heat thermal storage system: a review. *Renewable and Sustainable Energy Reviews*, 13(9):2225–2244, 2009.

[5] Christoph Rathgeber, Laia Miró, Luisa F Cabeza, and Stefan Hiebler. Measurement of enthalpy curves of phase change materials via DSC and T-History: When are both methods needed to estimate the behaviour of the bulk material in applications? *Thermochimica Acta*, 596:79–88, 2014.

[6] Dan Dragulin and M Ruther. Specific heat capacity of aluminium and aluminium alloys. *Heat Treat*, 3:81–85, 2018.

[7] Peggy Cebe, Benjamin P Partlow, David L Kaplan, Andreas Wurm, Evgeny Zhuravlev, and Christoph Schick. Using flash DSC for determining the liquid state heat capacity of silk fibroin. *Thermochimica Acta*, 615:8–14, 2015.

[8] Louis A Turner. Zeroth law of Thermodynamics. *American Journal of Physics*, 29(2):71–76, 1961.

[9] Mike Reading and Duncan QM Craig. Principles of differential scanning calorimetry. *Thermal Analysis of Pharmaceuticals*, 1:1–22, 2006.

[10] Nicolas Chobaut. Measurements and modelling of residual stresses during quenching of thick heat treatable aluminium components in relation to their precipitation state. Technical report, EPFL, 2015.

[11] Kurt Binder. Theory of first-order phase transitions. *Reports on Progress in Physics*, 50(7):783, 1987.

[12] Jeffrey William Edington and JW Edington. *The operation and calibration of the electron microscope.* Springer, 1974.

[13] Max Haider, Harald Rose, Stephan Uhlemann, Eugen Schwan, Bernd Kabius, and Knut Urban. A spherical-aberration-corrected 200 kv transmission electron microscope. *Ultramicroscopy*, 75(1):53–60, 1998.

[14] Hidetaka Sawada, Takeshi Tomita, Mikio Naruse, Toshikazu Honda, Paul Hambridge, Peter Hartel, Maximilian Haider, Crispin Hetherington, Ron Doole, Angus Kirkland, et al. Experimental evaluation of a spherical aberration-corrected TEM and STEM. *Microscopy*, 54(2):119–121, 2005.

[15] Sisi Zhou and Liang Jiang. Modern description of Rayleigh's criterion. *Physical Review A*, 99(1):013808, 2019.

[16] C Barry Carter and David B Williams. *Transmission electron microscopy: Diffraction, imaging, and spectrometry.* Springer, 2016.

[17] Christoph Johannes Marty. *Vom Beobachten des Beobachters der Beobachter.* PhD thesis, TU Dortmund, 2015.

[18] Nanoscience.com. Scanning Transmission Electron Microscopy. Available at: https://www.nanoscience.com/techniques/scanning-transmission-electron-microscopy/. Accessed: 25.04.2024.

[19] EP Butler. In situ experiments in the transmission electron microscope. *Reports on Progress in Physics*, 42(5):833, 1979.

# Chapter 4

# Radiation-resistant aluminium alloy for space missions in the extreme environment of the solar system[*]

## Author´s Contribution

*Patrick D. Willenshofer* - Conceptualization, Methodology, Investigation, Visualization, Writing the original draft.

*Matheus A. Tunes* - Investigation, Conceptualization, Methodology, Writing - Review and Editing.

*Ho T. Vo* - Supervision, Investigation - Review and Editing.

*Lukas Stemper* - Supervision, Investigation - Review and Editing.

*Oliver Renk* - Supervision, Investigation - Review and Editing.

*Graeme Greaves* - Supervision, Investigation - Review and Editing.

*Peter J. Uggowitzer* - Supervision, Investigation, Methodology, Writing - Review and Editing.

---

[*] Status: Chapter 4 is a paper under revision for publication in the Journal Nature Communications, written by Patrick D. Willenshofer, Matheus A. Tunes, Ho T. Vo, Lukas Stemper, Oliver Renk, Graeme Greaves, Peter J. Uggowitzer, and Stefan Pogatscher

*Stefan Pogatscher* - Project Administration, Supervision, Investigation, Writing - Review and Editing.

## Acknowledgments

The research herein reported has been supported by both the European Research Council excellent science grant "TRANSDESIGN" through the Horizon 2020 program under contract 757961 and the Austrian Research Promotion Agency (FFG) in the project 3DnanoAnalytics (FFG-No 858040). The Los Alamos National Laboratory, an affirmative action equal opportunity employer, is managed by Triad National Security, LLC for the U.S. Department of Energy's NNSA, under contract 89233218CNA000001 and provided research support to both MAT and HVT via Laboratory Directed Research and Development program under project numbers 20200689PRD2 and 20220790PRD2, respectively. Research funding for the construction of the MIAMI facility has been provided by the United Kindgom's Engineering and Physical Sciences Research Council (EPRSC) via grant EP/M028283/1.

## Abstract

Future human-based exploration of our solar system requires the invention of materials that can resist harsh environments. Age-hardenable aluminium alloys would be attractive candidates for structural components in long-distance spacecrafts, but their radiation resistance to solar energetic particles is insufficient. Common hardening phases dissolve and displacement damage occurs in the alloy matrix, which strongly degrades properties. Here we present an alloy where hardening is achieved by T-phase, featuring a giant unit cell and highly-negative enthalpy of formation. The phase shows record radiation survivability and can stabilize an ultrafine-grained structure upon temperature and radiation in the alloy, therby successfully preventing displacement damage to occur. Such concept can be considered ideal for the next-generation space materials and the design of radiation resistant alloy.

## 4.1 Main Part

Humans are constantly striving to explore and unveil the unknown. This desire has set our species in a path in the ladder of science, and through excellence and knowledge, we are now progressively perceiving our position in the vast cosmic arena of the Universe. The exploration of the outer space is a colossal challenge that involves the multidisciplinary application of a wide plethora of modern technologies and sciences.

The adventure of humans in space is mainly permitted through the knowledge acquired by an ancient science: the metallurgy. The role of this science in the human-based exploration of space consists in the design and evaluation of the applicability of new materials for spacecrafts, satellites and space probes within the harsh environment of the space [1, 2, 3]. The knowledge accumulated over 70 years on multinational space programs allowed the elaboration of a current list of materials' requirements for application in extraterrestrial environments, considering the multiple degradation mechanisms that may operate synergistically while under in-service in space [2, 3]: (i) high strength-to-weight ratio [4, 5, 6, 7], (ii) excellent thermal performance in a broader temperature range whilst in vacuum [8, 9, 10, 6, 7, 11, 12], (iii) high corrosion resistance to active monoatomic species (*e.g.* O) and to ionizing plasma [13, 14, 15, 16], (iv) easy manufacturability and repairability [17, 18], (v) costs [19, 20], and (vi) high radiation tolerance [1, 2, 21, 3]. As a limiting factor, the first requirement calls for materials that are inherently lightweight as this is intended to minimize payload, fuel demands and low production costs. In terms of the interaction between both highly-energetic particles and electromagnetic radiation with matter, our solar system can be considered an extreme environment for materials and the last requirement on high radiation tolerance is predominant considering long-duration and long-distance space missions with possible human settlement in extraterrestrial environments [2].

In this context, the sources of radiation for both humans and materials within the solar system can be categorized as endogenous or exogenous. Endogenous radiation comprise the class that is generated within the interiors of a spacecraft, as for example, by a small modular nuclear reactor. Exogenous source of radiation constitute of trapped radiation, cosmic rays, solar wind and flares and coronal mass ejections [22, 23]. These are critical for both humans and materials within the solar system. This radiation is mostly generated by the Sun and its relationship with the solar cycles and its surrounding solar system is known as space weather [24]. For low-orbit missions, trapped radiation within the Earth's Van-Allen belts is problematic. These belts are magnetic fields that protects the Earth from Sun's radiation via trapping, thus also containing a significant flux of highly energetic particles that can cause radiation damage in materials. For space-missions beyond the Van-Allen belts and under space weather normal conditions, the total flux of solar energetic particles can reach $10^{12}$ ions$\cdot$cm$^{-2}\cdot$s$^{-1}$ causing moderate damage to in-service materials [24, 22, 25]. Under abnormal conditions, solar flares and coronal mass ejections can significantly increase the radiation flux in a short-period of time that may lead to severe radiation effects in spacecraft materials [3].

Both endogenous and exogenous radiation sources within the context of space missions pose new challenges for materials science with respect to the selection of structural materials for application in the extreme environment of the solar system [2, 3]. Considering the strictly high strength-to-weight ratio as a major criteria for materials selection, Al is a preferential metal candidate and, in fact, Al-based alloys are already used in several spacecraft and satellites structures with a dual purpose: to shield and to resist energetic particle and electromagnetic radiations [3]. Al-based alloys are inherently lightweight due to their attainable low density and they can also be designed to achieve high levels of strength via precipitation hardening [26, 27, 28]. The retention of such a high strength will be dependent upon the survivability of hardening precipitates under irradiation: if the radiation dissolves the precipitates, the alloy will lose the initially designed high strength [29, 3]. "Ideal" materials for radiation environments are those that can preserve its initial properties upon impact of highly energetic particles with their crystalline lattices. Energetic particle irradiation can cause degradation via introduction of point defects into crystalline structures by displacing the lattice atoms from their equilibrium positions. On this context, displacements-per-atom (or dpa) is an average measure of how much lattice atoms are displaced from their lattice upon impinging atomic collisions.

Irradiation experiments in Al-based alloys have so far shown both a tendency for saturation of displacement damage in a form of dislocation loops (causing irradiation-induced embrittlement) and hardening phases dissolution (leading to alloy softening) at doses as low as 0.1 dpa considering commercial Al-based alloys with micrometer-sized grains [29, 3]. Therefore, two major aspects are desirable for the candidateship of novel Al-based alloys as future space materials: a hardening phase capable of resisting high doses of irradiation, but in addition offer a matrix capable of resisting the development of displacement damage in the form of dislocation loops and voids. Using the crossover principle, we demonstrate in this work the solution to the problem via the synthesis of a stable ultra-fine grained (UFG) microstructure of a novel aluminium crossover alloy. Recently invented via the metallurgical merge between two distinct classes of aluminium alloys, the AlMg and AlZnMg(Cu) alloys (AA5xxx/AA7xxx), the aluminium crossover alloys were found to be hardenable via precipitation of a highly-concentrated ternary intermetallic superstructure: the T-phase with chemical formula $Mg_{32}(Zn,Al)_{49}$ [30]. For simplicity, the herein investigated crossover alloy Al-5.34Mg-1.56Zn-0.26Cu-0.04Ag in at.% - is referred to AlMgZnCuAg throughout the article. Usually, nanocrystalline or UFG Al-based alloys tend to recrystallize at low temperatures easily [31]. We prove that suitable heat treatment procedures enable the UFG structure of our Al-based crossover alloy to both precipitate the T-phase and preserve its matrix grain size within the nanoscale upon heavy irradiation. Heavy ion irradiations with *in situ* Transmission Electron Microscopy (TEM) were performed at the MIAMI facilities using a 300 keV $Ar^+$ ion beam line [32]. This methodology allowed a real-time assessment and direct microstructural monitoring of the radiation effects.

### 4.1.1 Results

The procedure for obtaining the UFG AlMgZnCuAg crossover alloy is shown in Figure 4.1a. After casting and High-Pressure Torsion (HPT), a characteristic UFG microstructure was observed as shown in the Bright-Field TEM micrograph (BFTEM)

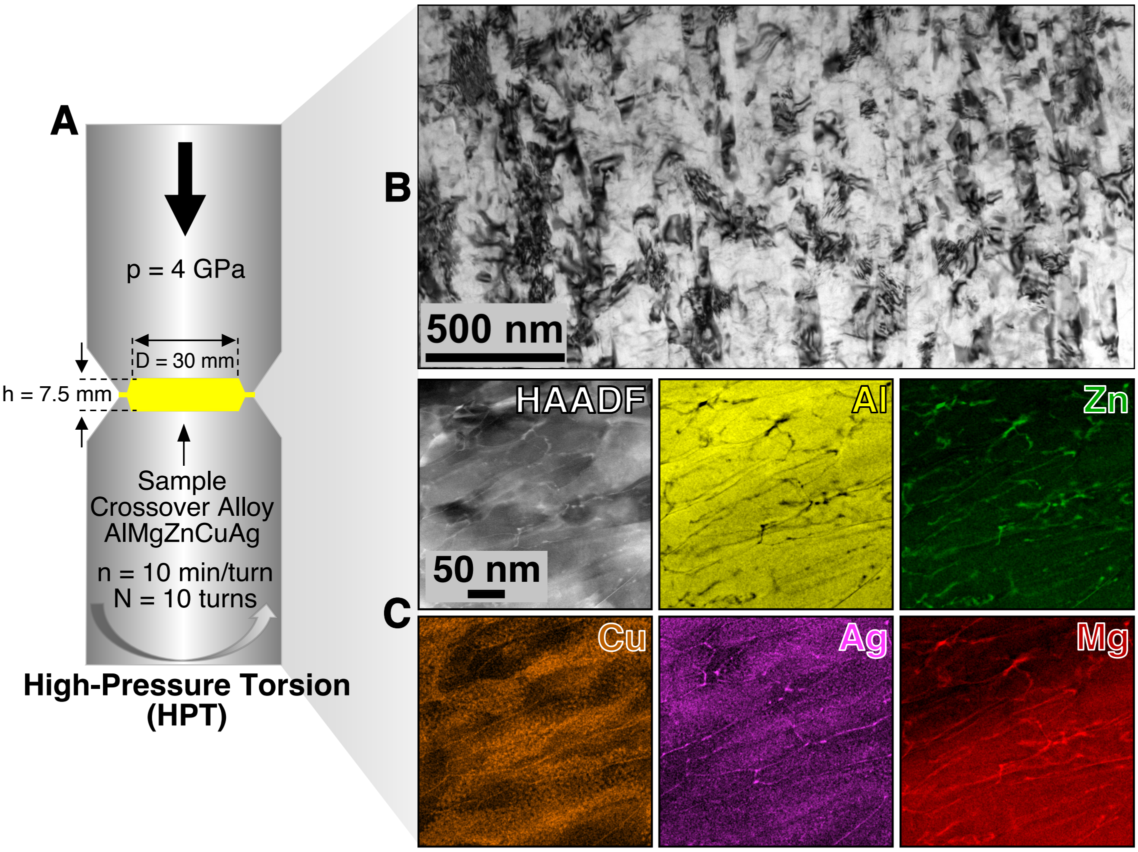

Figure 4.1: Synthesis of the UFG aluminium crossover alloy — a) To achieve an UFG microstructure from the bulk AlMgZnCuAg crossover alloy, the technique of HPT was used. B) After processing, BFTEM revealed a UFG microstructure. Local nanochemistry analysis revealed segregation of all alloying elements to the grain boundaries, but no T-phase precipitates in the as-processed condition as shown in the STEM-EDX mapping in c).

in Figure 4.1b. Scanning Transmission Electron Microscopy (STEM) with coupled Energy-Dispersive X-ray spectroscopy (EDX) assessment of the alloy in the as-processed condition is also presented in Figure 4.1c. After HPT, no T-phase precipitation was observed, although the goal to achieve grains confined within the nanometer-scale was successful. Mg, Zn, Cu and Ag segregation along the grain boundaries was noted in this condition.

The absence of T-phase precipitates suggested the need for heat-treatment enabling its formation. The challenge here is to overcome the well-known low-temperature recrystallization of UFG Al-based alloys [31]. For the UFG AlMgZnCuAg crossover alloy investigated in this work, we found that a controlled heat-treatment using a ramp rate of 10 K$\cdot$min$^{-1}$ up to 506 K was sufficient to promote nucleation and growth of T-phase precipitates while recrystallization was not observed. The set of STEM-EDX mappings in Figure 4.2a shows the microstructure of our alloy after this heat-treatment step. T-phase precipitates are observed not only at transgranular positions, but also along intragranular positions. STEM-EDX measurements revealed no difference between precipitates at transgranular or intragranular sites. In addition, according to our thermodynamic calculations (see Figure 4.4), only T-phase precipitates are expected. These results also validate another study on a bulk aluminium crossover alloy with similar chemical composition [44]. By pinning the grain boundaries at the nanoscale and thus stabilizing the initial grain size, the T-phase was observed to prevent the phenomenon of recrystallization. Therefore, the T-phase precipitation potential of the UFG AlMgZnCuAg crossover alloy was herein demonstrated. It is worth noting that various heat-treatment conditions have been tested within this project and it was observed that recrystallization happened only at much faster heating rates for the UFG AlMgZnCuAg crossover alloy shown in the extended data. During these experiments, only the T-phase precipitates were detected. Moreover, thermodynamic calculations also predicted only the precipitation of T-phase particles in the matrix (see Figure 4.4).

Irradiation experiments were performed up to extreme doses of 100 dpa, which represents the average value over the whole specimen thickness. The dose steps shown in Fig. SM2 correspond to the set of BFTEM micrographs in Figure 4.2b) acquired during the *in situ* TEM irradiations of the alloy after heat treatment. Two important conclusions can be drawn from the results of the irradiation tests. Firstly, neither formation nor accumulation of irradiation-induced dislocation loops is noted even though the alloy was real-time monitored using a multi-beam condition in BFTEM. This is opposed to our previous observations [3] in a coarse grained Al-based crossover alloy where numerous dislocation loops formed and accumulated and resulted in irradiation-induced embrittlement typically observed in metals and alloys [3]. Secondly, no irradiation-induced grain-growth was noted. As recently reviewed in literature [33], this result is of a particular interest as many metallic nanocrystalline alloys subjected to ion irradiation severely suffer from this effect already at lower doses than herein tested. Voids were observed to form only at doses higher than 75

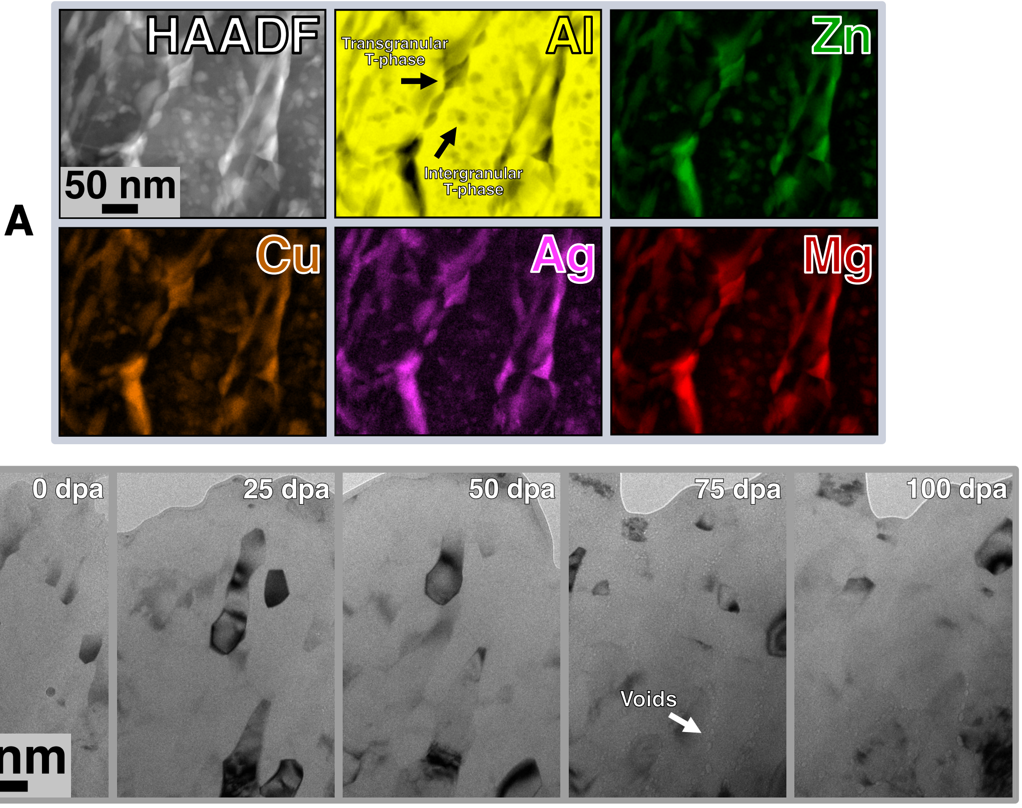

Figure 4.2: Alloy's stability under irradiation — Nucleation of T-phase precipitates in the UFG AlMgZnCuAg crossover alloy was observed after heat-treatment using a ramp of 10 K·min$^{-1}$ up to 506 K a). The microstructural evolution of the UFG AlMgZnCuAg crossover alloy as monitored *in situ* within the TEM is shown in the set of underfocused BFTEM micrographs in b) from 0 to 100 dpa. The alloy's microstructure neither exhibit formation of dislocation loops nor grain growth at a maximum dose of 100 dpa. Voids are only observed to form at around 75 dpa.

dpa: this was the only deleterious effect of radiation observed for this alloy.

Both the absence of dislocation loops and grain growth already suggest that the tested material exhibits a distinct and outstanding level of radiation tolerance. However, final proof for the survivability of the T-phase precipitates under irradiation needs to be fully disclosed. It is worth emphasizing that the dissolution of hardening precipitates under irradiation occurs via ballistic mixing (BM) [29, 3]. The ballistic impact of a highly energetic particle within the crystalline lattice of an alloy generates a cascade of point defects, raising local temperature for an ultra-short period of time which results in a complete local chemical reorganization of atoms in a crystal, and also the dissolution of hardening phase particles. Only a limited number of studies exist on BM-assisted dissolution of age-hardening precipitates in Al-based alloys. The commercial Al-based alloy grade AA6061-T6 was shown to be susceptible to BM-assisted dissolution of its hardening phase – the $Mg_2Si$ known as $\beta$-phase – which did not survive doses up to 0.2 dpa when exposed to proton beams with energies between 600-800 MeV [29]. Lohmann *et al.* results were both timely and independently validated by Singh *et al.* [34]. It is worth noting that the AA6061-T6 is commercially significant and widely used as structural material for aerospace applications. Severe radiation effects have been also reported to other commercial Al-based alloys [35, 36, 38, 37, 39, 40, 41], which motivated scientific research to develop novel Al-based age-hardenable alloys capable of resisting the deleterious effect of radiation exposure. Opposed to Lohmann *et al.* and Singh *et al.* [29, 34], Flament *et al.* irradiated the AA6061-T6 with heavy-ions with high energies (4 MeV Au and 2 MeV W ions) [42]. These authors report partial dissolution of $Mg_2Si$ precipitates at around 95 dpa and complete dissolution after 165 dpa, but have not investigated the effects of irradiation on the hardening phases at lower doses ($\leq 1$ dpa). Therefore, whether the $Mg_2Si$ dissolve at lower doses and re-precipitates at higher doses is pending further research.

Preliminary research demonstrated that the T-phase has a superior Radiation Survivability Level (RSL) of 1 dpa when compared with other hardening phases in conventional Al-based alloys [3]. T-phase precipitates in a Al-5.30Mg-1.42Zn (at.%)

micrometre-grain sized crossover alloy survived up to 1 dpa using heavy ions with 100 keV $Pb^+$. A possible higher RSL for T-phase precipitates in the UFG Al-based crossover alloy is a hypothesis to be tested in this work. As these precipitates can be hardly seen using the multi-beam and lower-magnification BFTEM condition due to their small sizes, STEM-EDX mapping as shown in Figure 4.6a) were acquired after irradiation around 6 dpa. These images unequivocally prove that T-phase survived at this irradiation dose. This has been additionally proven by subsequent post-irradiation assessment using Selected-Area Electron Diffraction (SAED) pattern, High-Resolution TEM (HRTEM) with derived FFT, respectively in Figure 4.6b-d). For reference, the observed superlattice reflections (more visible in the FFT) agree well with previous identification of T-phase precipitates [43, 44, 45, 30]. Given the observations made so far, the results shown in this research serve as a guidance to elaborate a new alloy design strategy for novel UFG Al-based alloys to be used in extreme environments. This is described in the schematics presented in Figure 4.6e): After processing via HPT the alloys' potential is not yet fully exploited. A suitable heat treatment must be applied in order to precipitate T-phase both along the grain boundaries and at transgranular positions. Using this alloy design strategy, the mechanisms of high radiation tolerance can be harnessed. The presence of homogeneously distributed nanoprecipitates in higher volumetric fraction compared with commercial Al-based alloys [3] as well as the fact that the alloy confines its grain size within the nanoscale suggest a significant ability for absorption of radiation-induced point defects without material degradation, thus preventing the manifestation of extended radiation effects (except for voids at very high doses of 75 dpa).

Post-irradiation investigations beyond 6 dpa were performed to assess the RSL of T-phase precipitates within the UFG AlMgZnCuAg crossover alloy. Figure 4.4a) and Figure 4.4b) show the STEM-EDX maps taken at low and high magnification after 24 and 100 dpa, respectively. We discovered that the RSL threshold of T-phase precipitates within the UFG AlMgZnCuAg crossover alloy is 24 dpa. T-phase was observed to be fully dissolved at 100 dpa. To the best of our knowledge, a RSL of 24 dpa is a new record scored among all known hardening precipitates tested under

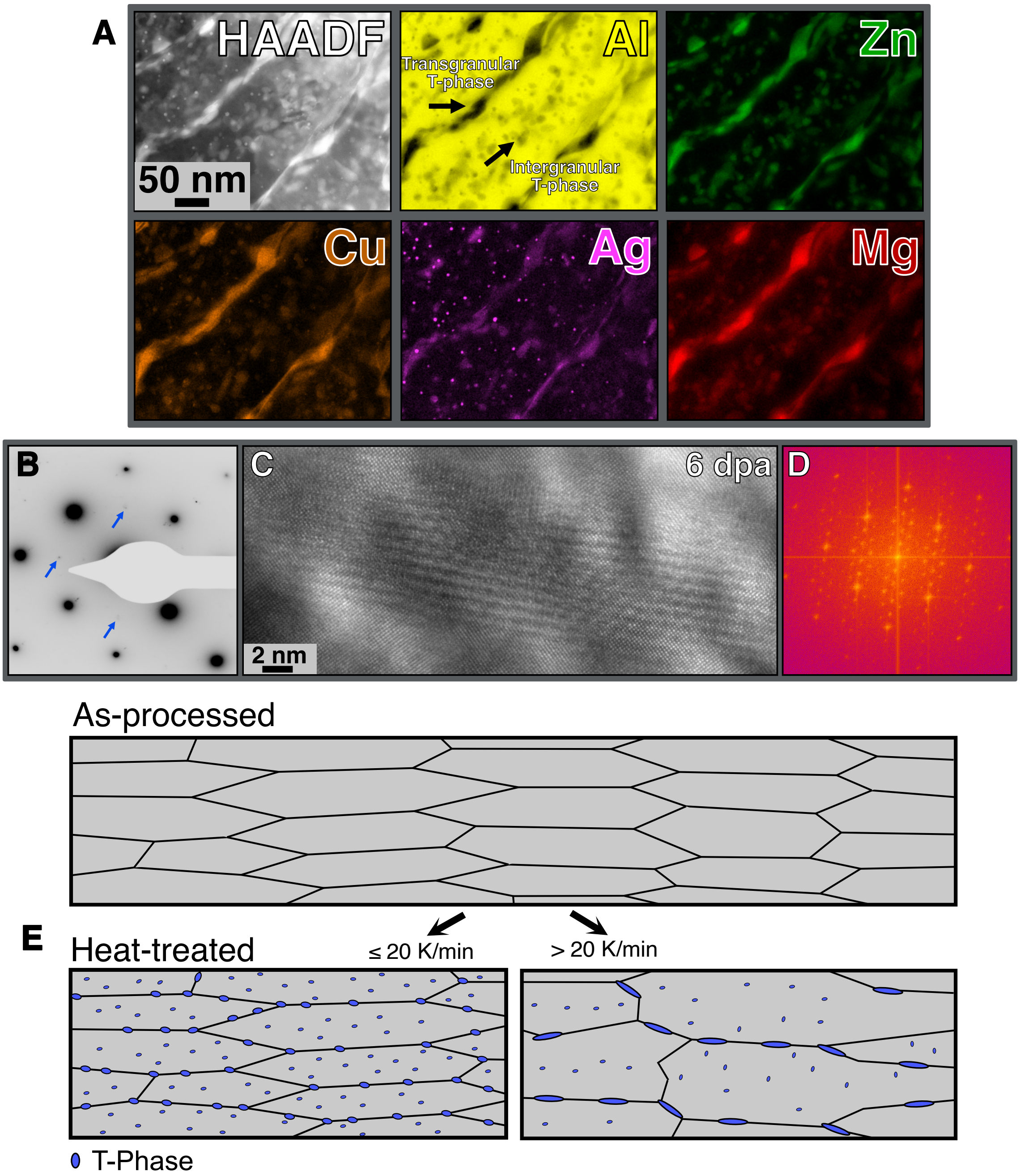

Figure 4.3: Alloy's stability under irradiation (post-irradiation examination) — Post-irradiation methodologies using conventional and analytical electron-microscopy were used to investigate the origins of the alloy's stability under irradiation. A) STEM-EDX mapping and b-d) SAED, HRTEM and FFT, respectively, show that T-phase precipitates are stable and did not dissolve at the exemplary dose of 6 dpa, which is six [3] and thirty [29] times higher dose than previous reports on irradiation-assisted dissolution of hardening phases in bulk Al-based alloys. The schematics in e) exhibit microstructural differences in the UFG alloy before and after a heat treatment, establishing a new alloy design strategy to achieve high radiation tolerance. T-phase precipitates are prone to nucleate, grow and stabilize the structure.

irradiation so far. This is 24 times higher compared to our previous record of 1 dpa in the coarse grained Al-based crossover alloy [3] and 120 times higher than $Mg_2Si$ in conventional AA6061-T6 as tested by Lohmann *et al.* [29].

Thermodynamics were used to assess the stability of crystalline phases under irradiation. Figure 4.4c) reveals another interesting and important feature of Al-based crossover alloys: the T-phase's enthalpy of formation ($H_f$) shows the highest negative value known so far among the hardening precipitates within the whole spectrum of commercial aluminium alloys, *i.e.* ($Mg_2Zn$) $\eta$-, ($Al_2Cu$) $\theta$-, ($Mg_2Si$) $\beta$-phase. The crystal structures of all these hardening phases as well as the T-phase are shown in Figure 4.4e). T-phase exhibits both distinct $H_f$ and crystal structure when compared to other precipitates in Al-based alloys. In fact, Bergman and Pauling *et al.* discovered in the late 1950s [46], that T-phase has a characteristic unit cell structure comprising 162 atoms per cube. BM-assisted dissolution of precipitates requires that the incoming and highly-energetic atoms promote dissociation of constituents via atomic displacements in an uncontrolled manner that inevitably leads to destruction of the crystalline state. However, high negative values for $H_f$ indicate that the dissolution of the entire T-phase crystal structure under radiation is significantly impeded. This is opposed to the case of ceramics materials with mixed covalent-ionic bonding: amorphization (loss-of-crystallinity) occurs via destruction of atomic bonding promoted by displacing collisions in an irreversible manner [47], although they can also be characterized with high negative values for enthalpy of formation. Conversely, T-phase shows that both atomic displacements and stoichiometry changes can take place without major changes in its bulk crystal structure (Figure 4.4d)) [48]. Evidence herein presented may indicate that the origins of high radiation tolerance of T-phase precipitates resort – and can be tailored – to its unique thermodynamic state as an essential factor of stability.

It has been previously demonstrated that the T-phase can dissolve both Cu and Ag in its crystal structure contributing both its thermodynamic stability and to an enhancement of mechanical properties [45, 44]. Upon the irradiation experiments, Ag nanoprecipitates do form at 6 dpa (see Figure 4.6a)), whilst Mg, Zn and Cu are not affected. It is worth to mention that the vast majority of Ag is found within the T-phase, thus the nucleation of Ag nanoprecipitates did not harm the stability of the T-phase under irradiation. Additions of Ag into the crossover alloy were found to be of importance for the thermodynamic stability of the T-phase [45]. Therefore, the addition of Ag is required to support nucleation of the T-phase and its irradiation resistance.

During the irradiation experiments, the alloy was monitored in situ within a TEM. Neither grain growth nor the development of microstructural defects like dislocation loops or stacking fault tetrahedral were observed up to 100 dpa. STEM-EDX assessment also revealed that the T-phase is stable up to 24 dpa. Moreover, only at high doses such as 75 dpa, voids were detected in the matrix.

The design of new materials for stellar-radiation environments currently present several challenges mainly with respect to radiation resistance. The criteria of high strength-to-weight ratio is mandatory for space programs, limiting the choices to metals exhibiting lower densities. In this research, we introduced a new alloy design methodology that lead to the synthesis of a new UFG AlMgZnCuAg crossover alloy with high radiation tolerance. This alloy features unique T-phase precipitates with an estimated RSL of 24 dpa, a new irradiation dose record. In addition, due to the UFG microstructure, the alloy has not exhibit any detectable dislocation loop as a result of irradiation, and voids were only observed at a dose of 75 dpa. We have shown that by tailoring thermodynamics at the atomic level, new materials can be designed to sustain radiation levels that even extrapolates the exogenous conditions found in the solar system. Still further research is required to unveil the full mechanisms by which T-phase precipitates survive to irradiation in such aggressive conditions.

## 4.2 Materials and Methods

### 4.2.1 Synthesis of the alloy and post-synthesis processing

A novel UFG Al-based crossover alloy within the quinary system of Al–Mg–Zn–Cu–Ag was synthesized using a vacuum induction melting furnace. Casting was performed

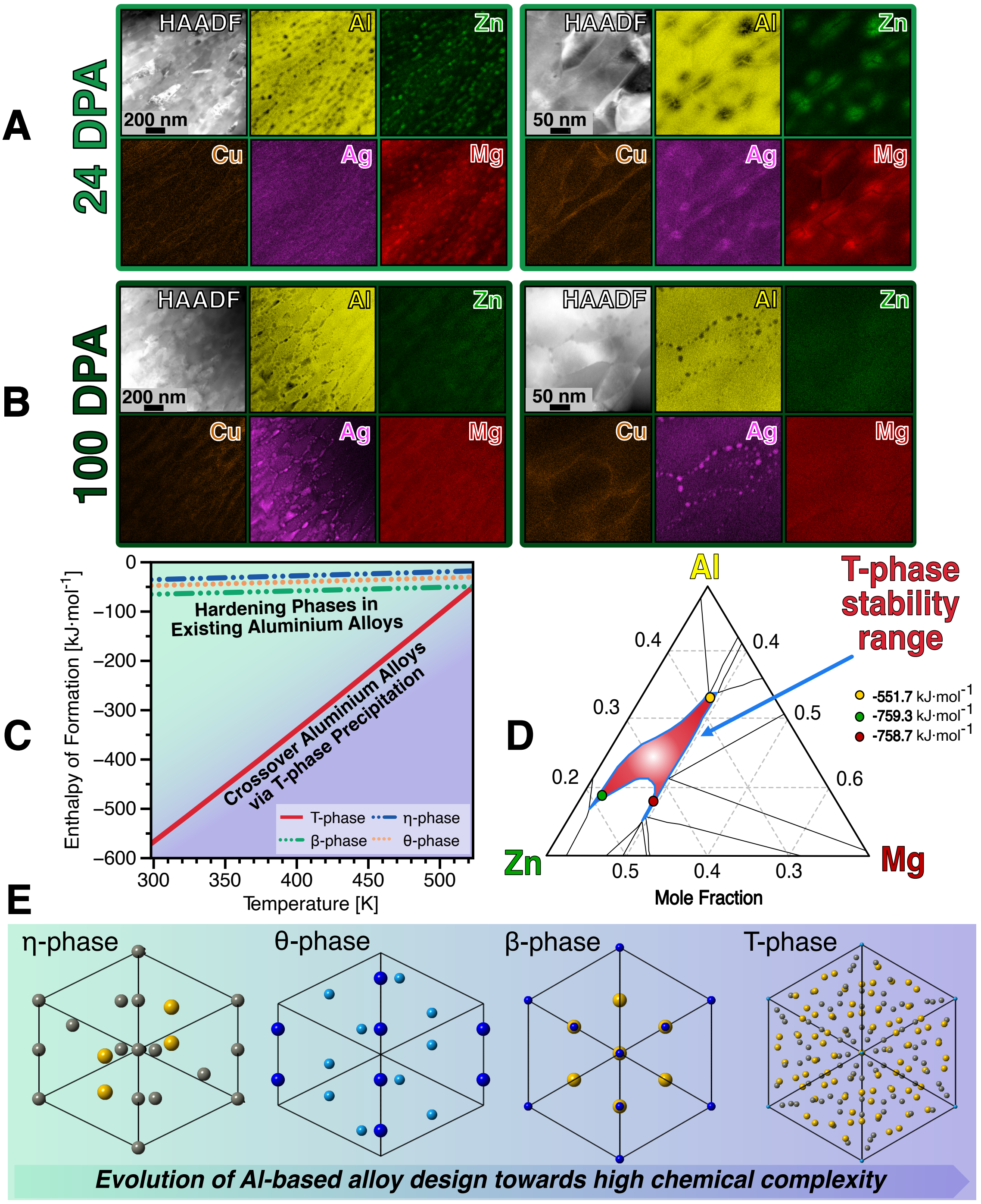

Figure 4.4: Radiation Survivability Level of T-phase precipitates and thermodynamic origins of their high radiation tolerance — A survey using STEM-EDX mapping in the post-irradiated specimens shows that T-phase precipitates surviving up to a dose of 24 dpa, as denoted in a). After 24 dpa, the precipitates began to (progressively) dissolve and at the dose of 100 dpa, b), no T-phase precipitates were detected in the UFG AlMgZnCuAg crossover alloy. Radiation-induced precipitation of pure Ag nanoprecipitates is noted only at doses around 100 dpa. Thermodynamic calculations in plot c) show that the entalphy of formation for T-phase precipitates is significantly lower compared with hardening precipitates within the existing Al-based alloys. The T-phase is found to be stable over a wide range of chemical ratios as shown in the ternary equilibrium phase diagram in d) calculated at both 298 K and 1 bar. e) The crystal structures of the ($Al_2Cu$) $\theta$-phase, ($Mg_2Zn$) $\eta$-phase, ($Mg_2Si$) $\beta$-phase and ($Mg_{32}(Zn,Al)_{49}$) demonstrate that chemical complexity is a distinct characteristic of the T-phase precipitates tailoring the radiation resistance of the UFG AlMgZnCuAg crossover alloy.

in a Cu mould and the elemental composition was measured to be Al-5.34Mg-1.56Zn-0.26Cu-0.04Ag in at.% using Optical Emission Spectroscopy . After casting, the alloy slabs were homogenized at both 733 and 743 K followed by a machining step to obtain a disk with 6.5 mm thickness and 30 mm in diameter. The last step was necessary to fit the anvil for the HPT application. To obtain a UFG structure, HPT was used with 4 GPa of pressure, 10 turns comprising 10 min$\cdot$revolution$^{-1}$ for each turn. To investigate the microstructural stability and precipitation behavior of the UFG Al-based crossover alloy upon heating and irradiation, samples for Scanning and Transmission Electron Microscopy (STEM/TEM) were prepared from the outer radius of HPT disk to ensure a microstructure with uniform distribution of grain sizes. Different heat treatment strategies were applied and studied: as-processed via HPT and at 5, 10 and 20 K$\cdot$min$^{-1}$ up to 506 K.

### 4.2.2 Sample preparation for electron microscopy

Thin-foil for electron microscopy were prepared from the as-processed condition. Samples were ground to a thickness between 80-100 $\mu$m. Disks with 3 mm (diameter) were punched from the foil and subjected to twin Jet Electropolishing using a solution of 25% nitric acid and 75% methanol (in volume) at a temperature range from 243 to 248 K with an electric potential of 12 V until perforation. After electropolishing, specimens were washed in three sub-sequential pure methanol baths and left to dry in the air.

### 4.2.3 In situ TEM annealing and ion irradiation

*In situ* TEM annealing was carried out to investigate the microstructural response and stability of the UFG Al-based alloy in addition to evaluate its precipitation behavior. For these experiments, a Protochips FUSION MEMS chip-based holder in a Thermo Fisher Talos F200X S/TEM was used followed by a sample preparation procedure described in literature [29].

*In situ* TEM heavy ion irradiations were carried out in the MIAMI-2 facility at the University of Huddersfield [32]. The irradiation experiments were performed using a 300 keV $Ar^+$ ion beam. The flux was measured at the specimen position using a current metering rod and it was estimated to be $7.74\times10^{13}$ ions·cm$^{-2}$·s$^{-1}$ with an empirical error of 10%. Prior to irradiation, the as-processed samples were subjected to heat-treatment using a Gatan double-tilt heating holder model 652. The heat-treatment was performed at a ramp rate of 10 K·min$^{-1}$ up 506 K in order to allow the precipitation of the T-phase. During the irradiation experiments, samples were monitored using a Gatan Oneview 4k camera coupled in a Hitachi H9500 TEM operating at 300 keV. The Stopping and Range of Ions in Matter (SRIM) code [50] was used to convert fluence to an equivalent dose in displacement-per-atom (dpa) following a procedure suggested by Stoller et al. [51]. Under the ion irradiation conditions presented in this work, the maximum fluence achieved during the experiments was $2.3\times10^{17}$ ions·cm$^{-2}$, which corresponds to an equivalent dose average of 100 dpa. This ion irradiation set-up was found to be a convenient way to simulate the displacement cascades generated by the primary knock-on atoms (PKA) in Al when subjected to collisions with highly-energetic proton beams emitted by the Sun [3, 52], and without radioactive activation of the UFG Al-based crossover alloy.

### 4.2.4 Pre- and post-irradiation characterization methodology

Pre- and post-irradiation characterization was carried out using both a Thermo Fisher Scientific Talos F200X and a Thermo Fisher Titan 30-800 scanning transmission electron microscopes. For investigations high annular dark field (HAADF), bright-field (BF-TEM), high-resolution (HRTEM) and energy-dispersive X-ray spectroscopy (EDX) measurements were carried out.

### 4.2.5 Thermodynamic calculations

The enthalpy of formation ($H_f$) curves in Figure 4.4c,d) were calculated using the thermochemical software FactSage 8.0 and the FTlite database. Since the intermetallic T-phase has no strict stoichiometric value for Zn or Al, we determined the composition of the T-phase in our alloy at the desired artificial aging temperature at 506 K. We used the given composition to calculate the enthalpy of formation as a function of temperature within the range from 273 K to 523 K. Furthermore, the variation of enthalpy as a function of temperature of essential hardening phases in different Al-based alloys were drawn comparatively. Therefore, we selected $\theta$-phase ($Al_2Cu$), $\beta$-phase ($Mg_2Si$) and $\eta$-phase ($MgZn_2$) for 2xxx, 6xxx and 7xxx series alloys, respectively.

### 4.2.6 Appendix

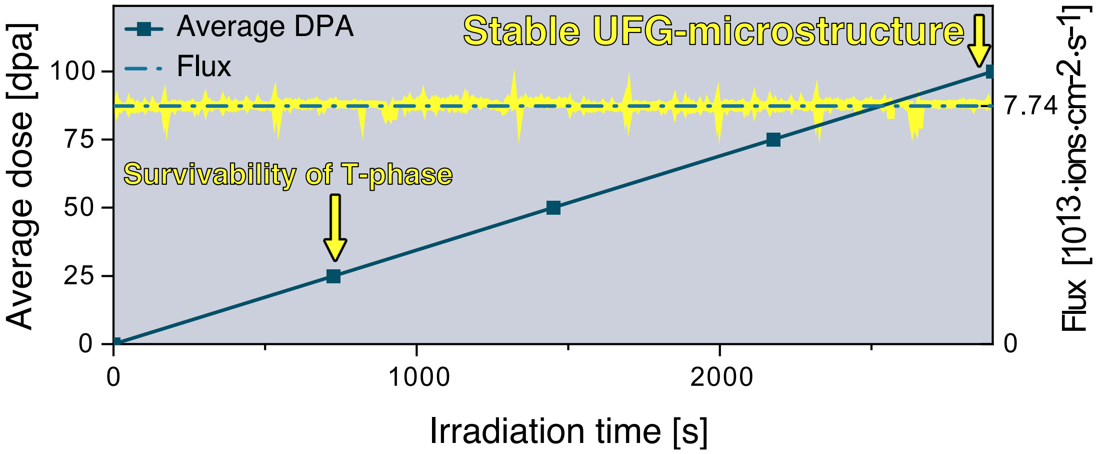

Figure 4.5: Irradiation experiments carried out on the UFG-crossover sample — The experiments were carried out up to 100 dpa. The Radiation Survivability Level of the T-phase was determined to be at 24 dpa. The experiments were carried out further up to 100 dpa. The UFG-microstructure was still intact after 100 dpa.

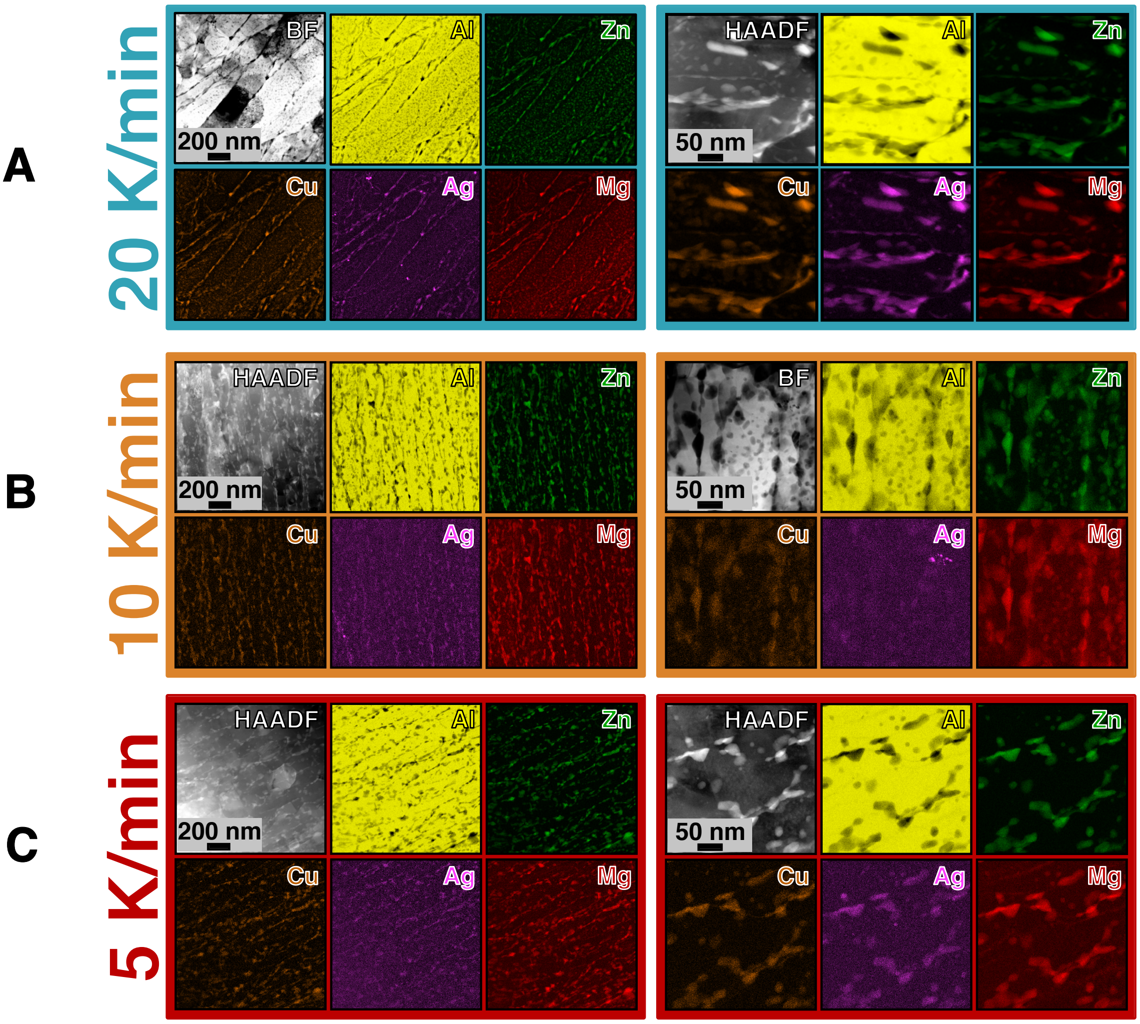

Figure 4.6: Different heating strategies to precipitate the T-phase — After HPT, no phase was detected. A proper heat-treatment was required to precipitate the T-phase and inhibit grain growth. a) 20 K/min b) 10 K/min and c) 5 K/min were tested. Above and below 10 K/min, the T-phase precipitation was not uniform. In a) and c), the nucleation sites mainly focused on the grain boundaries and the precipitates were observed to be coarse. Only when the sample was heated with 10 K/min in b), we were able to distribute fine precipitates at both inter- and transgranular sites.

## 4.3 Reference

[1] Judith C Yang and Kim K de Groh. Materials issues in the space environment. *MRS Bulletin*, 35(1):12–20, 2010.

[2] Tommaso Ghidini. Materials for space exploration and settlement. *Nature Materials*, 17(10):846–850, 2018.

[3] Matheus A Tunes, Lukas Stemper, Graeme Greaves, Peter J Uggowitzer, and Stefan Pogatscher. Prototypic Lightweight Alloy Design for Stellar-Radiation Environments. *Advanced Science*, 7(22):2002397, 2020.

[4] Neil Jacobstein, James Bellingham, and Guang-Zhong Yang. Robotics for space and marine sciences, 2017.

[5] Yang Gao and Steve Chien. Review on space robotics: Toward top-level science through space exploration. *Science Robotics*, 2(7):eaan5074, 2017.

[6] Manish Chhowalla and Deep Jariwala. Hyperbolic 3D architectures with 2D ceramics. *Science*, 363(6428):694–695, 2019.

[7] Qing-Fang Guan, Huai-Bin Yang, Zi-Meng Han, Li-Chuan Zhou, Yin-Bo Zhu, Zhang-Chi Ling, He-Bin Jiang, Peng-Fei Wang, Tao Ma, Heng-An Wu, et al. Lightweight, tough, and sustainable cellulose nanofiber-derived bulk structural materials with low thermal expansion coefficient. *Science Advances*, 6(18): eaaz1114, 2020.

[8] Joyce A Dever, Sharon K Rutledge, Mark M Hasegawa, and Charles K Reed. Evaluation of low earth orbit environmental effects on international space station thermal control materials. In *Protection of Space Materials from the Space Environment*, pages 181–195. Springer, 2001.

[9] Zhongping Yao, Qixing Xia, Pengfei Ju, Jiankang Wang, Peibo Su, Dongqi Li, and Zhaohua Jiang. Investigation of absorptance and emissivity of thermal control coatings on Mg–Li alloys and OES analysis during PEO process. *Scientific Reports*, 6(1):1–9, 2016.

[10] Harry A Atwater, Artur R Davoyan, Ognjen Ilic, Deep Jariwala, Michelle C Sherrott, Cora M Went, William S Whitney, and Joeson Wong. Materials challenges for the Starshot lightsail. *Nature Materials*, 17(10):861–867, 2018.

[11] Mingyang Li, Dongqing Liu, Haifeng Cheng, Liang Peng, and Mei Zu. Manipulating metals for adaptive thermal camouflage. *Science Advances*, 6(22): eaba3494, 2020.

[12] Yang Cheng, Xuanyang Li, Yixiu Qin, Yuting Fang, Guanglei Liu, Zengyao Wang, John Matz, Pei Dong, Jianfeng Shen, and Mingxin Ye. Hierarchically porous polyimide/$Ti_3C_2T_x$ film with stable electromagnetic interference shielding after resisting harsh conditions. *Science Advances*, 7(39):eabj1663, 2021.

[13] Bruce A Banks, Jane A Backus, Michael V Manno, Deborah L Waters, Kevin C Cameron, and Kim K De Groh. Prediction of atomic oxygen erosion yield for spacecraft polymers. *Journal of Spacecraft and Rockets*, 48(1):14–22, 2011.

[14] Aobo Guo, Claire C Ashmead, Kim K de Groh, and Edward A Sechkar. Effect of Solar Exposure on the Atomic Oxygen Erosion of Hubble Space Telescope Aluminized-Teflon Thermal Shields. In *Protection of Materials and Structures From the Space Environment*, pages 27–40. Springer, 2013.

[15] Kim K de Groh, Deborah L Waters, Jelila S Mohammed, Bruce A Perry, and Bruce A Banks. Analyses of Hubble Space Telescope Aluminized-Teflon Insulation Retrieved After 19 Years of Space Exposure. *Protection of Materials and Structures From the Space Environment*, pages 13–26, 2013.

[16] I Levchenko, S Xu, G Teel, D Mariotti, MLR Walker, and M Keidar. Recent progress and perspectives of space electric propulsion systems based on smart nanomaterials. *Nature Communications*, 9(1):1–19, 2018.

[17] David Cadogan, J Stein, and Mark Grahne. Inflatable composite habitat structures for lunar and mars exploration. *Acta Astronautica*, 44(7-12):399–406, 1999.

[18] Andrew Coffey, Alyssa Deardorff, Tyler Weihing, Bradford Robertson, and Dimitri N Mavris. Probabilistic Technology Selection for In Space Assembly, Manufacture, and Repair. In *2018 AIAA SPACE and Astronautics Forum and Exposition*, page 5240, 2018.

[19] John M Logsdon. International involvement in the US space station programme. *Space Policy*, 1(1):12–25, 1985.

[20] Peter M Banks. Future of US space programme. *Nature*, 327(6119):182, 1987.

[21] Tobias Vogl, Kabilan Sripathy, Ankur Sharma, Prithvi Reddy, James Sullivan, Joshua R Machacek, Linglong Zhang, Fouad Karouta, Ben C Buchler, Marcus W Doherty, et al. Radiation tolerance of two-dimensional material-based devices for space applications. *Nature Communications*, 10(1):1–10, 2019.

[22] N. A. Schwadron, F. Rahmanifard, J. Wilson, A. P. Jordan, H. E. Spence, C. J. Joyce, J. B. Blake, A. W. Case, W. de Wet, W. M. Farrell, J. C. Kasper, M. D. Looper, N. Lugaz, L. Mays, J. E. Mazur, J. Niehof, N. Petro, C. W. Smith, L. W. Townsend, R. Winslow, and C. Zeitlin. Update on the Worsening Particle Radiation Environment Observed by CRaTER and Implications for Future Human Deep-Space Exploration. *Space Weather*, 16(3):289–303, 2018. ISSN 15427390.

[23] Justin C Kasper, Stuart D Bale, John W Belcher, Matthieu Berthomier, Anthony W Case, Benjamin DG Chandran, DW Curtis, D Gallagher, SP Gary, L Golub, et al. Alfvénic velocity spikes and rotational flows in the near-Sun solar wind. *Nature*, 576(7786):228–231, 2019.

[24] Mark Moldwin. *An Introduction to Space Weather*, volume 1. Cambridge University Press Cambridge, 2008.

[25] Andrew Holmes-Siedle and Len Adams. *Handbook of Radiation Effects*. Oxford Univ. Press, Inc., New York, NY (United States), 1993.

[26] André Guinier. Structure of age-hardened aluminium-copper alloys. *Nature*, 142(3595):569–570, 1938.

[27] GD Preston. Structure of age-hardened aluminium-copper alloys. *Nature*, 142 (3595):570, 1938.

[28] Phillip Dumitraschkewitz, Peter J Uggowitzer, Stephan SA Gerstl, Jörg F Löffler, and Stefan Pogatscher. Size-dependent diffusion controls natural aging in aluminium alloys. *Nature Communications*, 10(1):1–6, 2019.

[29] W Lohmann, A Ribbens, WF Sommer, and BN Singh. Microstructure and mechanical properties of medium energy (600-800 MeV) proton irradiated commercial aluminium alloys. *Radiation Effects*, 101(1-4):283–299, 1987.

[30] Lukas Stemper, Matheus A Tunes, Ramona Tosone, Peter J Uggowitzer, and Stefan Pogatscher. On the potential of aluminum crossover alloys. *Progress in Materials Science*, 124:100873, 2022.

[31] Ruslan Z Valiev and Terence G Langdon. Principles of equal-channel angular pressing as a processing tool for grain refinement. *Progress in Materials Science*, 51(7):881–981, 2006.

[32] G Greaves, AH Mir, RW Harrison, MA Tunes, SE Donnelly, and JA Hinks. New microscope and ion accelerators for materials investigations (MIAMI-2) system at the University of Huddersfield. *Nuclear Instruments and Methods in Physics Research Section A: Accelerators, Spectrometers, Detectors and Associated Equipment*, 931:37–43, 2019.

[33] Xinghang Zhang, Khalid Hattar, Youxing Chen, Lin Shao, Jin Li, Cheng Sun, Kaiyuan Yu, Nan Li, Mitra L Taheri, Haiyan Wang, et al. Radiation damage in nanostructured materials. *Progress in Materials Science*, 96:217–321, 2018.

[34] Bachu Narain Singh, Torben Leffers, M Victoria, WV Green, and D Gavillet. Effects of 600 MeV proton irradiation on nucleation and growth of precipitates and helium bubbles in a high-purity Al-Mg-Si alloy. *Journal of Nuclear Materials*, 141:743–747, 1986.

[35] ZH Ismail. Effect of low dose neutron irradiation on the mechanical properties of an AlMgSi alloy. *Radiation Effects and Defects in Solids*, 112(4):105–110, 1990.

[36] LE Katz, H Herman, and AC Damask. Precipitation in neutron-irradiated Al-base Cu. *Acta Metallurgica*, 16(7):939–945, 1968.

[37] K Farrell. Microstructure and tensile properties of heavily irradiated 5052-0 aluminum alloy. *Journal of Nuclear Materials*, 97(1-2):33–43, 1981.

[38] KS Liu, O Kawano, Y Murakami, and H Yoshida. Structural changes in age-hardenable aluminium alloys induced by low temperature neutron irradiation. *Radiation Effects*, 15(1-2):37–49, 1972.

[39] IM Ghauri and Naveed Afzal. Effects of neutron irradiation on the stress relaxation rate in Al–Cu–Mg alloy. *Journal of Physics D: Applied Physics*, 40 (19):6044, 2007.

[40] IM Ghauri, Naveed Afzal, and Yasir Idrees. A study of microstructure and tensile properties of proton beam irradiated Al–Mg–Si alloy. *International Journal of Modern Physics B*, 25(12):1645–1652, 2011.

[41] Murthy Kolluri. Neutron Irradiation Effects in 5xxx and 6xxx Series Aluminum Alloys: A Literature Review. In *Radiation Effects in Materials*, volume 395, pages 116–124. InTech, 2016.

[42] Camille Flament, Joel Ribis, Jérôme Garnier, Y Serruys, F Leprêtre, A Gentils, C Baumier, M Descoins, D Mangelinck, A Lopez, et al. Stability of $\beta$" nano-phases in Al-Mg-Si (-Cu) alloy under high dose ion irradiation. *Acta Materialia*, 128:64–76, 2017.

[43] Lukas Stemper, Bernhard Mitas, Thomas Kremmer, Steffen Otterbach, Peter J Uggowitzer, and Stefan Pogatscher. Age-hardening of high pressure die casting AlMg alloys with Zn and combined Zn and Cu additions. *Materials & Design*, 181:107927, 2019.

[44] Lukas Stemper, Matheus A. Tunes, Paul Oberhauser, Peter J. Uggowitzer, and Stefan Pogatscher. Age-hardening response of AlMgZn alloys with Cu and Ag additions. *Acta Materialia*, 195:541 – 554, 2020. ISSN 1359-6454.

[45] Lukas Stemper, Matheus A Tunes, Phillip Dumitraschkewitz, Francisca Mendez-Martin, Ramona Tosone, Daniel Marchand, William A Curtin, Peter J Uggowitzer, and Stefan Pogatscher. Giant hardening response in AlMgZn (Cu) alloys. *Acta Materialia*, 206:116617, 2021.

[46] G. Bergman, J. L. T. Waugh, and L. Pauling. The crystal structure of the metallic phase $Mg_{32}(Al,Zn)_{49}$. *Acta Crystallographica*, 10(4):254–259, 1957.

[47] Bryan C Chakoumakos, Takashi Murakami, Gregory R Lumpkin, and Rodney C Ewing. Alpha-decay—Induced fracturing in zircon: The transition from the crystalline to the metamict state. *Science*, 236(4808):1556–1559, 1987.

[48] Yu Song, Songtao Zhan, Baohua Nie, Haiying Qi, Fangjun Liu, Touwen Fan, and Dongchu Chen. First-Principles Investigations on Structural Stability, Elastic Properties and Electronic Structure of $Mg_{32}(Al,Zn)_{49}$ Phase and $MgZn_2$ Phase. *Crystals*, 12(5):683, 2022.

[49] Matheus A Tunes, Cameron R Quick, Lukas Stemper, Diego SR Coradini, Jakob Grasserbauer, Phillip Dumitraschkewitz, Thomas M Kremmer, and Stefan Pogatscher. A fast and implantation-free sample production method for large scale electron-transparent metallic samples destined for MEMS-based in situ S/TEM experiments. *Materials*, 14(5):1085, 2021.

[50] James F Ziegler, Matthias D Ziegler, and Jochen P Biersack. SRIM–The stopping and range of ions in matter (2010). *Nuclear Instruments and Methods in Physics Research Section B: Beam Interactions with Materials and Atoms*, 268(11):1818–1823, 2010.

[51] R E Stoller, M B Toloczko, G S Was, A G Certain, S Dwaraknath, and F A Garner. On the use of SRIM for computing radiation damage exposure. *Nuclear*

*Instruments and Methods in Physics Research Section B: Beam Interactions with Materials and Atoms*, 310:75–80, sep 2013. ISSN 0168583X.

[52] CA English, BL Eyre, and ML Jenkins. Heavy-ion damage in $\alpha$-Fe. *Nature*, 263(5576):400–401, 1976.

# Chapter 5

# Precipitation behaviour in AlMgZnCuAg crossover alloy with coarse and ultrafine grains[*]

## Author´s Contribution

*Patrick D. Willenshofer* - Conceptualization, Methodology, Investigation, Visualization, Writing the original draft

*Matheus A. Tunes* - Visualization, Writing - Review and Editing

*Christina Kainz* - Investigation, Visualization, Writing - Review and Editing

*Oliver Renk* - Visualization, Writing - Review and Editing

*Thomas Kremmer* - Investigation, Visualization,Writing - Review and Editing

*Stefan Gneiger* - Investigation, Visualization, Writing - Review and Editing

*Peter J. Uggowitzer* - Conceptualization, Supervision, Writing - Review and Editing

*Stefan Pogatscher* - Project Administration, Conceptualization, Supervision, Writing - Review and Editing

---

[*] Status: Chapter 5 is published in the Journal Materials Research Letters, written by Patrick D. Willenshofer, Matheus A. Tunes, Christina Kainz, Oliver Renk, Thomas Kremmer, Stefan Gneiger, Peter J. Uggowitzer and Stefan Pogatscher.

## Acknowledgments

The research herein reported has been supported by both the European Research Council excellent science grant “TRANSDESIGN” through the Horizon 2020 program under contract 757961 and the Austrian Research Promotion Agency (FFG) in the project 3DnanoAnalytics (FFG-No 858040).

## Abstract

Crossover aluminium alloys have recently been introduced as a new class of coarse-grained age-hardenable alloys. Here, we study the evolution of precipitation of the T-Phase – $Mg_{32}(Zn,Al)_{49}$-phase – in a 5xxx/7xxx crossover alloy with coarse- and ultrafined microstructures. Both alloys were examined using differential scanning calorimetry, X-ray diffraction and *in situ* transmission electron microscopy. The ultrafine-grained alloy revealed significant different and accelerated precipitation behavior due to grain boundaries acting as fast diffusion paths. Additionally, the ultrafine-grained alloy revealed high resistance to grain growth upon heating, an effect primarily attributed to inter-granular precipitation synergistically with trans-granular precipitation of T-phase.

## 5.1 Introduction

To broaden the property profile while simultaneously improving sustainability [1], crossover alloying emerged as a promising strategy for research in the field of aluminium alloys. Such an approach was firstly developed for a crossover alloy merging the 5xxx and 7xxx [2, 3, 4, 5] aluminium alloy systems, and recently, it has been used to produce new alloys between 6xxx and 8xxx alloys [6]. In the 5xxx/7xxx crossover system, the T-phase – $Mg_{32}(Zn,Al)_{49}$ – was identified as the hardening precipitate. Although the T-phase of the Al–Mg–Zn ternary system is already known for decades [7, 8], the scientific interest has been rather low before introducing the crossover concept. Since then, however, the T-phase became the focus of intensive research in materials science. The T-phase is beneficial when used to inhibit grain growth or to generate particle stimulated nucleation [4], or even increase resistance to corrosion and hydrogen damage [9, 10, 11]. The age hardening potential by adding Cu and/or Ag was investigated, as reported by Stemper et al. [3, 5], as well as by other groups [12, 13]. Nevertheless, the precipitation sequence in coarse-grained (CG) Al-based crossover alloys is not yet fully exploited. Several groups presented different precipitation sequences as summarized by Stemper et al. [2]. Cu modifies the precipitation sequence as proposed by Hou et al. [14]: supersaturated solid solution (SSSS) → Guinier-Preston, fully coherent (GPI-zone) → T”, fully coherent (GPII-zone) → intermediate T’, semi-coherent → equilibrium T, incoherent. Moreover, Tunes et al. [15] found T-phase surviving upon heavy ion irradiation. Very recently the resistance of a crossover alloy against irradiation was strongly improved by reducing the grain size [16]. Specifically, these ultrafine-grained (UFG) crossover alloys aimed for applications in extreme environments, the precipitation behaviour has not been studied in detail so far, although it is known that a reduction in grain size to the nanometer scale may change the precipitation behavior significantly [17, 18]. The decrease in grain size is not only affecting the precipitation sequence of a given alloy, but consequently also its final mechanical properties [19, 20, 21, 22]. The process of precipitation within UFG regime exhibits variations compared to the CG counterpart. For instance, in cases where precipitates exist initially, severe plastic deformation (SPD) can result in the fragmentation or even dissolution of these precipitates into the matrix. This effect can lead to a state resembling a SSSS condition [23]. Conversely, SSSS with no initial precipitates present, SPD can induce dynamic precipitation [24]. Accelerated precipitation kinetics, as evidenced by Luo et al. [25], highlight an essential distinction compared to the CG material. This expedited precipitation phenomenon is attributed to the considerable density of defects adjacent to grain boundaries (GBs), potentially reaching values of up to $10^{17}$ $m^{-2}$ [26]. Moreover, the intermediate precipitation steps are often bypassed [17], leading directly to the precipitation of the equilibrium phase, even at lower temperatures. Therefore, precipitation sequences known from CG alloys need to be revised and reinvestigated. This study aims at systematically closing the knowledge gap in the precipitation behaviour of 5xxx/7xxx crossover alloys in different grain size regimes. The evolution of precipitates in both CG and UFG microstructral regimes is herein investigated through DSC measurements and characterized using X-ray diffraction (XRD) techniques and *in situ* transmission electron microscopy (TEM). A comprehensive evaluation on the overall thermal stability of the UFG structure is also performed.

## 5.2 Experimental

The chemical composition of the investigated crossover alloy is Al-4.9Mg-3.7Zn-0.6Cu-0.2Ag (determined via optical emission spectroscopy in wt.-%.). The CG alloys were processed by hot- and cold-rolling from 12 mm to 1.5 mm, followed by solution heat-treatment at 465°C/35 minutes and water quenching. High-pressure torsion (HPT) was carried out under a nominal hydrostatic pressure of 4 GPa for 10 revolutions at a rotational speed of 10 min/revolution using a disk with 12 mm height and 30 mm diameter. The investigations reported in this paper were performed after both the CG and UFG alloys experienced a storage time of 30 days at RT. It is important emphasizing that all thermal analysis experiments were performed at 10 $°C \cdot min^{-1}$.

Differential Scanning Calorimetry was carried out using a Netzsch 204DSC F1

Phönix device. Nitrogen was used both as a purge and protective gas (each 20 ml/min).

XRD measurements (Bruker AXS D8 Advance DaVinci diffractometer operating with Cu K$\alpha$ radiation) of fast cooled samples were performed to identify phases that precipitated. All experiments were performed in Bragg-Brentano geometry. Quantitative data on phase fraction was obtained through Rietveld refinement [27] that was performed using the software package Topas 6 by Bruker. Further details of the Rietveld refinement process for phase fraction estimation can be found elsewhere [28]. In addition, a series of prolonged isothermal aged specimens were measured to obtain information about the near-equilibrium state of the phases. All provided information of phase fraction within this research is corresponding to wt.-%.

Scanning Transmission Electron Microscopy (STEM) was carried out using a Thermo Fisher Scientific Talos F200X instrument. Thin foils were prepared by twin jet electro-polishing using a solution of 25 vol.-% nitric acid and 75 vol.-% methanol at a temperature range of -18 to -25°C and a voltage range of 12 to 14V. High angle annular dark field (HAADF), bright field (BF-TEM) and energy-dispersive X-ray spectroscopy (EDX) measurements were used. *In situ* heating was carried out using a micro-electro-mechanical system (MEMS) and a Protochips Fusion Select *in situ* heating/cooling holder with an uncoated e-chip. Preparation for *in situ* measurements were carried out according to literature [29]. The material was heat-treated within a TEM using a linear heating-rate of 10 °C·min$^{-1}$.

Thermodynamic assessments were carried out using Thermocalc 2023a with database TCAL8 to determine the phase fraction of the alloy system upon heating.

## 5.3 Results and Discussion

### 5.3.1 Precipitation sequence

Figure 5.1 a) and b) showing BFTEM images of the CG and UFG alloy, showcasing the difference in their grain size. The CG alloy reaches an average grain size of 54.6±2.6µm while for the UFG alloy, the average grain length reaches 294.3±109.8nm and the average grain width 91.4±36.6nm. The precipitation sequence for the CG and UFG alloy determined by DSC is displayed as heat-flow signals in Figure 5.1 c). The CG alloy shows exothermic peaks at 34, 233, 271, 306 and 445°C and endothermic peaks at 114 and 385°C. The development of precipitates in the CG alloy shares similarities to findings in experiments conducted by other research groups [30, 31, 14]. Defect recovery of the UFG alloy was not observed, but it may be overlaid by the precipitation signal in the DSC heat-flow [32].

The first peak at 34°C has been attributed to the formation of G.P. zones [25, 14]. Their partial dissolution can be seen upon further heating to 114°C. G.P. zones have been shown to enhance the age-hardening behaviour of the crossover alloy [12], even more pronounced when Cu and/or Ag is present. [3, 33, 34].

At 233°C, formation of metastable T"-phase precipitates is expected [14]. A peak at 271°C is not reported in the literature and is therefore assumed to be related with the nucleation of metastable T'-phase. It is not clear from literature whether the shoulder region at 306°C is anticipated to be the transformation of T"-phase → T'-phase [14], the transformation of T' → T [35] or nucleation of T-phase [36, 37]. The endothermic peak at 385°C represents most likely the dissolution of small-size T'-phase particles [30, 14]. The dissolution temperature of T-phase is reported between 430 and 485°C, which was not clearly observable during the DSC run in our experiments [38, 39, 40].

Reducing the grain size affects the precipitation behaviour of aluminium alloys [17], but as already mentioned, no comprehensive investigation for 5xxx/7xxx crossover alloys yet are known so far. As can be seen in Figure 5.1, the UFG alloy does not show an exothermic peak at low temperatures. Since UFG microstructures are rich in microstructural defects which provide fast diffusion paths [41], G.P. zones may have already formed during RT storage time, so that only their dissolution becomes visible as an endothermic peak at 110°C. Such behaviour was also observed in an UFG AA-7075 alloy [42]. The large exothermic peak at 183°C potentially relates to the maximum formation of a metastable phase. The following shoulder may be the transition to a more stable phase with its dissolution at higher temperature. However,

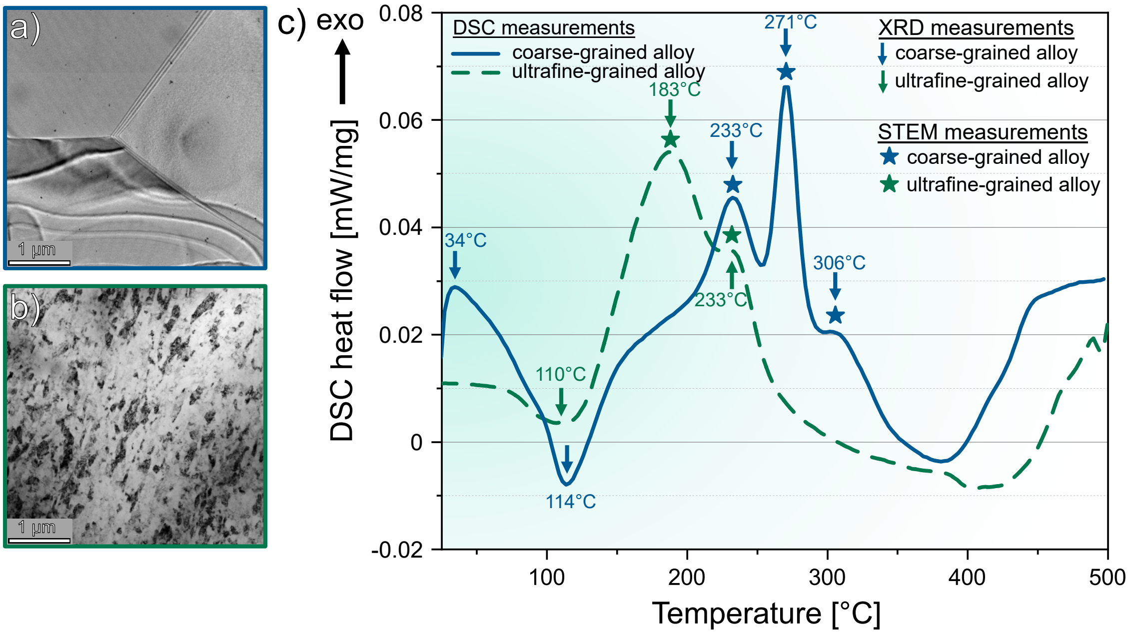

Figure 5.1: BFTEM images of a) the coarse- and b) ultrafined alloy. c) shows the DSC heat-flow curves of a coarse-grained (blue continuous line) AlMgCuZnAg crossover alloy after solution heat-treatment (465°C/35 min) and ultrafine-grained (green dashed line) AlMgCuZnAg crossover alloy. The sample was stored at RT for 30 days. The DSC experiments were performed with a linear heating rate of 10 °C·min$^{-1}$.

no further insight can be derived from the DSC curves.

It is noteworthy that both the CG and UFG alloys exhibit similar characteristics. It is quite feasible that the two exothermic peaks between 200 and 300°C in the CG alloy have merged into one major peak at 183 °C in the UFG alloy. Additionally, the precipitation temperature is shifted to lower temperatures, indicating higher precipitation kinetics in the UFG alloy, which can be attributed primarily to accelerated diffusion. As previously indicated, the type of precipitate strongly depends on the Zn/Mg ratio. As reported in [43, 44], when the Zn/Mg ratio is low, only T-phase precipitates are observed [45, 3]. Hence, given the alloy composition in our study, with a Zn/Mg ratio of 0.72, we expect to find exclusively T-phase particles. To validate these findings alongside our results and to study kinetics of the actual precipitates formed, we conducted XRD measurements at the peaks marked by arrows in Figure 5.1.

### 5.3.2 Phase evolution

To identify the precipitated phases, XRD measurements were performed. After linear heating the samples to the targeted peak temperatures of 34, 114, 233, 271 and 306°C for the CG alloy and 110, 183 and 233°C for the UFG alloy, we added an isothermal ageing time of 0, 1, 10 and 100h, respectively to evaluate kinetics.

The X-ray diffractograms of the CG samples are shown in Figure 5.2 a), b) and c). In addition to the diffractograms, also the standard peak positions of the fcc-Al matrix [46] and the T-phase [47] are shown. Note that Bigot et. al [48] observed that the equilibrium T-phase and its precursor exhibit a hardly distinguishable crystal structure. Consequently, XRD does not allow to distinguish between the precursor and the equilibrium T-phase, but can indicate that T-phase or precursors are present.

The lower peak temperatures, in particular 34 and 114°C, are not shown in Figure 5.2, because only reflections of the Al matrix were observed. They are thus not displayed in Figure 5.2. However, with increasing temperature, reflections peaks of T-phase become more distinct from 233°C/0h up to 233°C/100h of isothermal ageing. Their increase is marked with black arrows within Figure 5.2. This is also the case for 271 and 306°C. The increasing intensity of T-phase reflexes with increasing temperature and duration can be interpreted as the progressive formation of precipitates with T-phase structure.

The corresponding increase phase fraction is shown in Figure 5.2 d). When isothermal ageing was conducted at 233, 271, and 306°C in the as-heated conditions (0h), the phase fractions were measured to be 3.3, 4.1 and 3.5%, respectively. After 100h of isothermal ageing, the phase fractions at each temperature were 8.8, 9.5 and 8.9% indicating an approaching (quasi-)equilibrium state. This also fits very well to calculated values of 11.3, 9.9 and 8.6% for the T-phase fraction from Thermocalc.

The X-ray diffractograms of the UFG material are displayed in Figure 5.2 e), f) and g). Similar to the CG alloy, the UFG alloy shows an intensity increase of reflection peaks of precipitates with T-phase structure with increasing temperature and increasing ageing time.

The phase fraction of the T-phase is displayed in Figure 5.2 h). Even in the as-

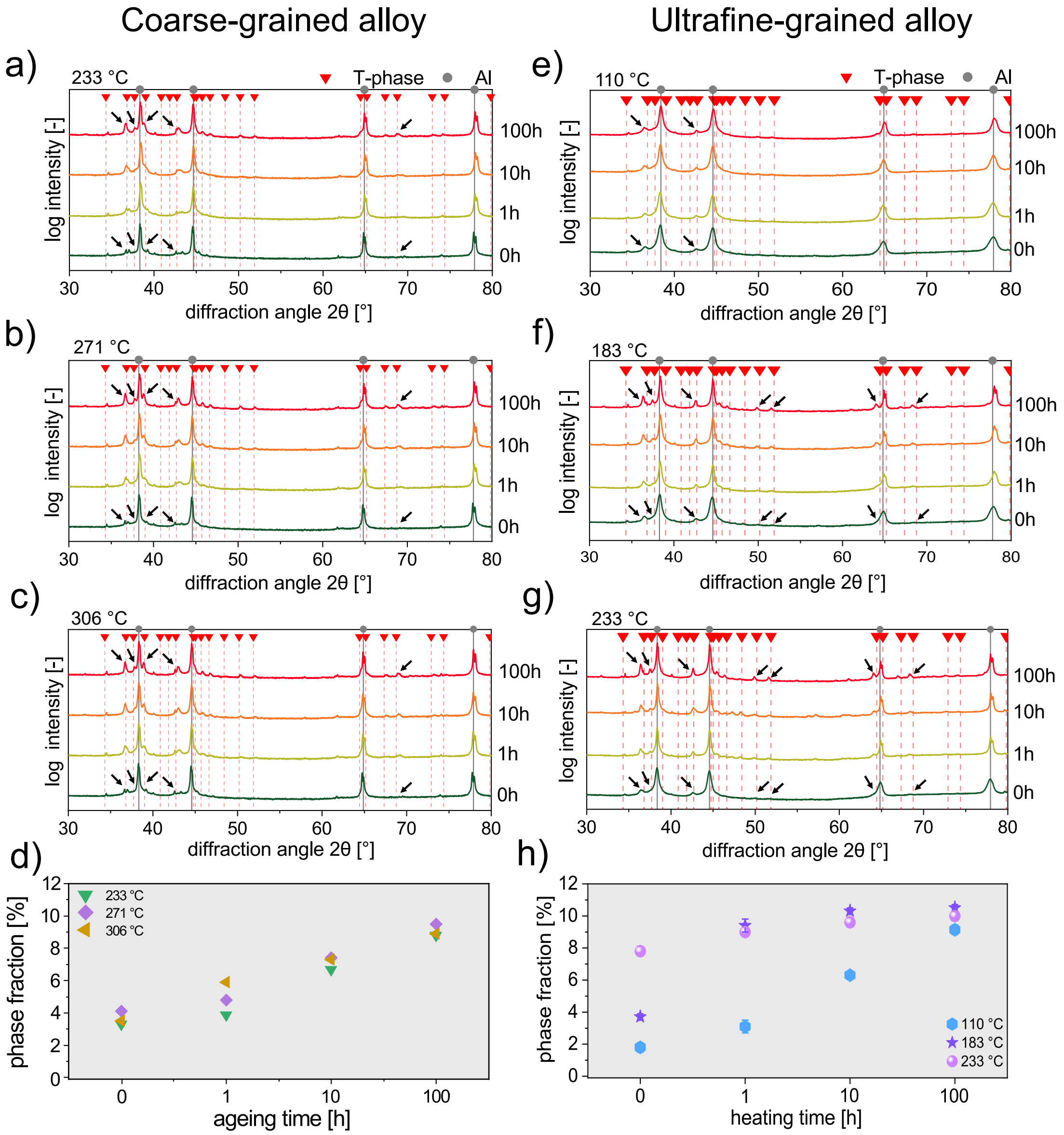

Figure 5.2: X-ray diffractograms of the coarse- and ultrafine-grained crossover Al alloy. The samples were heated with a linear heating rate of 10 °C·min$^{-1}$ up to a) 233°C, b) 271°C, c) 306°C and e) 110°C, f) 183°C, g) 233°C, respectively. The plot in in d) and h) display the phase fraction of T-phase as a function of temperature and duration of isothermal ageing of the CG alloy and the UFG alloy, respectively. Note that the phase fraction was determined by Rietveld refinement. Black arrows pointing out the increase of reflection peaks.

heated state (0h), volume fraction with a T-phase structure of 1.8, 3.7 and 7.8% were determined in the relatively low temperature range of 110, 183 and 233°C. It can be assumed that this observation is due to the fact that precipitates in UFG-structured materials can easily form via the benefits of preferential grain boundary diffusion [49]. After 1h at 110°C the phase fraction increases to 3.1%. When samples are heated at 183°C/1h and 233°C/1h, phase fractions of 9.0 and 9.4% were observed. Ageing for 10h leads to an increase of the phase fraction of the 110°C sample, resulting in 6.3%. Measurements at 183 and 233°C showing 10.3 and 9.6%, respectively. However, at 100h of isothermal ageing, all three samples exhibit again a (quasi-)equilibrium. The values of phase fraction for 110, 183 and 233°C are 9.1, 10.0 and 10.5%, respectively.

In summary, XRD measurements revealed, apart from Al matrix, the sole presence of phases with T-phase structure in both materials. However, the important question of the local position of the precipitates in the UFG material, at GBs or matrix, cannot be derived from XRD data. This will be answered by STEM investigations in the next section.

### 5.3.3 Precipitate characteristics

STEM investigations were carried out at 233, 271 and 306°C for the CG alloy and at 183 and 233°C for the UFG alloy in the as-heated condition, as indicated inFigure 5.1. As displayed in Figure 5.3 a), the investigations at 233°C revealed for the CG alloy that the main alloying elements Mg and Zn are present in the T-phase (note that no distinction is made between precursors and equilibrium of the T-phase). The elemental mappings does not clearly show an enrichment of Cu and Ag within the precipitate at this state. The morphology appears in a round shape and shows similarities as reported by Stemper *et al* [3]. Only very few elongated precipitates can be found as shown in Figure 5.3 a) in the HAADF image. The size of the particles is in average 6.7 ± 0.7 nm.

At 271°C, the incorporation of Cu and Ag within the T-phase was detected as shown in Figure 5.3 b). A detailed examination of the HAADF image reveals that the majority of the precipitates exhibit a spherical morphology. The presence of Cu and

Ag within the T-phase suggests their potential role in modifying the characteristics and properties of the precipitates. The particle size increased to 10.4 ± 1.4 nm.

At 306°C it is visible that Cu and Ag are clearly involved within the particles (Figure 5.3 c)). Cu may show a core/shell tendency, but a more detailed investigation is needed to fully clarify this issue. The morphology did not change significantly and their shape is predominantly spherical, but the size increased to 14.9 ± 5.2 nm.

The analysis of the UFG alloy at 183°C reveals the formation of elongated T-phase, consisting mainly of the alloying elemens Mg and Zn, and distributed preferably discontinuously at GBs (Figure 5.3 d)). This observation is an indication that no fully coherent precipitates participate in the first steps of the precipitation sequence, and that increased diffusion along GBs plays an important role. A similar UFG structure is also reported in literature [50, 51]. The T-phase thickness (*i.e.,* transverse length) were measured to be 7.1 ± 1.3 nm.

When the sample is heated to 233°C, precipitation within the matrix is visible in the UFG alloy Figure 5.3 e). Precipitation at GBs still occurs discontinuously, but the elongated T-phase slightly increased in thickness (12.4 ± 2.9 nm). At both precipitation sites, all alloying elements are incorporated into the T-phase. Precipitates within the grains appear to have both elongated and round shapes.

### 5.3.4 Thermal stability

Another important question arises regarding the thermal stability of both the UFG structure in terms of grain growth (recrystallization) and the T-phase precipitates in terms of growth and dissolution. We investigated this behaviour using *in situ* TEM heating experiments. The results are shown in Figure 5.4. Upon heating to 230°C, small precipitates can be seen primarily at GBs, which is consistent with the results presented in Figure 5.3. The UFG microstructure has not changed up to 280°C which can presumably be attributed to the pinning effect of T-phase particles on the GBs. At approximately 300°C, coalescence is noted and precipitates grow in size due to Ostwald ripening [52]. These particles, as indicated with an arrow, gradually diminish in size and eventually disappearing completely at 346°C. It should

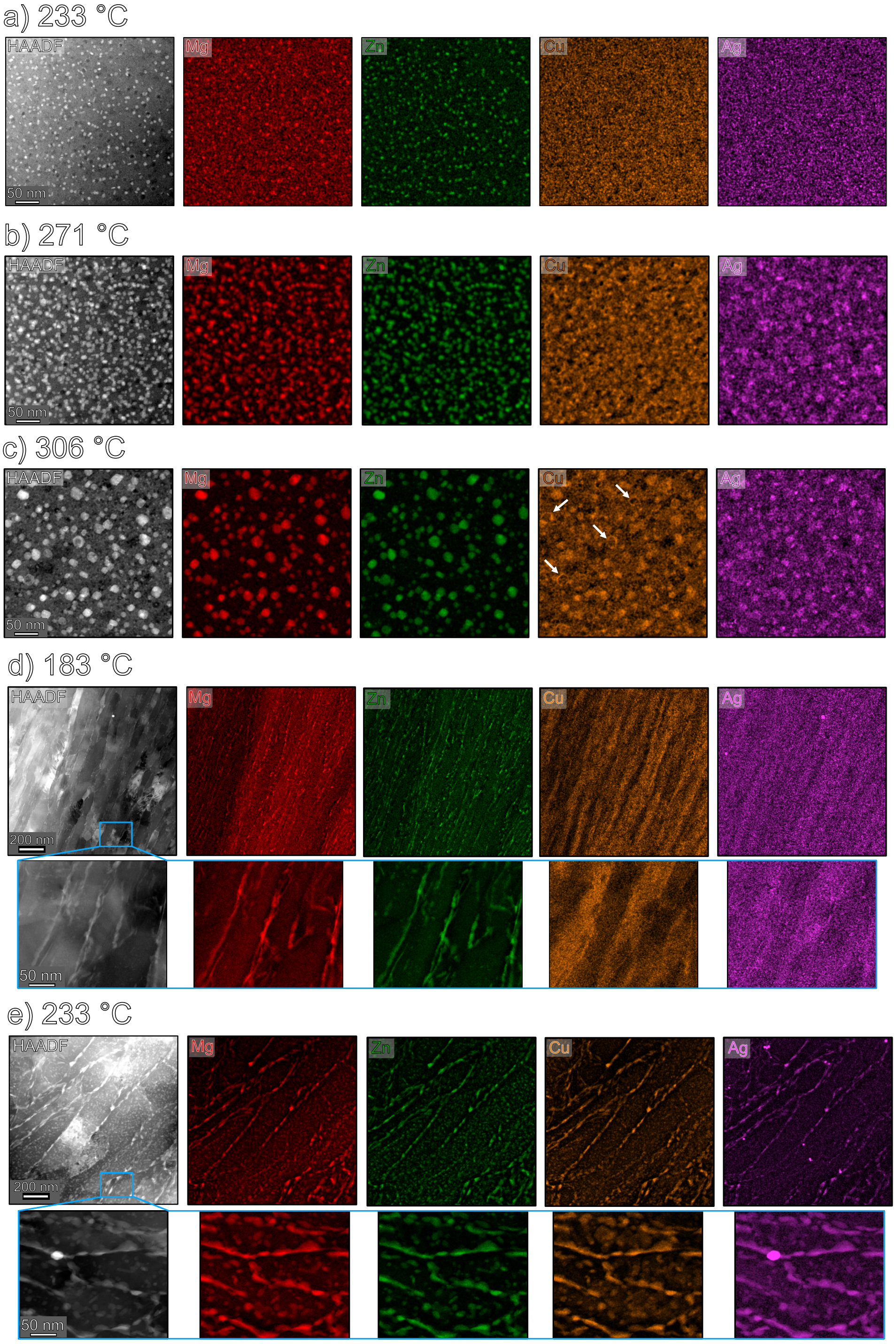

Figure 5.3: STEM HAADF and EDX elemental mappings of the coarse- and ultrafine-grained crossover Al alloy. The samples were heated with a linear heating rate of 10 °C·min$^{-1}$ up to a) 233°C, b) 271°C, c) 306°C for the CG alloy and to e) 183°C, f) 233°C for the UFG alloy.

be noted that the volume fraction of T-phase decreases with increasing temperature (solvus temperature according to Thermocalc simulation 450°C). Consequently, the precipitates partially dissolve, exemplified in Figure 5.4. Simultaneously, when T-phase particles are dissolving, the average grain size of the UFG microstructure is increasing.

However, the average grain size is still in the UFG regime. Given the significant amount of energy stored in GBs [53], UFG alloys are known to be susceptible to grain growth upon minimal heating [54, 55]. Dhal et al. [56] investigated a cryo-rolled AA-2024 alloy and observed the start of recrystallization at 100°C. Our study reveals that the grain size of the UFG crossover alloy remains unchanged up to 280°C and undergoes slow grain growth at temperatures beyond 300°C. Finally, the UFG microstructure completely diminishes at 380°C, showcasing the stabilizing effect of the T-phase particles on the UFG structure.

## 5.4 Conclusions

Coarse and a novel ultrafine-grained AlMgZnCuAg crossover alloy were investigated and the major differences were revealed using DSC, XRD and (*in situ*) TEM techniques. Grain size effects on the precipitation sequence were unravelled for an UFG aluminium crossover alloy for the first time. The grain size affects the precipitation behaviour and following conclusions can be drawn:

1. In both alloys, precipitation is governed by particles with T-phase structure-type. Isothermal ageing at different temperatures up to 100h did not change their crystal structure.

2. Kinetics of precipitation is different between CG and UFG alloys. The UFG alloy reaches equilibrium T-phase fraction faster and at lower temperature when compared with the CG alloy. This is most likely due to fast diffusion at GBs.

3. While for the CG alloy transgranular precipitation dominates, the UFG alloy is

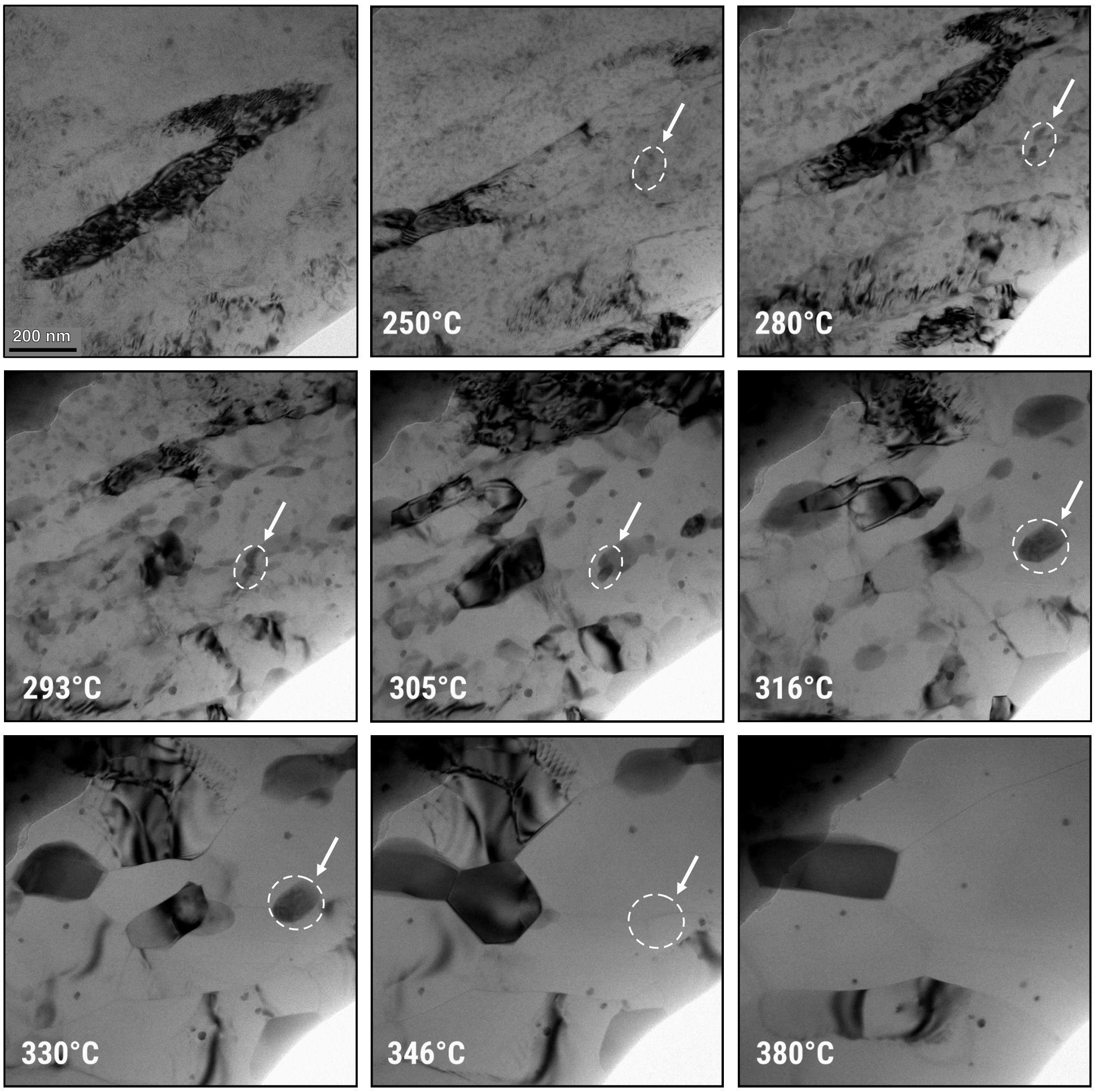

Figure 5.4: BFTEM images illustrating *in situ* TEM experiments conducted as a function of temperature on the UFG-AlMgZnCuAg alloy. The alloy underwent heat treatment using a MEMS Protochips system, employing a linear heating rate of 10 °C·min$^{-1}$. Images are extracted from the video file; the scale bar displayed at RT applies to all micrographs.

characterized by discontinuous precipitates at GBs (intragranular) accompanied by precipitates within the matrix.

4. Precipitation of the T-phase at GBs leads to a high thermal stability reflected by a resistance to grain growth in the UFG alloy up to 280°C.

## 5.5 Reference

[1] Dierk Raabe, Dirk Ponge, Peter J Uggowitzer, Moritz Roscher, Mario Paolantonio, Chuanlai Liu, Helmut Antrekowitsch, Ernst Kozeschnik, David Seidmann, Baptiste Gault, et al. Making sustainable aluminum by recycling scrap: The science of “dirty” alloys. *Progress in Materials Science*, 128:100947, 2022.

[2] Lukas Stemper, Matheus A Tunes, Ramona Tosone, Peter J Uggowitzer, and Stefan Pogatscher. On the potential of aluminum crossover alloys. *Progress in Materials Science*, 124:100873, 2022.

[3] Lukas Stemper, Bernhard Mitas, Thomas Kremmer, Steffen Otterbach, Peter J Uggowitzer, and Stefan Pogatscher. Age-hardening of high pressure die casting AlMg alloys with Zn and combined Zn and Cu additions. *Materials & Design*, 181:107927, 2019.

[4] Sebastian Samberger, Irmgard Weißensteiner, Lukas Stemper, Christina Kainz, Peter J Uggowitzer, and Stefan Pogatscher. Fine-grained aluminium crossover alloy for high-temperature sheet forming. *Acta Materialia*, 253:118952, 2023.

[5] Lukas Stemper, Matheus A Tunes, Phillip Dumitraschkewitz, Francisca Mendez-Martin, Ramona Tosone, Daniel Marchand, William A Curtin, Peter J Uggowitzer, and Stefan Pogatscher. Giant hardening response in AlMgZn (Cu) alloys. *Acta Materialia*, 206:116617, 2021.

[6] Bernhard Trink, Irmgard Weißensteiner, Peter J Uggowitzer, Katharina Strobel, and Stefan Pogatscher. High Fe content in Al-Mg-Si wrought alloys facilitates excellent mechanical properties. *Scripta Materialia*, 215:114701, 2022.

[7] GV Raynor and W Hume-Rothery. Equilibrium between $Al_2Mg_3Zn_3$ and the primary solid solution in the system aluminium-magnesium-zinc. *Transactions of the Faraday Society*, 44:29–36, 1948.

[8] Gunnar Bergman, John LT Waugh, and Linus Pauling. The crystal structure of the metallic phase $Mg_{32}(Zn,Al)_{49}$. *Acta Crystallographica*, 10(4):254–259, 1957.

[9] Cheng Cao, Di Zhang, Xu Wang, Qibiao Ma, Linzhong Zhuang, and Jishan Zhang. Effects of Cu addition on the precipitation hardening response and intergranular corrosion of Al-5.2 Mg-2.0 Zn (wt.%) alloy. *Materials Characterization*, 122:177–182, 2016.

[10] XB Yang, JH Chen, JZ Liu, F Qin, J Xie, and CL Wu. A high-strength AlZnMg alloy hardened by the T-phase precipitates. *Journal of Alloys and Compounds*, 610:69–73, 2014.

[11] Yafei Wang, Bhupendra Sharma, Yuantao Xu, Kazuyuki Shimizu, Hiro Fujihara, Kyosuke Hirayama, Akihisa Takeuchi, Masayuki Uesugi, Guangxu Cheng, and Hiroyuki Toda. Switching nanoprecipitates to resist hydrogen embrittlement in high-strength aluminum alloys. *Nature Communications*, 13(1):1–8, 2022.

[12] Cheng Cao, Di Zhang, Linzhong Zhuang, and Jishan Zhang. Improved age-hardening response and altered precipitation behavior of Al-5.2 Mg-0.45 Cu-2.0 Zn (wt%) alloy with pre-aging treatment. *Journal of Alloys and Compounds*, 691:40–43, 2017.

[13] Mami Mihara, Calin D Marioara, Sigmund J Andersen, Randi Holmestad, Equo Kobayashi, and Tatsuo Sato. Precipitation in an Al–Mg–Cu alloy and the effect of a low amount of Ag. *Materials Science and Engineering: A*, 658: 91–98, 2016.

[14] Shengli Hou, Pingping Liu, Di Zhang, Jishan Zhang, and Linzhong Zhuang. Precipitation hardening behavior and microstructure evolution of Al–5.1 Mg–

0.15 Cu alloy with 3.0 Zn (wt%) addition. *Journal of Materials Science*, 53(5): 3846–3861, 2018.

[15] Matheus A Tunes, Lukas Stemper, Graeme Greaves, Peter J Uggowitzer, and Stefan Pogatscher. Prototypic Lightweight Alloy Design for Stellar-Radiation Environments. *Advanced Science*, 7(22):2002397, 2020.

[16] Patrick D. Willenshofer, Matheus A. Tunes, Ho T. Vo, Lukas Stemper, Oliver Renk, Graeme Greaves, Peter J. Uggowitzer, and Stefan Pogatscher. Radiation-resistant aluminium alloy for space missions in the extreme environment of the solar system. Available at: https://arxiv.org/abs/2210.03397, 2022.

[17] T Hu, K Ma, TD Topping, JM Schoenung, and EJ Lavernia. Precipitation phenomena in an ultrafine-grained Al alloy. *Acta Materialia*, 61(6):2163–2178, 2013.

[18] Witold Chrominski and Malgorzata Lewandowska. Precipitation phenomena in ultrafine grained Al–Mg–Si alloy with heterogeneous microstructure. *Acta Materialia*, 103:547–557, 2016.

[19] KD Ralston, Dan Fabijanic, and Nick Birbilis. Effect of grain size on corrosion of high purity aluminium. *Electrochimica Acta*, 56(4):1729–1736, 2011.

[20] Piotr Bazarnik, Barbara Romelczyk-Baishya, Mariusz Kulczyk, and Malgorzata Lewandowska. The strength and ductility of 5483 aluminium alloy processed by various SPD methods. In *Materials Science Forum*, volume 765, pages 423–428. Trans Tech Publ, 2013.

[21] Muhammad Abubaker Khan, Yangwei Wang, Muhammad Hamza, Ghulam Yasin, Mohammad Tabish, Chuangshi Feng, Waheed Qamar Khan, Tahir Ahmad, Wei-Bing Liao, and Mohamed A Afifi. Precipitation behaviour in an Al-Zn-Mg-Cu alloy subjected to high strain rate compression tests. *Materials Characterization*, 180:111398, 2021.

[22] Muhammad Abubaker Khan, Chenhao Xu, Muhammad Hamza, Mohamed A Afifi, Naeem Akhtar Qaisrani, Huibin Sun, Bin Wang, Waheed Qamar Khan,

Ghulam Yasin, and Wei-Bing Liao. Enhanced tensile strength in an Al–Zn–Mg–Cu alloy via engineering the precipitates along the grain boundaries. *Journal of Materials Research and Technology*, 22:696–705, 2023.

[23] M Murayama, Zenji Horita, and K Hono. Microstructure of two-phase Al–1.7 at% Cu alloy deformed by equal-channel angular pressing. *Acta Materialia*, 49 (1):21–29, 2001.

[24] Hans J Roven, Manping Liu, and Jens C Werenskiold. Dynamic precipitation during severe plastic deformation of an Al–Mg–Si aluminium alloy. *Materials Science and Engineering: A*, 483:54–58, 2008.

[25] Jun Luo, Hongyun Luo, Sijie Li, Runze Wang, and Yue Ma. Effect of pre-ageing treatment on second nucleating of GPII zones and precipitation kinetics in an ultrafine grained 7075 aluminum alloy. *Materials & Design*, 187:108402, 2020.

[26] Hans Jørgen Roven, M Liu, Maxim Yu Murashkin, Ruslan Valiev, AR Kilmametov, Tamás Ungár, and L Balogh. Nanostructures and Microhardness in Al and Al–Mg Alloys Subjected to SPD. In *Materials Science Forum*, volume 604, pages 179–185. Trans Tech Publ, 2009.

[27] Robert Alan Young. *The Rietveld Method*, volume 5. International Union of Crystallography, 1993.

[28] Christina Kainz, Nina Schalk, Christian Saringer, and Christoph Czettl. In-situ investigation of the oxidation behavior of powdered TiN, Ti (C, N) and TiC coatings grown by chemical vapor deposition. *Surface and Coatings Technology*, 406:126633, 2021.

[29] Matheus A Tunes, Cameron R Quick, Lukas Stemper, Diego SR Coradini, Jakob Grasserbauer, Phillip Dumitraschkewitz, Thomas M Kremmer, and Stefan Pogatscher. A fast and implantation-free sample production method for large scale electron-transparent metallic samples destined for MEMS-based in situ S/TEM experiments. *Materials*, 14(5):1085, 2021.

[30] Nasser Afify, Abdel-Fattah Gaber, Ghada Abbady, et al. Fine scale precipitates in Al-Mg-Zn alloys after various aging temperatures. *Materials Sciences and Applications*, 2(05):427, 2011.

[31] M Chemingui, R Ameur, V Optasanu, and M Khitouni. DSC analysis of phase transformations during precipitation hardening in Al–Zn–Mg alloy (7020). *Journal of Thermal Analysis and Calorimetry*, 136:1887–1894, 2019.

[32] T Shanmugasundaram, BS Murty, and V Subramanya Sarma. Development of ultrafine grained high strength Al–Cu alloy by cryorolling. *Scripta Materialia*, 54(12):2013–2017, 2006.

[33] Yingxin Geng, Di Zhang, Jishan Zhang, and Linzhong Zhuang. Early-stage clustering and precipitation behavior in the age-hardened Al–Mg–Zn (-Cu) alloys. *Materials Science and Engineering: A*, 856:144015, 2022.

[34] Cheng Guo, Haitao Zhang, and Jiehua Li. Influence of Zn and/or Ag additions on microstructure and properties of Al-Mg based alloys. *Journal of Alloys and Compounds*, 904:163998, 2022.

[35] N Afify, A Gaber, and Gh Abbady. Characterization of the Developed Precipitates in Al-2 at.% Zn-x at.% Mg,(x= 1.8, 2, 2.4, 3, 4.2). *Light Metals 2013*, pages 431–436, 2016.

[36] XJ Jiang, J Tafto, B Noble, B Holme, and G Waterloo. Differential scanning calorimetry and electron diffraction investigation on low-temperature aging in Al-Zn-Mg alloys. *Metallurgical and Materials Transactions A*, 31:339–348, 2000.

[37] Peter Lang, Tomasz Wojcik, Erwin Povoden-Karadeniz, Ahmad Falahati, and Ernst Kozeschnik. Thermo-kinetic prediction of metastable and stable phase precipitation in Al–Zn–Mg series aluminium alloys during non-isothermal DSC analysis. *Journal of Alloys and Compounds*, 609:129–136, 2014.

[38] LEI Chuan, Qu-dong Wang, Hua-ping Tang, Tian-wen Liu, Zhong-yang Li, Hai-yan Jiang, WANG Kui, and Wen-jiang Ding. Effects of Mg content on

microstructure and mechanical properties of low Zn-containing Al-xMg-3Zn-1Cu cast alloys. *Transactions of Nonferrous Metals Society of China*, 32(3): 721–738, 2022.

[39] Ying Deng, Zhimin Yin, Jiaqi Duan, Kai Zhao, Bei Tang, and Zhenbo He. Evolution of microstructure and properties in a new type 2 mm Al–Zn–Mg–Sc–Zr alloy sheet. *Journal of Alloys and Compounds*, 517:118–126, 2012.

[40] Xiangzhen Zhu, Fuchu Liu, Shihao Wang, and Shouxun Ji. The development of low-temperature heat-treatable high-pressure die-cast Al–Mg–Fe–Mn alloys with Zn. *Journal of Materials Science*, 56:11083–11097, 2021.

[41] Sergiy V Divinski, Gerrit Reglitz, Harald Rösner, Yuri Estrin, and Gerhard Wilde. Ultra-fast diffusion channels in pure Ni severely deformed by equal-channel angular pressing. *Acta Materialia*, 59(5):1974–1985, 2011.

[42] Yonghao Zhao, Jizi Liu, Troy D Topping, and Enrique J Lavernia. Precipitation and aging phenomena in an ultrafine grained Al-Zn alloy by severe plastic deformation. *Journal of Alloys and Compounds*, 851:156931, 2021.

[43] Gloria Graf, Petra Spoerk-Erdely, Peter Staron, Andreas Stark, Francisca Mendez Martin, Helmut Clemens, and Thomas Klein. Quench rate sensitivity of age-hardenable Al-Zn-Mg-Cu alloys with respect to the Zn/Mg ratio: An in situ SAXS and HEXRD study. *Acta Materialia*, 227:117727, 2022.

[44] Ian Polmear, David StJohn, Jian-Feng Nie, and Ma Qian. *Light alloys: metallurgy of the light metals*. Butterworth-Heinemann, 2017.

[45] Tian-wen Liu, Qu-dong Wang, Hua-ping Tang, Zhong-yang Li, LEI Chuan, Mahmoud Ebrahimi, Hai-yan Jiang, and DING Wen-Jiang. Microstructure and mechanical properties of squeeze-cast Al-5.0 Mg-3.0 Zn-1.0 Cu alloys in solution-treated and aged conditions. *Transactions of Nonferrous Metals Society of China*, 30(9):2326–2338, 2020.

[46] A. P. Gulyaev and E. F. Trusova. Some Physical Properties and Some Solid Solutions of Al, Fe and Cu. *Zhurnal Tekhnicheskoi Fiziki*, 20:66, 1950.

[47] JH Auld and BE Williams. X-ray powder data of T phases composed of aluminium and magnesium with silver, copper or zinc. *Acta Crystallographica*, 21(5):830–831, 1966.

[48] Annabelle Bigot, Pierre Auger, Sylvain Chambreland, Didier Blavette, and Andrew Reeves. Atomic scale imaging and analysis of T'precipitates in Al-Mg-Zn alloys. *Microscopy Microanalysis Microstructures*, 8(2):103–113, 1997.

[49] Boryana Rashkova, Michael Faller, Reinhard Pippan, and Gerhard Dehm. Growth mechanism of $Al_2Cu$ precipitates during in situ TEM heating of a HPT deformed Al–3wt.% Cu alloy. *Journal of Alloys and Compounds*, 600: 43–50, 2014.

[50] Gulnaz Nurislamova, Xavier Sauvage, Maxim Murashkin, Rinat Islamgaliev, and Ruslan Valiev. Nanostructure and related mechanical properties of an Al–Mg–Si alloy processed by severe plastic deformation. *Philosophical Magazine Letters*, 88(6):459–466, 2008.

[51] Alexander P Zhilyaev, Azat A Gimazov, and Terence G Langdon. Recent developments in modelling of microhardness saturation during SPD processing of metals and alloys. *Journal of Materials Science*, 48:4461–4466, 2013.

[52] Peter W Voorhees. The theory of Ostwald ripening. *Journal of Statistical Physics*, 38:231–252, 1985.

[53] Xavier Sauvage, Gerhard Wilde, SV Divinski, Zenji Horita, and RZ Valiev. Grain boundaries in ultrafine grained materials processed by severe plastic deformation and related phenomena. *Materials Science and Engineering: A*, 540:1–12, 2012.

[54] Ruslan Z Valiev and Terence G Langdon. Principles of equal-channel angular pressing as a processing tool for grain refinement. *Progress in Materials Science*, 51(7):881–981, 2006.

[55] Malgorzata Lewandowska, Tomasz Wejrzanowski, and Krzysztof J Kurzydłowski. Grain growth in ultrafine grained aluminium processed by hydrostatic extrusion. *Journal of Materials Science*, 43(23):7495–7500, 2008.

[56] A Dhal, SK Panigrahi, and MS Shunmugam. Precipitation phenomena, thermal stability and grain growth kinetics in an ultra-fine grained Al 2014 alloy after annealing treatment. *Journal of Alloys and Compounds*, 649:229–238, 2015.

# Chapter 6

# Comparative analysis of experimental techniques for microstructural characterization of novel nanostructured aluminium alloys*

## Author´s Contribution

*Patrick D. Willenshofer* - Conceptualization, Methodology, Investigation, Visualization, Writing the original draft

*Diego S. R. Coradini* - Investigation, Visualization, Writing - Review and Editing

*Oliver Renk* - Investigation, Writing - Review and Editing

*Peter J. Uggowitzer* - Conceptualization, Supervision, Writing - Review and Editing

*Matheus A. Tunes* - Visualization, Writing - Review and Editing

---

*Status: Chapter 6 is published in the Journal Materials Characterization, written by Patrick D. Willenshofer, Diego S. R. Coradini, Oliver Renk, Peter J. Uggowitzer, Matheus A. Tunes and Stefan Pogatscher.

*Stefan Pogatscher* - Project Administration, Conceptualization, Supervision, Writing - Review and Editing

## Acknowledgments

The research herein reported has been supported by both the European Research Council excellent science grant "TRANSDESIGN" through the Horizon 2020 program under contract 757961 and the Austrian Research Promotion Agency (FFG) in the project 3DnanoAnalytics (FFG-No 858040).

## Abstract

Precipitation holds a pivotal role in comprehending the intrinsic behavior of materials. In the design of nanostructured metallic alloys, precipitates have found to increase the alloys' stability and response under extreme environmental conditions. Studies on precipitation often rely on conventional and *ex situ* electron-microscopy methods, but a systematic investigation that compares different sample conditions during heat treatment and its microstructural implications are rarely available. In this context, we employed a novel ultrafine-grained AlMgZnCuAg crossover alloy to compare three distinct conditions for investigating the precipitation sequence: (i) *ex situ* transmission electron microscopy (TEM) from bulk heating, (ii) *ex situ* TEM from TEM foil heating, and (iii) *in situ* TEM with microelectromechanical-system (MEMS) heating. Although the heat treatment procedure was consistent across all cases studied, the application of these three different experimental conditions in the same alloy system resulted in significant and non-negligible differences in the final precipitation behaviour. Ultimately, it resulted in observable microstructural variations and precipitates with distinctively different shape and sizes and, as a result, we outline herein the major similarities and differences among these techniques to achieve comparable results. This knowledge will help to compare and assess results of precipitation sequences obtained in different conditions.

## 6.1 Introduction

Al-Mg-Zn crossover alloys have emerged as a distinct class of materials within commercial aluminium alloy series, offering a remarkable combination of high strength, high ductility and several other unique properties attainable through the crossover alloying principle [1, 2, 3, 4, 5, 6, 7, 8]. To generate superior mechanical properties and microstructural stability in extreme environments (*i.e.* irradiation), there is a growing interest in achieving an ultrafine-grained (UFG) microstructure via severe plastic deformation (SPD) in Al-Mg-Zn crossover alloys [9, 5]. There are numerous methods to create UFG materials and high-pressure torsion (HPT) is one of the most effective methods to reduce grain sizes, as extremely high strains can be applied [10, 11].

In order to fully assess the properties and behaviour of this new crossover alloy class, particularly in the UFG regime, it is crucial to analyze the precipitation behaviour that occurs during a heat treatment [12, 13]. Precipitation is an inherent phenomenon occurring in nearly all classes of aluminium alloys [14] and is pivotal in determining their achievable strength. Therefore, microstructural analysis is one of the fundamental methods employed for understanding and optimizing the properties of a given material. Thus, understanding and analysing the precipitation sequence from a microstructural perspective plays a pivotal role in the field of aluminium crossover alloys [15].

Traditionally, precipitation analysis has been carried out alongside with the development of electron-microscopy methods, nowadays specifically scanning and/or transmission electron microscopy (comprising SEM, TEM and STEM), in concert with differential scanning calorimetry (DSC) methods. This allows to examine the heat-flow signal upon heating the alloy of interest in the DSC as well as to analyze microstructural changes in the electron-microscope [16, 13]. To track the precipitation sequence, one prepares samples which are heated to the temperature corresponding to the desired exothermic or endothermic peaks at the same rate, before quenching the sample. Subsequently, approximately 100 µm thin foils are prepared for TEM investigations at each temperature of interest [17, 18]. This methodology is herein referred to as "*ex situ* TEM from bulk heating" analysis in this work, and necessitates a new sample for each temperature (DSC peak) of interest.

Alternatively, *in situ* TEM experiments can be employed, requiring only one sample for a comprehensive precipitation analysis. Although focused ion beam milling is a common technique for TEM sample preparation [19], it is not widely recommended for aluminium samples due to Ga implantation and subsequent contamination during preparation and transfer onto the chip [20, 21]. However, literature suggested an alternative approach to avoid Ga implantation in Al-containing samples, providing a fast and contamination-free method using a scalpel to cut the electron-transparent region and transferring it on to a microelectromechanical systems (MEMS) chip [21, 22]. We studied and compared this technique in this paper, which will be referring to "*in situ* TEM with MEMS heating."

In addition to these two aforementioned techniques, we present a strategy to track the precipitation sequence in novel nanostructured crossover alloys. Our approach starts by preparing the TEM sample from the bulk material. After TEM sample preparation, the 3 mm TEM disk is subjected to heating in a well controlled furnace under atmospheric pressure and Nitrogen in a DSC. Therefore, this methodology will be referred to "*ex situ* TEM from TEM foil heating". To evaluate potential differences of the three techniques with respect to the precipitation sequence, we provide a systematic comparison between *ex situ* TEM from bulk heating, *ex situ* TEM from TEM foil and MEMS-based *in situ* TEM heating.

The use of *in situ* experiments is advantageous for directly monitoring various microstructural characteristics (e.g. grain growth, thermal stability or the precipitation of second-phase particles [13, 23, 24, 25, 26, 27]) that change continuously or at an unkown temperature during thermal treatments. However, because the electron-transparent region is very thin (approximately 100 nm), microstructural kinetics are significantly accelerated [28], making it challenging to compare these results with actual in-service conditions. This study aims to elucidate the differences among multiple analysed samples under different conditions, noting that similar trends were observed in different samples.

## 6.2 Materials and Methods

### 6.2.1 Alloy synthesis

The investigated alloy in this research is an UFG aluminium crossover alloy containing 4.8% Mg, 3.7% Zn, 0.6% Cu and 0.17% Ag as nominal chemical composition (in mass-%). The alloy was casted on laboratory scale with ≈100 g in weight in a copper mould to ensure high cooling rates [29]. After casting, the chemical composition of the slabs were measured on a milled surface with optical emission spectroscopy. To reduce the grain-size towards the submicron scale, HPT was carried out under a nominal hydrostatic pressure of 4 GPa for 10 revolutions at a rotational speed of 10 min/revolution resulting in a disk with 7 mm height and 30 mm diameter. After HPT, the alloy was stored at room temperature (RT) to achieve 30 days of natural aging (NA). This period allowed for stabilization of the material's microstructure, ensuring consistency and comparability among different specimens while conducting this study.

### 6.2.2 Sample preparation

The specimens used in this study were subjected to different preparation techniques based on each methodology. After NA, samples were cut with dimensions of approximately 10x7 mm$^2$ and a thickness of 1 mm. Following that, the samples were divided into three different batches: (A) *ex situ* TEM from bulk heating, (B) *ex situ* TEM from TEM foil, and (C) *in situ* TEM from MEMS heating.

#### Method (A): *ex situ* TEM from bulk heating

A sample of 1 mm thickness was subjected to heat-treatments in an air-circulating furnace using a linear heating rate of 0.16 K/s to 183°C. Following that, the sample was quenched into water thermalized at RT. Then it was manually ground down to an approximate thickness of 100 $\mu$m using different grades of SiC-Paper. Discs with a diameter of 3 mm were punched from these foils and subjected to twin jet electro-polishing in a Streuers TenuPol-5. The electrolyte solution consisted of 25%

nitric acid and 75% methanol (in vol.%). A temperature range of –25 to –20°C was measured during preparation. The potential between the electrodes was set between 12V and 14V. After electro-polishing, the disk underwent a thorough cleaning process. This involved immersing the sample in three separate containers, each filled with pure methanol. The cleaning steps ensured the removal of any residual contaminants or impurities, leaving behind a pristine surface. Following this, the sample was carefully dried using ambient air, allowing any remaining traces of methanol to evaporate.

### Method (B): *ex situ* TEM from TEM foil heating

A sample of 1 mm thickness was manually ground down to 100 $\mu$m thickness and a 3 mm disk was punched. Then, as mentioned above, TEM foil preparation was carried out. The electro-polished disk was placed within an aluminium crucible with a pierced lid, which was carefully positioned within the DSC machine for subsequent heat treatment. The same linear heating rate of 10 K/s as for method (A) was applied, gradually rising from RT to 183°C. The specimen was then quenched to RT within the DSC as fast as possible, with an approximate cooling rate of 50-100°C$\cdot$min$^{-1}$. Nitrogen (99.999 % purity) was used both as purge and protective gas, each 20 ml/min. It is worth emphasizing that the *ex situ* TEM from TEM foil heating methodology can be used with a single-disk approach. Following this, one single TEM disk could be used to semi-continuously analyse the resulting microstructure due to ageing. For example, it could be used to determine the microstructure after numerous ageing times (such as 1h, 10h, and so on).

### Method (C): MEMS-based *in situ* TEM heating

A Protochips fusion select *in situ* heating/cooling holder with an uncoated e-chip was used. Preparation for *in situ* measurements were carried out without using Focused Ion Beam via a recent method described in literature [21]. For this, electropolished samples were cut by a scalpel. An electron-transparent small sample with approx. 30x30µm$^2$ in size was obtained, which was then manually transferred to the chip of the MEMS protochips system. Subsequently, the heat-treatment was performed within the TEM and after the target temperature of 183°C with 0.16 K/s was reached, the sample was quenched to RT with 1000°C·s$^{-1}$.

### 6.2.3 Scanning/Transmission Electron Microscopy (S/TEM)

Electron microscopy was carried out using a Thermo Fisher Scientific™ Talos F200X scanning transmission electron microscope operating at 200 kV. The following imaging modes were used: bright-field TEM (BF-TEM), high-angle annular dark field (HAADF-STEM) with a camera length of 160 mm as well as energy-dispersive X-ray spectroscopy (EDX) measurements. The Velox software was used for image analysis.

## 6.3 Results and Discussion

### 6.3.1 Initial state of the UFG crossover alloy

It is important to understand the initial state of the UFG crossover alloy before delving into the precipitation study. Hence, we examined the impact of SPD via HPT at RT on the microstructure. HPT led to the formation of a homogeneous UFG microstructure characterized by elongated column-like grains. The origins of the studied samples is depicted in Figure 6.1 (a). The average grain size was measured to be 199±20 nm in length and a width of 62±4 nm, resulting in an corresponding average aspect ratio of 3.2. Notably, the grain size achieved in the UFG crossover alloy is significantly smaller than reported for similar UFG aluminium alloys. For example, a length of 430 nm and width of 150 nm was observed after ECAP in a 7075 Al series alloy [30], while a cryo-milled 5083 Al alloy exhibited 440 nm in equiaxed shape [31]. Figure 6.1 (b) shows a bright-field TEM (BF-TEM) micrograph of the bulk crossover alloy after HPT. It is crucial emphasizing that the initial starting microstructure of the UFG crossover alloy was consistent across all the methods discussed in this report. To gain further insight into the elemental distribution of the alloying elements after HPT, EDX analysis was performed, as shown in Figure 6.1 (c). After 30 days of natural aging (NA) at RT, the severely deformed microstructure shows no signs of larger precipitates, despite pure Ag nanophases. In previous research, the pristine material showed no signs of precipitation after a similar amount of NA time. Segregation of the elements on the grain boundaries was recorded [5]. However, one cannot rule out the presence of clusters (not T-phase) due to NA. The absence of T-phase type precipitates underscores the need for a heat treatment to stimulate phase precipitation within the material. Consistent with our findings, literature reports indicate that precipitates may dissolve during SPD, resulting in a state akin to a supersaturated solid solution of the alloy [32]. Conversely, it was noted that precipitates could emerge following HPT, indicating the activation of a dynamic precipitation process during SPD [33, 34], which was not evident in our investigation. To summarize, the aluminum crossover alloy attains an UFG single-phase state after HPT, without the presence of precipitates. Grain sizes are confined to the submicron scale, with sporadic Ag dispersoids observed transgranularly in the microstructure.

### 6.3.2 Comparison between the three different heat treatment techniques

All specimens underwent heat treatment with a consistent heating rate of 10°C per minute (= 0.16 K/s) from RT to 183°C. At this specific temperature, T-phase – $Mg_{32}(Zn, Al)_{49}$ – precipitates were found to nucleate and grow based on the Zn/Mg ratio of the alloy, which is the main hardening phase in the crossover system [35, 13]. The HAADF detector, which provides Z-contrast imaging, enabled the observation of T-phase precipitates along grain boundaries and also within the matrix, as depicted in Figure 6.2. Notably, the HAADF detector yielded varied results for the same alloy when employing three different heat treatment techniques. These outcomes are summarized below and in Table 6.1:

- *Ex situ* TEM from bulk heating: the majority of T-phase particles appear discontinuously at the grain boundaries (intergranular), and some few T-phase nanoparticles can be seen within the matrix (transgranular);
- *Ex situ* TEM from TEM foil heating: T-phase precipitates are observed at both intergranular and transgranular positions in higher densities when compared

with the aforementioned method; and

- *In situ* TEM with MEMS heating: the majority of T-phases exhibit a uniform distribution along the grain boundaries (intergranular), yet no precipitates are observed at transgranular positions, unlike the observations in the other two *ex situ* variants mentioned above.

The difference between these three distinct methods are also reflected in the chemical mappings shown in Figure 6.2. In the *ex situ* TEM analysis using bulk

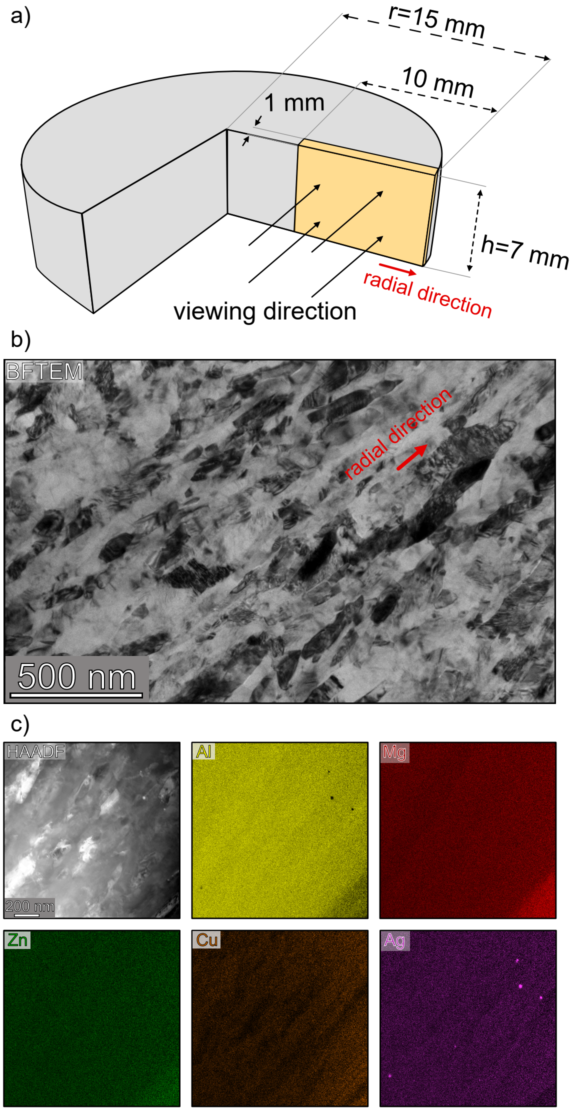

Figure 6.1: Nanostructured aluminium crossover alloy after HPT at RT with 30 days of natural ageing. (a) gives a schematic sketch of the HPTed disk, highlighting the viewing direction and the origins of the samples used. (b) BF-TEM image and (c) STEM-EDX mapping measurements showing the elemental maps of Al, Mg, Zn, Cu and Ag. The scale bar in the HAADF image in (c) applies to all elemental maps. The grains are elongated in the radial direction of the sample.

heating method, the distribution of elements reveals intriguing patterns. Mg is notably present within the T-phase at the grain boundaries, as well as in solid solution. The majority of Zn is observed at the T-phase present on the grain boundaries, but Zn is also found in solid solution. Conversely, Cu and Ag appear to remain predominantly in solid solution, with no apparent inclination towards incorporation within the T-phase particles. In case of UFG alloys, one must consider two aspects: Firstly, the extensive presence of grain boundaries, amplifies the occurrence of grain boundary precipitation, facilitated by rapid diffusion pathways [28]. Secondly, Mg and Zn exhibit notably high diffusion coefficient within the Al matrix, surpassing that of Cu by approximately two orders of magnitude [36]. Pure Ag nanoparticles were detected within the grain matrix, however, they were also present prior to the heat-treatment as shown in Figure 6.1, and neither their morphology nor distribution changed upon heating. Recently, a similar behavior was observed for Cu and Ag in the UFG crossover alloy [13]. During the heat treatment, a significant increase in grain length to 554±36 nm was noted, while the grain width increased to 87±6 nm. The increase in grain size is shown in Figure 6.4. The width of the T-phase precipitates was measured to be 11±1 nm.

The *ex situ* TEM from TEM foil heating method unveils a different picture. Notably, both Mg and Zn exhibit significant integration into the T-phase precipitates across inter- and transgranular regions. Surprisingly, despite the short heat treatment applied (183 °C with 0.16 K/s), Cu and Ag show a tendency towards integration into the T-phase particles, contrary to expectations. Both Cu and Ag are observed mainly

Table 6.1: Qualitative comparison between the three experimental methods in terms of T-phase precipitation at site-specific dependencies

| | **Specific site of T-phase precipitation** | |
|---|---|---|
| **Heating Method** | **Intergranular** | **Transgranular** |
| *Ex situ* TEM from bulk heating | Low | Low |
| *Ex situ* TEM from TEM foil heating | High | Medium |
| *In situ* TEM with MEMS heating | High | Zero |

at the grain boundaries, with neither element initially integrating into the T-phase particles within the matrix. Again, pure Ag nanoparticles were also detected but their morphology did not alter as a result of heating within the DSC. The average grain length after the application of the *ex situ* DSC method was measured to be 294±22 nm and an average grain width of 91±7 nm. The grain length exhibited an increase compared to the as-received condition, albeit not to the extent observed with the bulk analysis method. Moreover, the average particle thickness was found to be 10±1 nm, which is similar to the bulk analysis method.

Notably, with the *in situ* MEMS methodology, both Mg and Zn are present within the T-phase precipitates. Intriguingly, no precipitated phases were observed within the grains. However, similar to the *ex situ* bulk method, Cu and Ag appear only in solid solution, and almost no incorporation within the precipitated phases was detected. Additionally, it is noteworthy that no pure Ag nanoparticles were observed, but this might be attributed to a statistical effect due to the small area analyzed within the TEM sample on the MEMS chip. The grain size lies in between TEM foil heating and bulk heating methods with an average grain length of 455±25 nm and an average grain width of 86±5 nm. The average particle thickness was measured to be 9±1 nm, which is the smallest among all investigated methods, however, yet still within the same range. In summary, 30 grains and 40 second-phase particles were analysed to give a proper statistical overview. Measurements of the particles were taken from both particles on grain boundaries and matrix, if possible. A high magnification analysis of the microstructure is provided in Figure 6.3.

It is widely acknowledged that UFG materials can exhibit accelerated enhanced precipitation kinetics owing to their abundant grain boundaries, which serve as rapid diffusion pathways [37, 28]. Thus, precipitates will tend to predominantly nucleate and grow on the grain boundaries. However, there are still disparities in the state of precipitation, among the three techniques employed. This prompts the question: what factors contribute to the differences in precipitation behavior?

Firstly, it is reasonable to assume that regardless of the heating method used, all samples originated from a bulk material, thus all the studied samples have the same chemical composition. Therefore, differences in the materials' chemistry are negligible. It is worth emphasizing that when thermal experiments are carried out with the *ex situ* bulk method, a significant volume of material is heated compared to the other two methods, which could lead to different heat transport across the

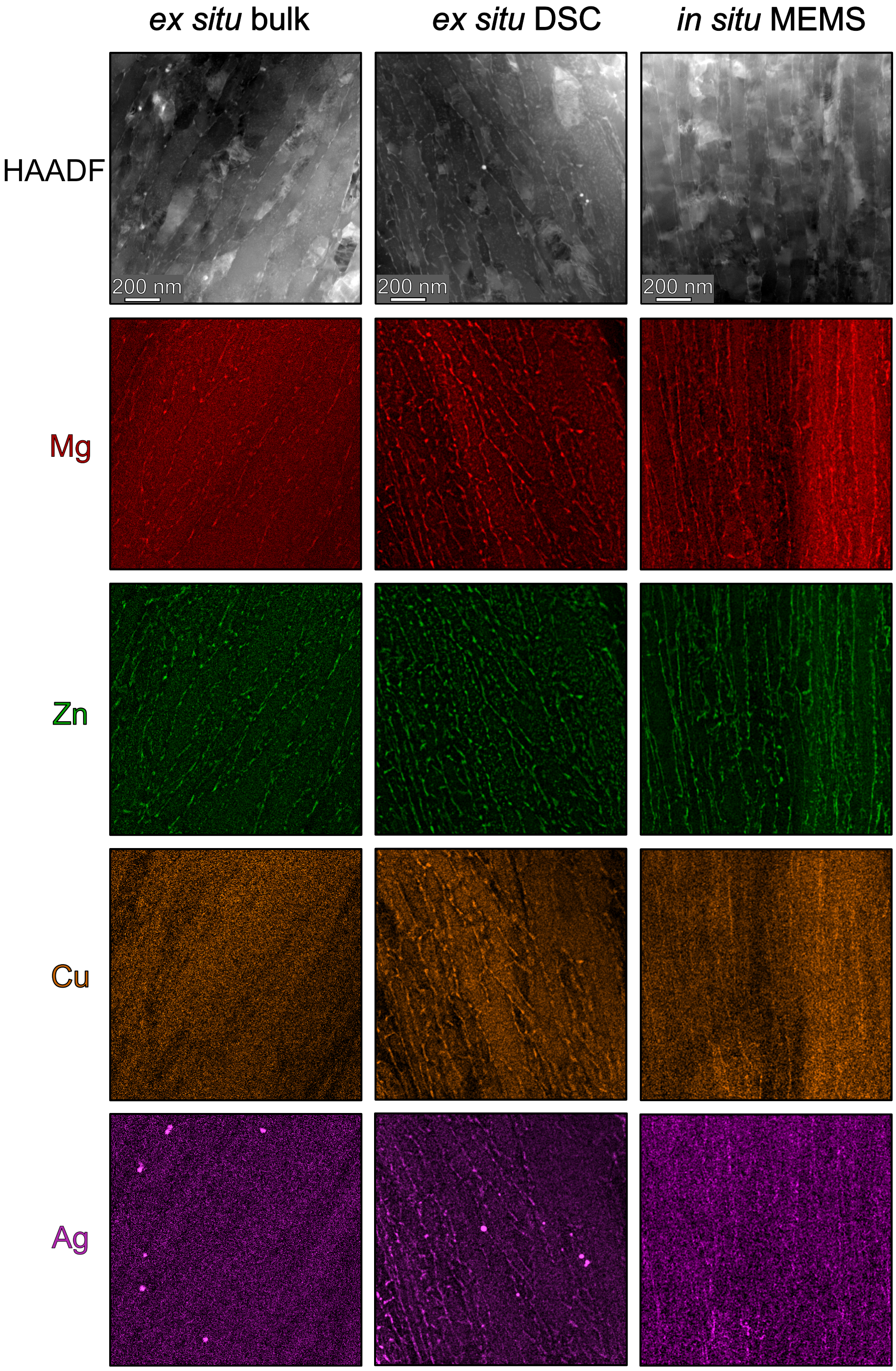

Figure 6.2: Low magnification STEM-EDX analysis of three different heat treatment techniques to analyze the precipitation behavior of an ultrafine-grained crossover alloy. The alloy was heat-treated with the same heating rate of 10 °C·min$^{-1}$ from RT to 183 °C. The shown scale bar in the HAADF-STEM image applies to all elemental maps shown below.

sample [38]. However, due to the slow linear heating rate of 0.16 K/s and the small sample size of 10x7x1 mm$^3$, it is reasonable to assume that the whole material was heated uniformly.

When looking at *ex situ* TEM from TEM foil heating and *in situ* TEM with

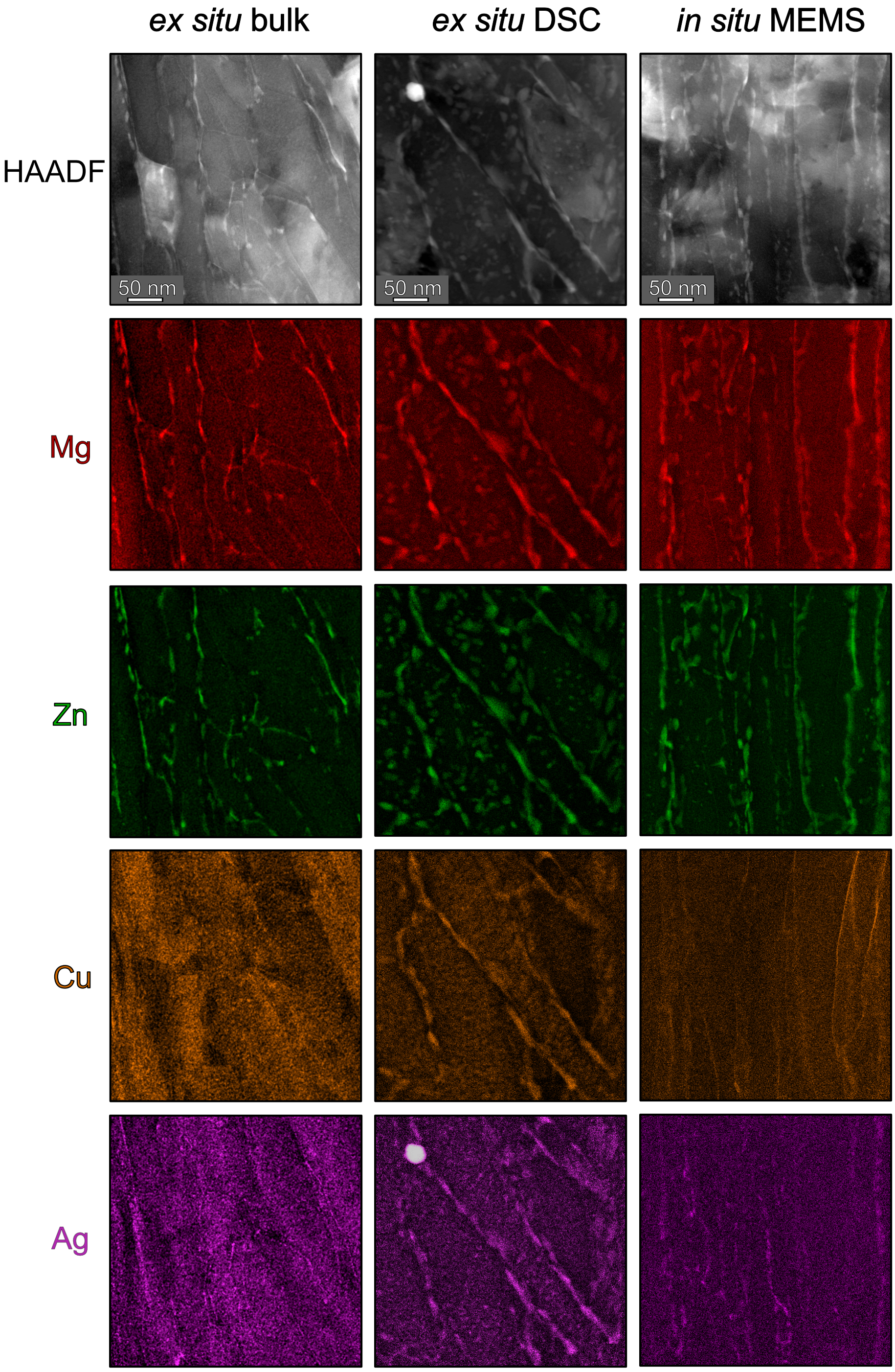

Figure 6.3: High magnification STEM-EDX analysis of three different heat treatment techniques to analyze the precipitation behavior of an ultrafine-grained crossover alloy. The alloy was heat-treated with the same heating rate of 0.16 K/s from RT to 183 °C. The shown scale bar in the HAADF-STEM image applies to all elemental maps shown below.

MEMS heating techniques, notably for the latter case, the sample is an electron-transparent region regarded as a thin-film. It was reported that the first layer of a metallic surface contains highly mobile vacancies, which can lead to enhanced diffusion within the superficial layers [39, 40]. Still, if precipitation in both *ex situ* TEM from TEM foil heating and *in situ* TEM with MEMS heating techniques are governed by the surface diffusion mechanism, the differences between those two are not easily justified.

To elucidate this phenomenon, it may be crucial to consider the environmental conditions during heating. *Ex situ* TEM from TEM foil heating occurred at ambient pressure. In contrast, the *in situ* TEM analysis utilizing MEMS heating was conducted at a TEM column pressure of approximately 3-8x$10^{-6}$ Pa. A recent investigation [41] revealed that Cu due to low column pressure can sublimate far below its melting point. However, the partial pressure of Mg and Zn in the surrounding atmosphere can be approximated to be practically zero in both *ex situ* TEM from TEM foil heating and *in situ* TEM with MEMS heating, since these are open systems with either a cold-finger or a fresh gas flow in the setup. The question remains why the *ex situ* TEM from TEM foil heating is faster in kinetics. A potential mechanism can be derived when looking at the surface conditions. Typically, it is assumed that surface diffusion can accelerate kinetics in thin film samples. However, in the *in situ* TEM with MEMS heating kinetics of precipitation seems to be slowest, even slower than in

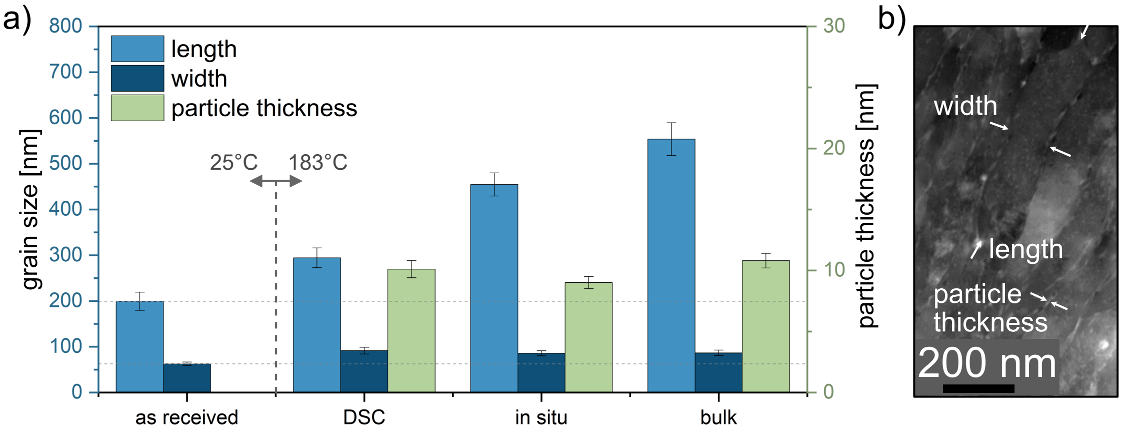

Figure 6.4: a) Graph depicting the average grain and particle sizes of the UFG crossover alloy. It illustrates the initial values (as-received) and the changes resulting from various heating techniques. b) Showing the method to measure the various microstructural characteristics.

the *ex situ* bulk method. It is reasonable that Mg and Zn will preferentially evaporate in the vacuum chamber conditions in the TEM when arrived at the surface and thus will not find their way back into the matrix to form precipitates. Hence acceleration of kinetics via surface diffusion is limited. Kinetics are likely to be reduced, since the atoms are lost instead of using a fast diffusion pathway. Note that this will be generally different for many other solute elements with low vapour pressure. In case of the *ex situ* TEM from TEM foil heating in a DSC, there is a technical nitrogen atmosphere (purity 99.999 %) at ambient pressure, but with a significant oxygen partial pressure present. This is widely accepted to be the case in commercial DSC systems and also leads in the analysis of Al to surface oxidation, even changing the colour of samples at higher temperature then applied here. It can be assumed that Mg atoms present at the surface are oxidised immediately [42, 43, 44]. This will form a barrier layer which capsules the system stopping evaporation. Note that such behavior will probably not be the case for other noble solute elements. However, the effect can enable for a fast diffusion pathway at the interface between alloy matrix and the oxide surface, since further Mg atoms are not lost and a thin film associated acceleration of diffusion is likely. This can explain the faster kinetics and the precipitation in the matrix for *ex situ* TEM from TEM foil heating compared to the *in situ* TEM with MEMS heating. It is even possible to explain the faster kinetics compared to the *ex situ* bulk method due to the extra diffusion at the interface. The proposed mechanism can well explain kinetics following the line *ex situ* TEM from TEM foil heating > *ex situ* bulk method > *in situ* TEM with MEMS heating.

Despite the different atmospheric conditions among all tested samples, it is also important to discuss the effect of different cooling rates, which are summarised in Table 6.2. While the *ex situ* TEM from bulk heating sample was quenched in water, the maximum cooling rate for this was 800 K/s [45]. However, there is a time gap between the final ageing temperature of 183 °C and water quenching. In this time gap, precipitation can still occur. Similarly, the *ex situ* TEM from TEM foil heating has the slowest cooling rate with 10 K/s, which is the maximum rate allowed by the machine. For the *in situ* TEM with MEMS heating sample, the maximum cooling

Table 6.2: Comparison of the three distinct conditions. While the heating rate in all conditions was controlled via 0.16 K/s, the cooling was set as fast as possible, which depends on the used setup. Furthermore, the atmosphere in all conditions is different and the sample thickness also varies. [45, 46]

| **Method** | **Heating Rate [K/s]** | **Cooling Rate [K/s]** | **Atmosphere** | **Sample Thickness** |
|---|---|---|---|---|
| *Ex situ* TEM from bulk heating | 0.16 | 800 | Air | 1 mm |
| *Ex situ* TEM from TEM foil heating | 0.16 | 10 | LN2 | 75 nm |
| *In situ* TEM with MEMS heating | 0.16 | 1000 | Quasi vacuum | 75 nm |

rate of can reach $10^6$ K/s [46] thus significantly hindering precipitation during cooling. For all the three cases studied, precipitation is mainly occurring during heating at a rate of 0.16 K/s for all conditions studied.

Another point arises when comparing the sample thicknesses. While *ex situ* TEM from bulk heating has the biggest sample volume, and therefore the biggest potential for precipitation growth, both *ex situ* TEM from TEM foil heating and *in situ* TEM with MEMS heating have a lower volume (electron-transparent samples). In these latter cases, precipitation growth is limited, as their sizes could already be in the same order of magnitude of the sample thickness. On the other hand, due to the reduced volume nearby the precipitates, the number of solute atoms is also reduced and the potential for precipitation growth could be inhibited, while kinetics may be increased (thin film effect).

Although EDX mappings were acquired, the accuracy of the measurements is not sufficient for exact quantification, yet, a qualitatively trend can be seen. For example, the Mg/Al ratio in both *ex situ* conditions are higher compared to the *in situ* condition, which supports the hypothesis of Mg evaporation during *in situ* experiments. A plot of the signal is shown in the supplementary materials in Figure 1. Note that the signals are normalised to the Al peak. Furthermore, an increase in the oxygen peak was observed in the *ex situ* TEM from TEM foil heating, which could be explained by the formation of an oxide layer on the sample's surface, and thus enhancing the precipitation kinetics.

Modelling and computation improve the design of materials. In particular, TEM techniques that provide continuous, direct insight into microstructural evolution (such as the methods presented here) can provide robust data sets for testing and calibrating models in a short time. [47, 48, 49]

Figure 6.4 shows the average grain size in terms of length and width as well as the particle thickness of the T-phase precipitates upon the three different conditions investigated. While the pristine condition (Figure 6.1 b) was found to have the smallest grain size, an increase in grain length and width was measured (Figure 6.2). The results of such measurements are shown in Figure 6.4. Nonetheless, all three methodologies exhibit overlapping uncertainties and lacks therefore statistical significance. The particle thickness of T-phase precipitates upon heating to 183°C is in the same range in all tested methodologies. These particular features can be explained considering the precipitation regimes displayed in Table 6.1. When both, matrix grains and grain boundaries are only weakly occupied by precipitates, which is the case with *ex situ* TEM bulk heating, then growth becomes apparent. It is also worth emphasizing that grain growth in thin films is limited [50]. Thus, grains in the *ex situ* bulk can grow more easily, which is also reflected in Figure 6.4. In addition, the lowest grain length is observed in the *ex situ* from TEM foil heating, where qualitatively most precipitates are found, as shown in Table 6.1. The major disparity in microstructure between *ex situ* TEM from TEM foil heating and *in situ* TEM heating from MEMS – evident in Figure 6.2 and qualitatively in Table 6.1 – lies in the absence of intergranular precipitation in the former, while the latter displays a moderate fraction of precipitates at these sites. This experimental confirmation underscores the role of T-phase precipitates in grain boundary pinning and thus restricting grain growth, particularly when they are abundant at grain boundaries, but also present at transgranular sites. For instance, in the case of *in situ* TEM with MEMS heating, where the T-phase is absent from the matrix, a modest grain growth (in length) is observed. Collectively, these results highlight the potential of various heat treatment methodologies, when carefully assessed and post-characterized, to facilitate microstructural engineering in emerging nanostructured aluminium alloys. To fully address and understand the mechanisms of the observed sublimation with the *in situ* MEMS heating method, further investigations should be carried out in future.

## 6.4 Conclusions

In summary, this paper evaluates innovative methods to explore and quantify precipitation and the stability of nanostructured metals through STEM. The methods discussed involves *ex situ* TEM from bulk heating, *ex situ* TEM from TEM foil heating, and *in situ* TEM with MEMS Protochips. The advantage of using a single-disk for investigations is to gather the information on the same region of interest in a (semi-)continuous approach. Microstructural changes upon (isothermal) heating can be then observed. Using a TEM foil subjected to external furnace heating (e.g., a DSC device) in an *ex situ* configuration, the introduced TEM foil heating method presents several practical benefits. It enables for an alternative to an *in situ* TEM/MEMS approach, sidestepping the necessity for supplementary equipment within the S/TEM configuration and examining several different heat treatment steps at one single sample. This renders it a convenient and readily accessible choice for more laboratories and researchers.

By comparing the results obtained from the various methodologies, it becomes apparent that different preparation techniques facilitate the analysis of precipitation behavior. Moreover, this study illuminates both the similarities and differences among the three demonstrated methods, providing valuable insights for researchers in the field of materials analysis. By presenting an efficient and reliable alternative, the *ex situ* TEM from TEM foil heating method opens up new avenues of exploring precipitation behaviors and better understanding of material properties.

## 6.5 Appendix

The following Figure 6.5 displays the acquired EDX signal. The signal for all three studied conditions was normalised to the highest peak (Al-K$\alpha$1). The left image displays the O-K$\alpha$1 energy line, where an increase in the intensity for the *ex situ* TEM from TEM foil heating can be found. This increase in intensity could be linked with the formation of an oxide layer on the sample's surface.

The image in the middle shows both the Mg-K$\alpha$1 and the Al-K$\alpha$1 line. While the normalisation of the peak signals can be seen in the overlapping Al peaks, a decrease in the intensity of Mg is recorded. The right image shows a magnification of this section, where this decrease can be seen clearer upon the Mg-K$\alpha$1 line. This decrease could be explained by the sublimation of Mg upon heating during *in situ* experiments within the TEM.

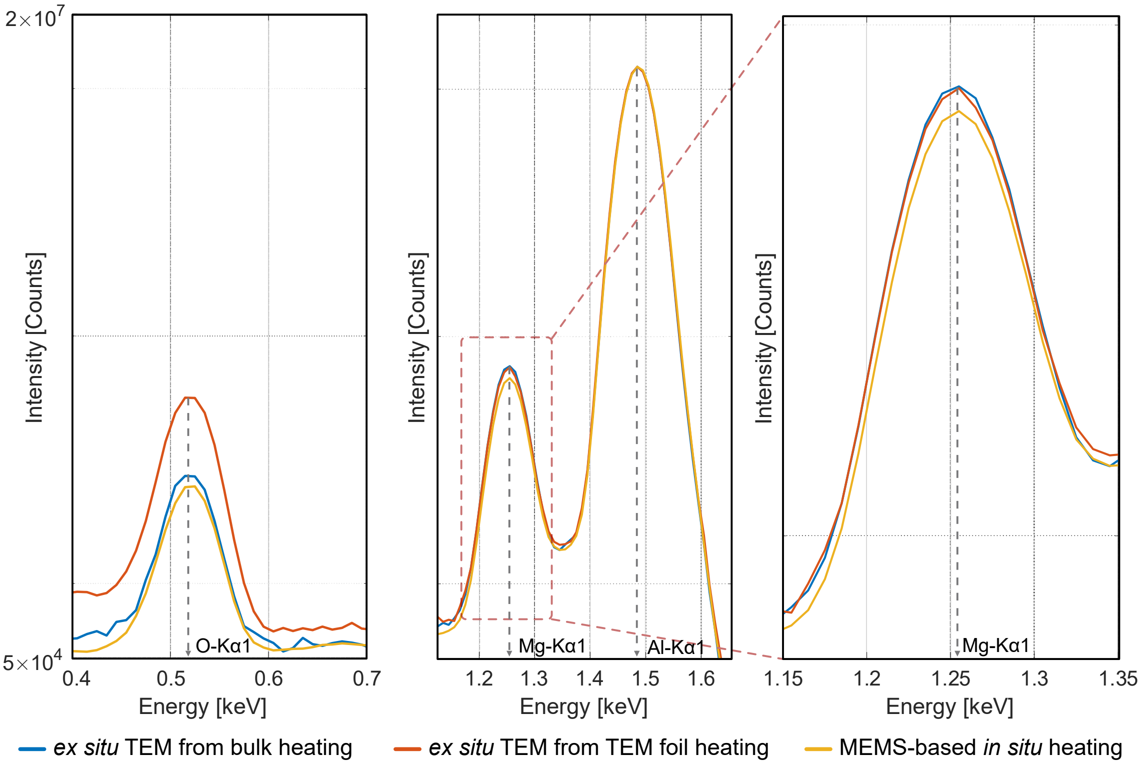

Figure 6.5: Plot of the signals acquired by EDX mappings in three different conditions. A qualitatively trend can be seen. Left: increase of the oxygen signal in the *ex situ* TEM from TEM foil heating. Middle: a decrease in the Mg signal in the MEMS-based *in situ* heating. Right: higher magnification of the Mg signal. Note that the signal is normalised to the Al peak and the y-axis is logarithmic.

## 6.6 Reference

[1] Florian Schmid, Lukas Stemper, and Ramona Tosone. Amag crossalloy®—a unique aluminum alloy concept for lightweighting the future. In Stephan Broek, editor, *Light Metals 2023*, pages 500–504. Springer Nature Switzerland, Cham, 2023. ISBN 978-3-031-22532-1.

[2] Sebastian Samberger, Irmgard Weißensteiner, Lukas Stemper, Christina Kainz, Peter J Uggowitzer, and Stefan Pogatscher. Fine-grained aluminium crossover alloy for high-temperature sheet forming. *Acta Materialia*, 253:118952, 2023.

[3] Lukas Stemper, Matheus A Tunes, Ramona Tosone, Peter J Uggowitzer, and Stefan Pogatscher. On the potential of aluminum crossover alloys. *Progress in Materials Science*, 124:100873, 2022.

[4] Matheus A Tunes, Lukas Stemper, Graeme Greaves, Peter J Uggowitzer, and Stefan Pogatscher. Prototypic Lightweight Alloy Design for Stellar-Radiation Environments. *Advanced Science*, 7(22):2002397, 2020.

[5] Patrick D Willenshofer, Matheus A Tunes, Ho T Vo, Lukas Stemper, Oliver Renk, Graeme Greaves, Peter J Uggowitzer, and Stefan Pogatscher. Radiation-resistant aluminium alloy for space missions in the extreme environment of the solar system. Available at: https://arxiv.org/abs/2210.03397.

[6] Chunyan Meng, Di Zhang, Hua Cui, Linzhong Zhuang, and Jishan Zhang. Mechanical properties, intergranular corrosion behavior and microstructure of Zn modified Al–Mg alloys. *Journal of Alloys and Compounds*, 617:925–932, 2014.

[7] Chunyan Meng, Di Zhang, Linzhong Zhuang, and Jishan Zhang. Correlations between stress corrosion cracking, grain boundary precipitates and Zn content of Al–Mg–Zn alloys. *Journal of Alloys and Compounds*, 655:178–187, 2016.

[8] Yafei Wang, Bhupendra Sharma, Yuantao Xu, Kazuyuki Shimizu, Hiro Fujihara, Kyosuke Hirayama, Akihisa Takeuchi, Masayuki Uesugi, Guangxu Cheng, and

Hiroyuki Toda. Switching nanoprecipitates to resist hydrogen embrittlement in high-strength aluminum alloys. *Nature Communications*, 13(1):6860, 2022.

[9] Weilin Yan, Xiaohong Liu, Jinyuan Huang, and Lin Chen. Strength and ductility in ultrafine-grained wrought aluminum alloys. *Materials & Design*, 49:520–524, 2013.

[10] Akira Azushima, Reiner Kopp, Antti Korhonen, Dong-Yol Yang, Fabrizio Micari, GD Lahoti, Peter Groche, Jun Yanagimoto, N Tsuji, Andrzej Rosochowski, et al. Severe plastic deformation (SPD) processes for metals. *CIRP Annals*, 57 (2):716–735, 2008.

[11] Alexander P Zhilyaev and Terence G Langdon. Using high-pressure torsion for metal processing: Fundamentals and applications. *Progress in Materials Science*, 53(6):893–979, 2008.

[12] Cheng Guo, Haitao Zhang, Shanshan Li, Rixin Chen, Yunfei Nan, Lei Li, Ping Wang, Baomian Li, Jianzhong Cui, and Hiromi Nagaumi. Evolution of microstructure, mechanical properties and corrosion behavior of Al-4Mg-2Zn-0.3 Ag (wt.%) alloy processed by T6 or thermomechanical treatment. *Corrosion Science*, 188:109551, 2021.

[13] PD Willenshofer, Matheus Araujo Tunes, Christina Kainz, Oliver Renk, Thomas M Kremmer, Stefan Gneiger, Peter J Uggowitzer, and Stefan Pogatscher. Precipitation behaviour in AlMgZnCuAg crossover alloy with coarse and ultrafine grains. *Materials Research Letters*, 11(12):1063–1072, 2023.

[14] Ian Polmear, David StJohn, Jian-Feng Nie, and Ma Qian. *Light alloys: metallurgy of the light metals*. Butterworth-Heinemann, 2017.

[15] Lukas Stemper, Bernhard Mitas, Thomas Kremmer, Steffen Otterbach, Peter J Uggowitzer, and Stefan Pogatscher. Age-hardening of high pressure die casting AlMg alloys with Zn and combined Zn and Cu additions. *Materials & Design*, 181:107927, 2019.

[16] Reza S Yassar, David P Field, and Hasso Weiland. Transmission electron microscopy and differential scanning calorimetry studies on the precipitation sequence in an Al–Mg–Si alloy: AA6022. *Journal of Materials Research*, 20 (10):2705–2711, 2005.

[17] Assel Aitkaliyeva, James W Madden, Brandon D Miller, James I Cole, and Jian Gan. Comparison of preparation techniques for nuclear materials for transmission electron microscopy (TEM). *Journal of Nuclear Materials*, 459: 241–246, 2015.

[18] Duggi V. Sridhara Rao, K. Muraleedharan, and C. Humphreys. TEM specimen preparation techniques. Available at: https://api.semanticscholar.org/CorpusID:7945310, 2010.

[19] Lucille A Giannuzzi and Frederick A Stevie. A review of focused ion beam milling techniques for TEM specimen preparation. *Micron*, 30(3):197–204, 1999.

[20] Kinga A Unocic, Michael J Mills, and GS Daehn. Effect of gallium focused ion beam milling on preparation of aluminium thin foils. *Journal of Microscopy*, 240(3):227–238, 2010.

[21] Matheus A Tunes, Cameron R Quick, Lukas Stemper, Diego SR Coradini, Jakob Grasserbauer, Phillip Dumitraschkewitz, Thomas M Kremmer, and Stefan Pogatscher. A fast and implantation-free sample production method for large scale electron-transparent metallic samples destined for MEMS-based in situ S/TEM experiments. *Materials*, 14(5):1085, 2021.

[22] Jack W Judy. Microelectromechanical systems (MEMS): fabrication, design and applications. *Smart Materials and Structures*, 10(6):1115, 2001.

[23] Tsai-Fu Chung, Yo-Lun Yang, Bo-Ming Huang, Zhusheng Shi, Jianguo Lin, Takahito Ohmura, and Jer-Ren Yang. Transmission electron microscopy investigation of separated nucleation and in-situ nucleation in AA7050 aluminium alloy. *Acta Materialia*, 149:377–387, 2018.

[24] Jayshri Dumbre, Shravan K Kairy, Elaf Anber, Timothy Langan, Mitra L Taheri, Thomas Dorin, and Nick Birbilis. Understanding the formation of (Al,Si)$_3$Sc and V-phase (AlSc$_2$Si$_2$) in Al-Si-Sc alloys via ex situ heat treatments and in situ transmission electron microscopy studies. *Journal of Alloys and Compounds*, 861:158511, 2021.

[25] Mingjun Yang, Andrey Orekhov, Zhi-Yi Hu, Man Feng, Shenbao Jin, Gang Sha, Kai Li, Vahid Samaee, Min Song, Yong Du, et al. Shearing and rotation of $\beta$ and $\beta$ precipitates in an Al-Mg-Si alloy under tensile deformation: In-situ and ex-situ studies. *Acta Materialia*, 220:117310, 2021.

[26] Arya Chatterjee, Liang Qi, and Amit Misra. In situ transmission electron microscopy investigation of nucleation of GP zones under natural aging in Al-Zn-Mg alloy. *Scripta Materialia*, 207:114319, 2022.

[27] Jiao Chen, Kenta Yoshida, Tomoaki Suzudo, Yusuke Shimada, Koji Inoue, Toyohiko J Konno, and Yasuyoshi Nagai. In Situ TEM Observation and MD Simulation of Frank Partial Dislocation Climbing in Al–Cu Alloy. *Materials Transactions*, 63(4):468–474, 2022.

[28] Boryana Rashkova, Michael Faller, Reinhard Pippan, and Gerhard Dehm. Growth mechanism of Al2Cu precipitates during in situ TEM heating of a HPT deformed Al–3wt.% Cu alloy. *Journal of Alloys and Compounds*, 600: 43–50, 2014.

[29] Florian Schmid, Lukas Stemper, T Ebner, Walter Leitner, and Stefan Pogatscher. Industry-oriented sample preparation of 6xxx and 5xxx aluminum alloys in laboratory scale. In *Proceedings of the EMC*, pages 639–652, 2019.

[30] YH Zhao, XZ Liao, YT Zhu, and RZ Valiev. Enhanced mechanical properties in ultrafine grained 7075 Al alloy. *Journal of Materials Research*, 20(2):288–291, 2005.

[31] Manish Chauhan, Indranil Roy, and Farghalli A Mohamed. High-strain-rate superplasticity in bulk cryomilled ultra-fine-grained 5083 Al. *Metallurgical and Materials Transactions A*, 37:2715–2725, 2006.

[32] M Murayama, Zenji Horita, and K Hono. Microstructure of two-phase Al–1.7 at% Cu alloy deformed by equal-channel angular pressing. *Acta Materialia*, 49 (1):21–29, 2001.

[33] Hans J Roven, Manping Liu, and Jens C Werenskiold. Dynamic precipitation during severe plastic deformation of an Al–Mg–Si aluminium alloy. *Materials Science and Engineering: A*, 483:54–58, 2008.

[34] Bogusława Adamczyk-Cieślak, Jarosław Mizera, and Krzysztof Jan Kurzydłowski. Microstructures in the 6060 aluminium alloy after various severe plastic deformation treatments. *Materials Characterization*, 62(3):327–332, 2011.

[35] Gloria Graf, Petra Spoerk-Erdely, Peter Staron, Andreas Stark, Francisca Mendez Martin, Helmut Clemens, and Thomas Klein. Quench rate sensitivity of age-hardenable Al-Zn-Mg-Cu alloys with respect to the Zn/Mg ratio: An in situ SAXS and HEXRD study. *Acta Materialia*, 227:117727, 2022.

[36] Zhaorui Zhang, Yue Li, Hongxiang Li, Di Zhang, and Jishan Zhang. Effect of high Cu concentration on the mechanical property and precipitation behavior of Al–Mg–Zn-(Cu) crossover alloys. *Journal of Materials Research and Technology*, 20:4585–4596, 2022.

[37] Sergiy V Divinski, Gerrit Reglitz, Harald Rösner, Yuri Estrin, and Gerhard Wilde. Ultra-fast diffusion channels in pure Ni severely deformed by equal-channel angular pressing. *Acta Materialia*, 59(5):1974–1985, 2011.

[38] Paul A Rometsch, Yong Zhang, and Steven Knight. Heat treatment of 7xxx series aluminium alloys—Some recent developments. *Transactions of Nonferrous Metals Society of China*, 24(7):2003–2017, 2014.

[39] John A Thornton. The microstructure of sputter-deposited coatings. *Journal of Vacuum Science & Technology A: Vacuum, Surfaces, and Films*, 4(6):3059–3065, 1986.

[40] R Van Gastel, E Somfai, SB Van Albada, W Van Saarloos, and JWM Frenken. Nothing moves a surface: Vacancy mediated surface diffusion. *Physical Review Letters*, 86(8):1562, 2001.

[41] Diego Santa Rosa Coradini, Matheus Araujo Tunes, Patrick Willenshofer, Cameron Quick, Thomas Kremmer, Stefan Luidold, Peter J Uggowitzer, and Stefan Pogatscher. Unravelling Nanometallurgy with in Situ Electron-Microscopy: A Case Study with Cu Nanowires. Available at: https://dx.doi.org/10.2139/ssrn.4313569, 2022.

[42] Benjamin Milkereit, Olaf Kessler, and Christoph Schick. Recording of continuous cooling precipitation diagrams of aluminium alloys. *Thermochimica Acta*, 492(1-2):73–78, 2009.

[43] Benjamin Milkereit, Olaf Kessler, and Christoph Schick. Precipitation and dissolution kinetics in metallic alloys with focus on aluminium alloys by calorimetry in a wide scanning rate range. *Fast Scanning Calorimetry*, pages 723–773, 2016.

[44] Benjamin Milkereit, Lydia Burgschat, Richard H Kemsies, Armin Springer, Christoph Schick, and Olaf Kessler. In situ differential scanning calorimetry analysis of dissolution and precipitation kinetics in Mg–Y–RE alloy WE43. *Journal of Magnesium and Alloys*, 7(1):1–14, 2019.

[45] Sebastian Samberger, Lukas Stemper, Florian Schmid, and Stefan Pogatscher. Effect of Heating/Cooling-rates on the aging behaviour of Al alloys. In *Proceedings of EMC*, page 1, 2023.

[46] Phillip Dumitraschkewitz, Matheus A Tunes, Cameron R Quick, Diego Santa Rosa Coradini, Thomas M Kremmer, Parthiban Ramasamy, Peter J Uggowitzer, and Stefan Pogatscher. MEMS-Based in situ electron-microscopy

investigation of rapid solidification and heat treatment on eutectic Al-Cu. *Acta Materialia*, 239:118225, 2022.

[47] Josh Kacher, Ting Zhu, Olivier Pierron, and Douglas E Spearot. Integrating in situ TEM experiments and atomistic simulations for defect mechanics. *Current Opinion in Solid State and Materials Science*, 23(3):117–128, 2019.

[48] T Frolov, M Asta, and Y Mishin. Phase transformations at interfaces: observations from atomistic modeling. *Current Opinion in Solid State and Materials Science*, 20(5):308–315, 2016.

[49] Yang Hu and Timothy J Rupert. Atomistic modeling of interfacial segregation and structural transitions in ternary alloys. *Journal of Materials Science*, 54 (5):3975–3993, 2019.

[50] Carl V Thompson. Grain growth in thin films. *Annual Review of Materials Science*, 20(1):245–268, 1990.

# Chapter 7

# Summary and Outlook

The research presented in this work contributes significantly to the understanding and advancement of 5xx/7xxx Al crossover alloys, focusing on their fundamental behaviour. These novel alloys demonstrate enhanced performance for high-demanding applications, which are critical for various industrial sectors, including automotive, aerospace and space applications. One of the key outcomes of this study is the identification of the optimal alloy composition, which balances strength, ductility, and irradiation resistance.

The first publication presented in chapter 4 revolved the successful manufacturing process of an ultrafine-grained Al crossover alloy. The study demonstrated that High-Pressure Torsion can achieve a significant reduction in grain size. Although previous irradiation experiments showed the formation and accumulation of radiation-induced point defects in the matrix, these effects were entirely suppressed in the ultrafine-grained alloy, even at very high dose levels. This is linked to the vast amount of grain boundaries in the ultrafine-grained alloy, which can act as sinks for radiation-induced defects, where they can annihilate. As a result, the survivability of the hardening phase during irradiation was extended from 1 dpa to 24 dpa. This improvement was attributed to the addition of alloying elements that dissolved into the T-phase, enhancing its chemical complexity and stability under irradiation.

From a materials science perspective, the reduction in grain size also influences the precipitation behaviour of the alloy significantly. This is further explored in chapter 5, where both the coarse-grained and ultrafine-grained alloy are examined using differential scanning calorimetry to observe the precipitation behaviour as a function of grain size. In both alloys, the primary hardening phase was identified as the T-phase; however, the ultrafine-grained alloy exhibited accelerated precipitation kinetics. This can be attributed to the higher density of grain boundaries in the ultrafine-grained alloy, which provide rapid diffusion pathways. As a result, the ultrafine-grained alloy achieves quasi-equilibrium conditions much faster than the coarse-grained alloy. Moreover, the thermal stability of the ultrafine-grained crossover alloy was monitored during *in situ* Transmission Electron Microscopy investigations. It was discovered that the T-phase has a strong ability to pin the grain boundaries under thermal exposure, inhibiting recrystallisation processes up to temperatures exceeding 300 °C.

Finally, the publication in chapter 6 offers insights into various experimental techniques for microstructural characterisation. The ultrafine-grained crossover alloy was annealed under different conditions (*ex situ* and *in situ*) and subsequently compared using Transmission Electron Microscopy. It was observed that precipitation behavior is influenced not only by grain size but also by the experimental method. While precipitation kinetics in bulk materials are primarily governed by volume diffusion of solutes, annealing of thin films can benefit from surface diffusion mechanisms, further enhancing precipitation kinetics. However, it was also found that annealing thin films in *in situ* experiments differs from *ex situ* setups, despite both techniques theoretically promoting precipitation via surface diffusion. In *in situ* experiments, which are conducted in low vacuum, solutes with high vapor pressures (such as Mg and Zn) can easily evaporate in the Transmission Electron Microscopy chamber, rendering them unavailable for precipitation. As a result, the advantages of surface diffusion mechanisms are minimal. In contrast, during *ex situ* thin film annealing, Mg may form a stable oxide layer, which enables surface diffusion and thus accelerates precipitation kinetics.

In conclusion, a stable and irradiation-resistant crossover alloy was manufactured, by designing a material with a high amount of grain boundaries, hardened and stabilised by a chemically complex T-phase. The precipitation behaviour was studied as a function of grain size and experimental techniques, which offers valuable insights for future research. This alloy system demonstrates significant potential for next-generation space materials.

# Chapter 8

# Appendix

The following appendix provides supplemental information and additional resources to support the main content of this document. It includes detailed data and reference materials that offer deeper insights into the subjects covered. The appendix is organized to facilitate easy access to specific sections, ensuring that readers can quickly find the information they need. Table 8.1 lists the amount of artificial intelligence to support the writing of this thesis.

Table 8.1: List of artificial intelligence used in this thesis.

| Objective | Part of AI (in %) | Tool / Version | Remark | Reference to prompting |
|---|---|---|---|---|
| Improvement of linguistic readability | 20 | Chat GPT v4.0 | n/a | oc.unileoben.ac.at/index.php /s/4wqfAs07HAplL3e |

## 8.1 Additional research

In addition to the investigations detailed in the main part of this thesis, we have also conducted extensive research on the corrosion behavior of the crossover alloys. This research was carried out concurrently with the primary studies, focusing on understanding the long-term durability and environmental resistance of the material under various conditions.

At present, the data and findings from the corrosion studies have not been included in this thesis as they are still under analysis and preparation for publication. However, these results are expected to be finalized and made available shortly after the completion of this thesis. Once published, the data will be accessible online for reference. The next section shows the figures which will be presented in the published version of the publication.

### 8.1.1 Figures of the corrosion-related studies

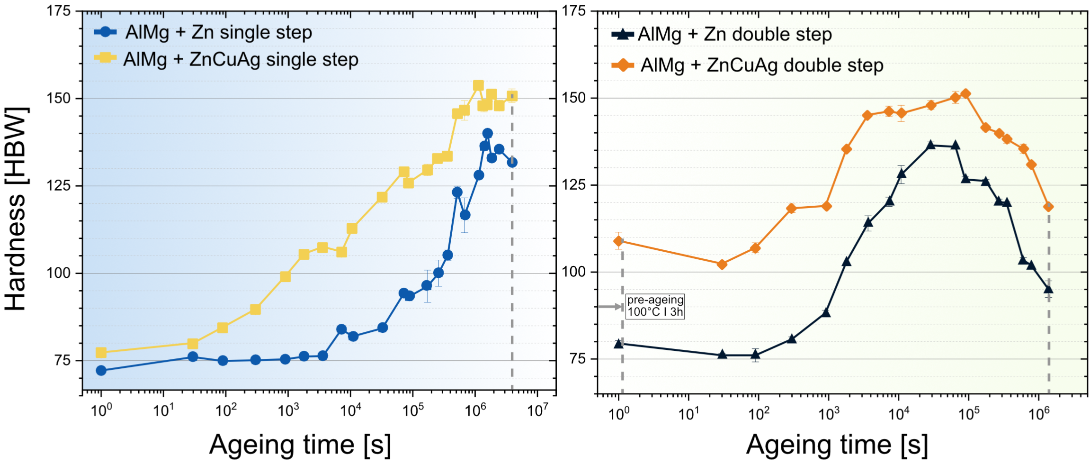

Figure 8.1: Evolution of hardness vs. time. Left: single-step ageing at 125°C for 45 days. Right: double-step ageing with pre-ageing at 100°C/3h + 175°C for 16 days. Note that the time scale is plotted logarithmic.

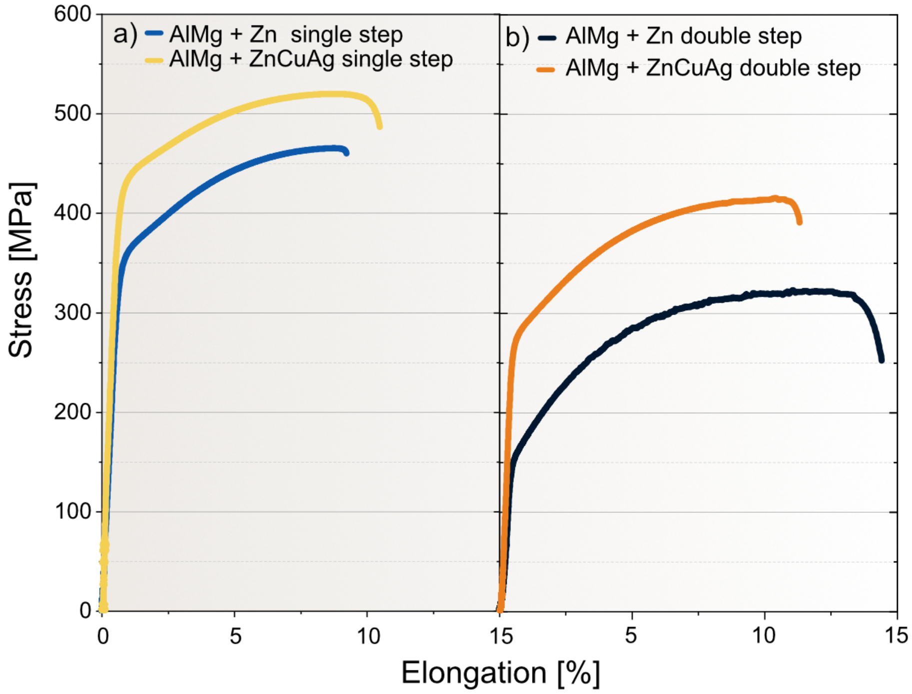

Figure 8.2: Tensile tests of a) single-step ageing at 125°C for 45 days and b) double-step ageing with pre-ageing at 100°C/3h + 175°C for 16 days.

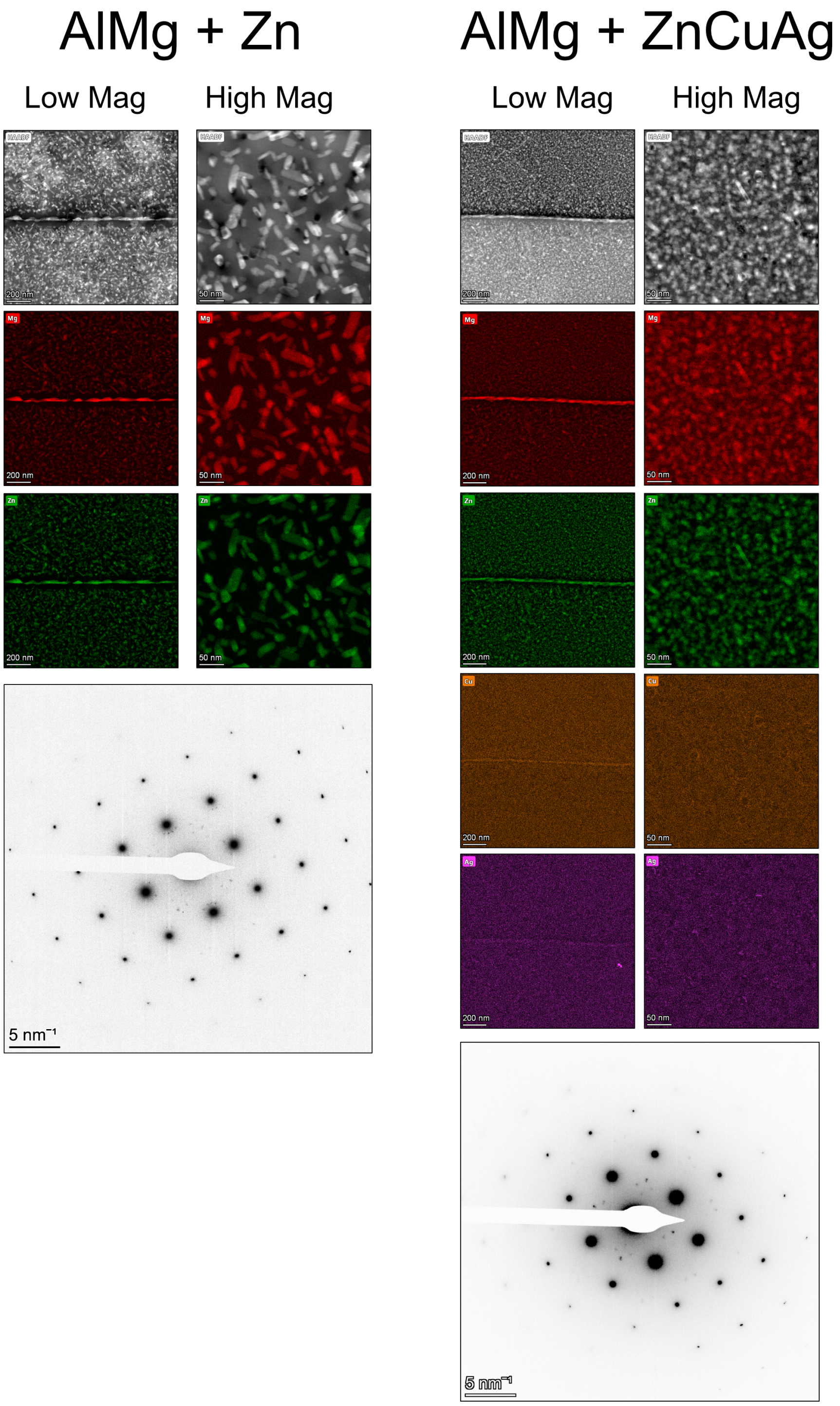

Figure 8.3: STEM-HAADF images of (a) AlMg+Zn and (b) AlMg+ZnCuAg alloys in single-step ageing condition after 45 days at 125°C. Low magnification images were taken at the grain boundaries, while high magnification images are shown within the matrix.

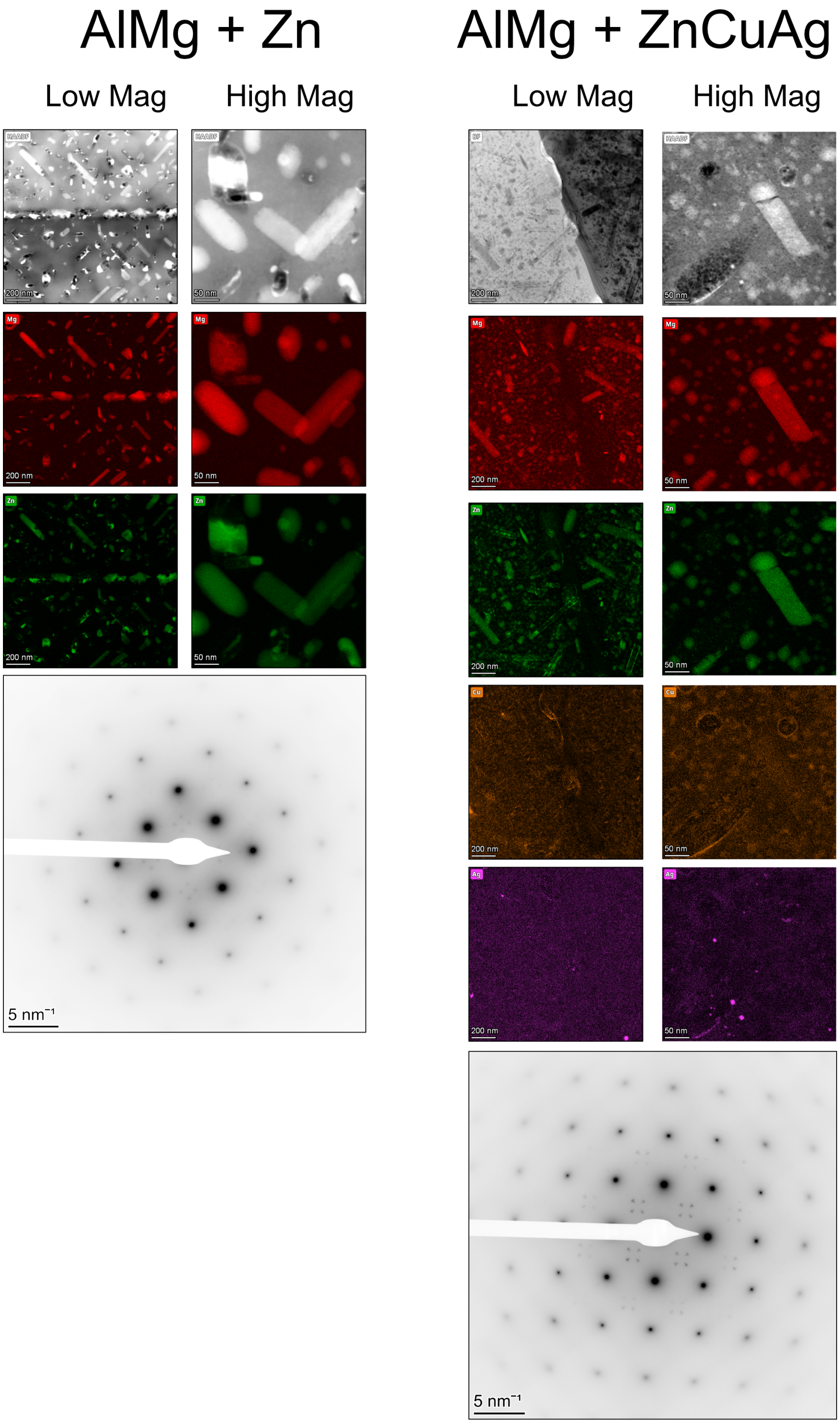

Figure 8.4: STEM-HAADF images of (a) AlMg+Zn and (b) AlMg+ZnCuAg alloys in double-step ageing condition after pre-ageing (100°C/3h) and 16 days at 175°C. Low magnification images were taken at the grain boundaries, while high magnification images are shown within the matrix.

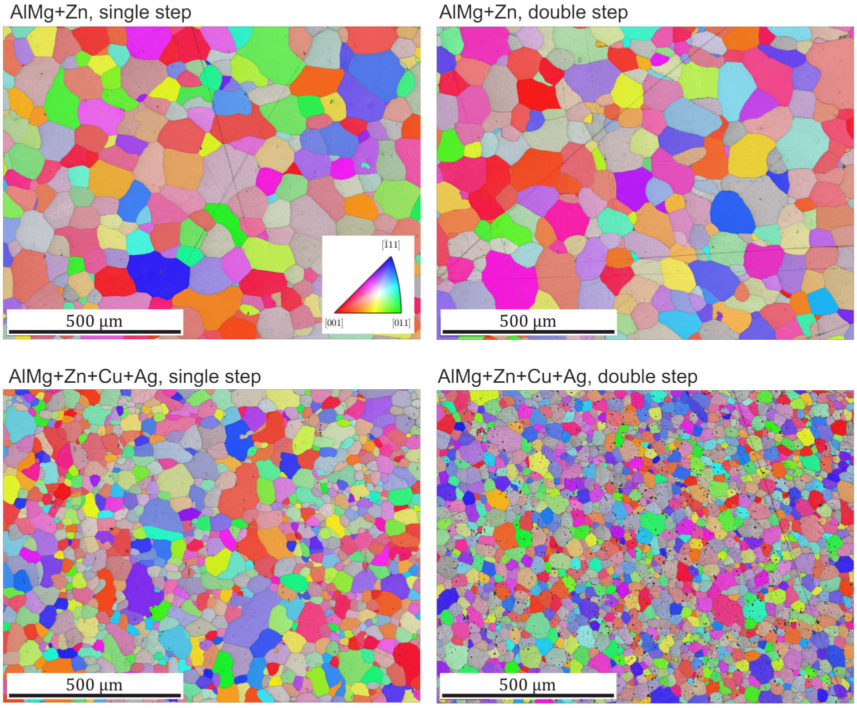

Figure 8.5: Inverse pole figure maps of the tested sample surfaces. The color code corresponds to the orientation triangle

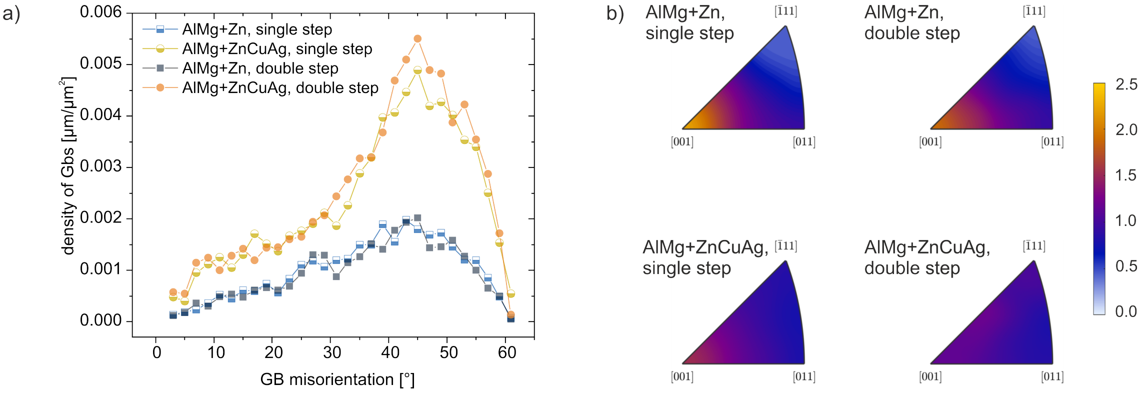

Figure 8.6: a) Comparison of the densities of grain boundaries over the grain boundary misorientation angle and b) texture visualized as orientation distribution function in an orientation triangle in sample normal direction

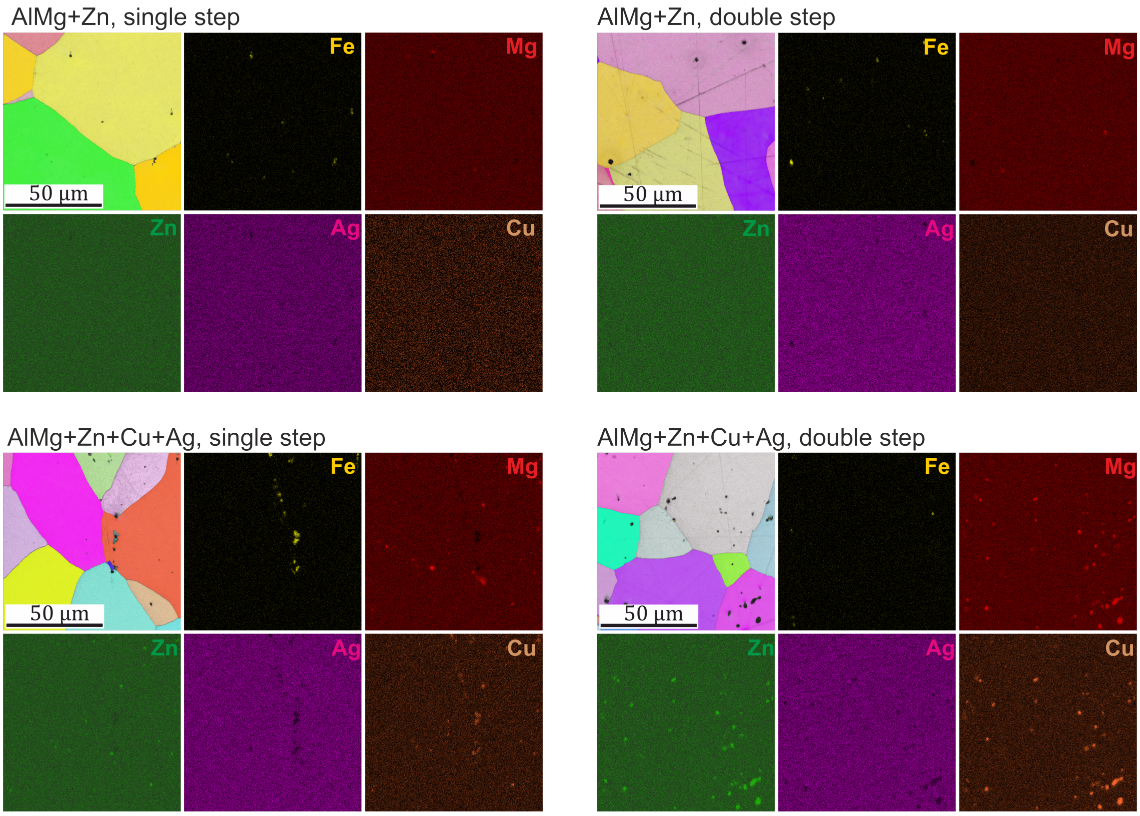

Figure 8.7: EBSD/EDS scans in higher resolution, showing the microstructure via inverse pole figure coloring and the band contrast in gray scale, compared to EDS maps of the main alloying elements.

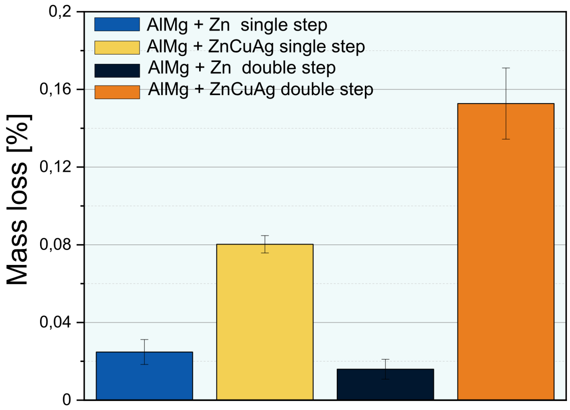

Figure 8.8: Results of mass loss test of the AlMg+Zn(CuAg) crossover alloy in single step (125°C for 45 days) and double step (100°C/3h + 175 °C for 16 days) condition.

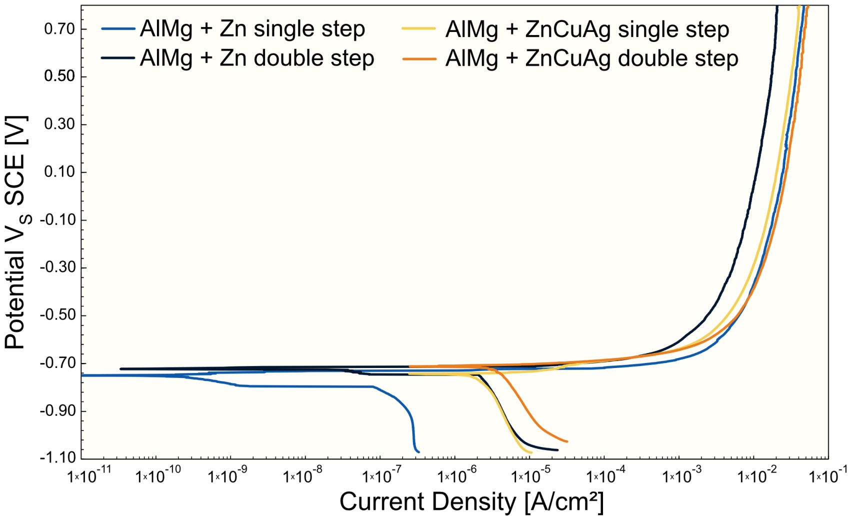

Figure 8.9: Results of the potentiodynamic polarization tests in 0.5 wt.-% NaCl solution. Single step heat treatment was carried out at 125 °C for 45 days and double step heat treatment at 100 °C/3h + 175 °C for 16 days.

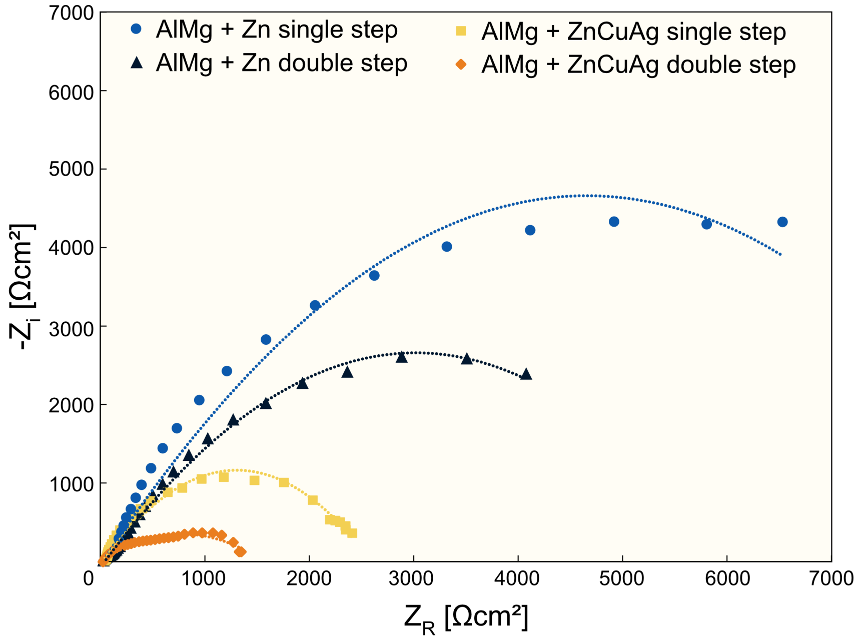

Figure 8.10: Results of the electrochemical impedance spectroscopy tests performed in 0.5% NaCl solution, representation with Nyquist plot, dots represent experimental data, lines the results of the fitting. Single step heat treatment was carried out at 125 °C for 45 days and double step heat treatment at 100 °C/3h + 175 °C for 16 days.

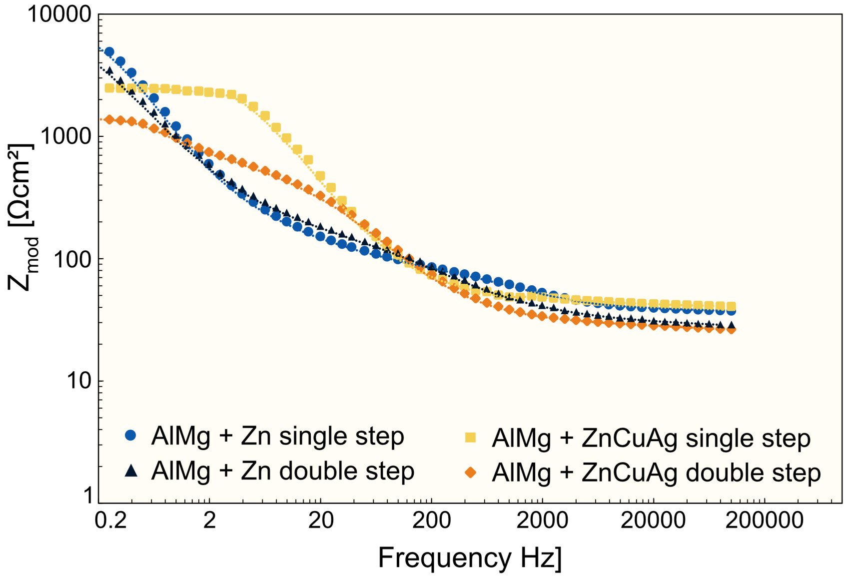

Figure 8.11: Results of the electrochemical impedance spectroscopy tests performed in 0.5% NaCl solution, representation with Bode plot, dots represent experimental data, lines the results of the fitting. Single step heat treatment was carried out at 125 °C for 45 days and double step heat treatment at 100 °C/3h + 175 °C for 16 days.

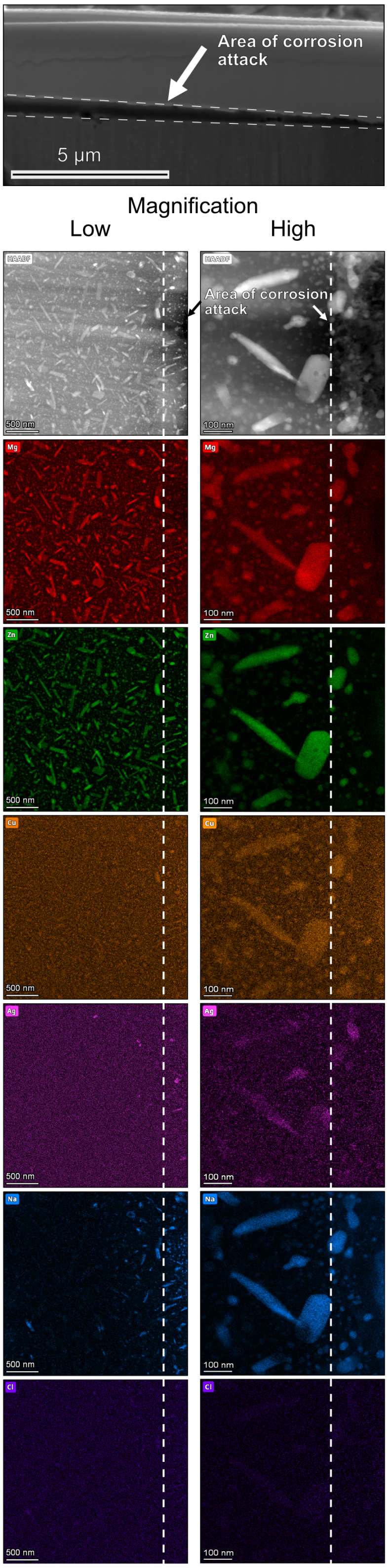

Figure 8.12: Post characterisation of the AlMg+ZnCuAg alloy with double step heat treatment (100 °C/3h + 175 °C for 16 days). A TEM lamellae was lifted out from the area of corrosion attack. The top image shows an overview SEM image, while the bottom depicts STEM-HAADF and elemental mappings. Left: low magnification images and right: high magnification images.